Evaluation of permeation of active pharmaceutical ingredients through outer biological barriers for topical application

Dissertation

zur

Erlangung des Doktorgrades (Dr. rer. nat.)

der

Mathematisch-Naturwissenschaftlichen Fakultät

der

Rheinischen Friedrich-Wilhelms-Universität Bonn

vorgelegt von

Sebastian Kalju Kappes

aus

Groß-Umstadt

Bonn 2023

Angefertigt mit Genehmigung der Mathematisch-Naturwissenschaftlichen Fakultät
der Rheinischen Friedrich-Wilhelms-Universität Bonn

Gutachter/Betreuer: Prof. Dr. Alf Lamprecht
Gutachter: Prof. Dr. Yann Pellequer

Tag der Promotion: 12.01.2024
Erscheinungsjahr: 2024

Table of Contents

List of Abbreviations

µCT	X-ray microtomography
API	Active pharmaceutical ingredient
BAT	Brown adipose tissue
BFZ	Bifonazole
BHS	Bovine hoof sheets
BP4202	BIO-PSA™ 7-4202
cAMP	Cyclic adenosine monophosphate
CC	Cocoyl Caprylocaprate
CIDEA	Cell death-inducing DFFA-like effector A
CLB	Clenbuterol
CRE	Canesten® Extra Creme
DIO2	Type II iodothyronine deiodinase
DLS	Dynamic light scattering particle size analysis
DMF	Dimethyl formamide
DMI	Dimethyl isosorbide
DMSO	Dimethyl sulfoxide
DSC	Dynamic scanning calorimetry
DT2054	DuroTAK® 2054
DT2510	DuroTAK® 2510
EtOH	Ethanol
EU	European Union
FDC	Franz Diffusion Cell
FF	Formoterol fumarate dihydrate
FIB	Focused ion beam
H&E	Hematoxylin & eosin
HEC	Hydroxyethyl cellulose
HPC-H	Hydroxypropyl cellulose H
HPC-SL	Hydroxypropyl cellulose SL
HPLC	High performance liquid chromatography
HPRT	Hypoxanthine-guanine-phosphoribosyltransferase
IPM	Isopropyl myristate

LABA	Long-acting beta agonist
LAC	Lacquer
LogP	Octanol-water partition coefficient
MCT812	Miglyol® 812
MeOH	Methanol
MIR	Mirabegron
MW	Molecular weight
MXP	Parteck® MXP
NMP	N-Methyl-2-pyrrolidone
NP-40	Nonidet® P 40 substitute
P407	Poloxamer 407
PAT	Patch
PC	Propylene carbonate
PEG	Polyethylene glycol
PG	Propylene glycol
PGC1α	Peroxisome proliferator-activated receptor gamma coactivator 1-alpha
Ph. Eur.	European Pharmacopoeia
PLM	Polarized light microscopy
PPARy	Peroxisome proliferator activated receptor gamma
PSA	Pressure-sensitive adhesive
qPCR	Real-time polymerase chain reaction
REM	Raster electron microscopy
RLPO	Eudragit® RL PO
RPL13A	Ribosomal Protein L13a
SABA	Short-acting beta agonist
SAL	Canesten® Extra Salbe
SAL w/o	Canesten® Extra Salbe without urea
SC	Stratum corneum
SD	Standard deviation
SDS	Sodium dodecyl sulfate
SDS-PAGE	Sodium dodecyl sulfate polyacrylamide gel electrophoresis
SEM	Scanning electron microscopy

SOL	Solution
SS	Salbutamol hemisulfate
TC	Transcutol®
TEA	Triethylamine
THF	Tetrahydrofuran
TNFα	Tumor necrosis factor alpha
UCP1	Uncoupling-Protein-1
WAT	White adipose tissue
WATi	Inguinal white adipose tissue
WT	Wild type
XRD	X-ray diffraction
β2ADR	β2-adrenoreceptor
β3ADR	β3-adrenoreceptor
βADR	β-adrenoreceptor

List of Figures

List of Tables

1 Abstract

The pharmaceutical therapy of diseases and health conditions is mostly connected to a systemic application of drug substances, most commonly in the form of solid dosage forms for oral application in order to reach their designated target tissue. However, the relative ease of solid dosage form development, manufacturing, and the high patient compliance come at the cost of non-intended exposure of the body's tissues to active pharmaceutical ingredient (API). This may result in adverse effects and reduce therapeutic success.

An alternative to the application of systemically effective drug delivery systems is the use of topical dosage forms, whose advantage is the exposure to drug right at the target tissue or in the nearest vicinity to it. Thus, adverse effects can be reduced, and highly effective drug concentrations still be achieved.

This work focuses on dosage forms that are designed for delivery of APIs over a barrier to treat the barrier itself and even more so the adjacent tissue beneath, specifically by application on the skin and the nail plate.

First, the delivery of actives to the subcutaneous white adipose tissue, to remodel it for a potential use in metabolic disorders, is addressed. For this, feasibility studies for the topical application of the browning agents mirabegron, clenbuterol, salbutamol hemisulfate, and formoterol fumarate dihydrate are described with a focus on permeation through human skin *in-vitro*. The substances are proposed to induce a change of phenotype from white adipocytes, which store energy in the form of triglycerides, towards a beige form of adipocyte that expresses proteins of brown adipocytes. This would thereby increase energy expenditure of the treated tissues by enabling combustion of the stored fat in non-shivering thermogenesis. For all these compounds first formulations were found that allowed significant delivery through 400 µm thick human skin. Further experiments on mice *in-vivo* and full thickness abdominal human skin with adhering adipose tissue *ex-vivo* confirmed the delivery observed *in-vitro* and the proposed effect of the substances by results on gene and protein level, as well as histologically. The presented therapeutic approach could thus be a highly valuable approach to treat metabolic diseases, such as diabetes mellitus and obesity.

Secondly, improvement of existing Franz Diffusion Cell setups for delivery to the nail is explored. While permeation study design is rather sophisticated for skin as the barrier in question, ungual permeation has been poorly studied, despite the need for highly effective

medicines for diseases related to this skin appendage, such as fungal infection. Therefore, the nail has continued to be a formidable barrier up to this day and predictive test systems are needed. The work herein presents an improvement to an *in-vitro* permeation model using membranes of bovine hoof as human nail surrogates to study ungual permeation. For this, membranes of 100 µm and 400 µm thickness, as well as 400 µm membranes infected with *Trichophyton rubrum*, the most prominent cause of onychomycosis, were compared in terms of their respective applicability for ungual permeation assessment from dosage forms with an immediate or prolonged release profile of the commercially used antifungal model drug bifonazole. It was discovered that prolonged release dosage forms could be compared in the 100 µm setup with sufficient resolution to save time. In contrast, differences between dosage forms with immediate release characteristics and contained permeation enhancer were more pronounced using a more physiological thickness of 400 µm. Moreover, infection of membranes still enabled assessment of the effect of vastly different formulation composition on flux, and in addition allowed testing of membrane ablation as a desired side effect of treatment.

2 Theoretical Background

2.1 Topical Application of Medicines

Although oral administration of solid dosage forms such as tablets is the most common route of drug delivery, administration of an active pharmaceutical ingredient (API) on and through the outer barriers of the body has unique advantages [1].

Upon application of a medicine onto an outer barrier of the body, the dosage form of an API may be designed to deliver the API for two different purposes. Either topical administration is desired, in which a direct or local effect on the barrier or adjacent tissues is to be achieved, or systemic action is pursued, i.e., an effect on the entire body by absorption of API into and subsequent distribution through the vascular system. The latter, in the case of application to the skin, is commonly called transdermal administration and is also referred to as such in this thesis, while the local therapeutic approach is referred to as topical or dermal.

Topical therapy is advantageous in case of diseases or conditions that directly originate in or concern the barrier tissues, on which the medicine is applied on, or tissues in the immediate vicinity.

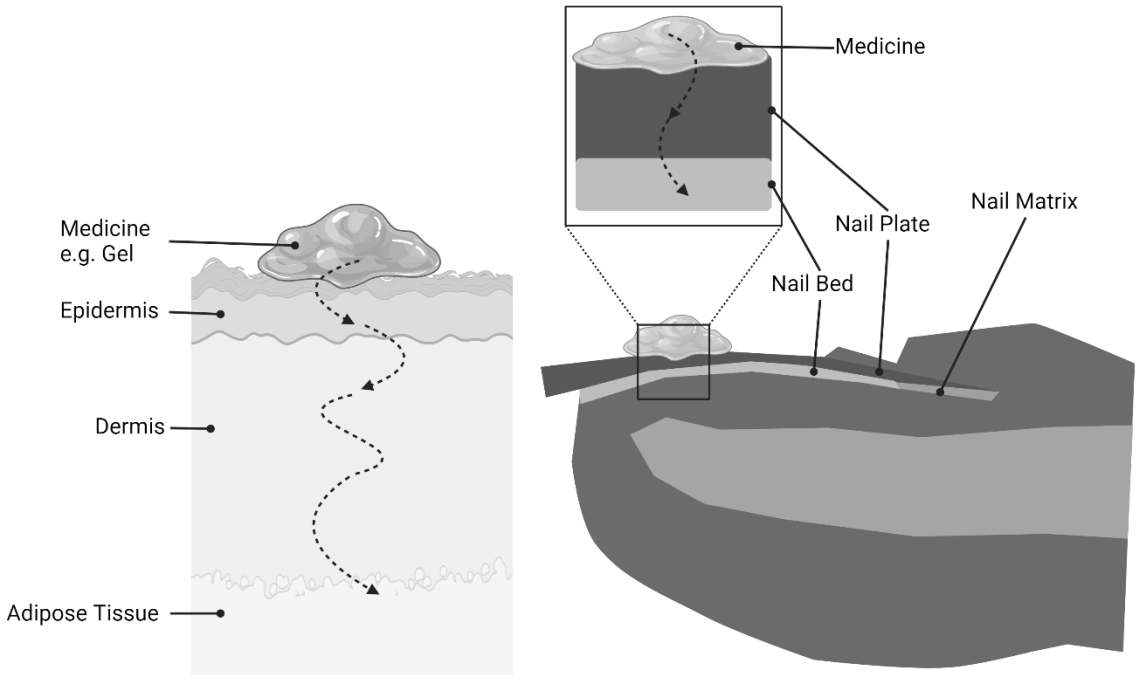

Figure 1: Schematic representation of topical medicine administration onto skin (left) and nail (right). The active pharmaceutical ingredient (API) is liberated from its formulation and penetrates into the external barriers i.e. the epidermis or the nail plate allowing for treatment of these structures. To treat the adjacent tissues, the API must permeate through these barriers in effective quantities. Created with Biorender.com

This advantage lies in the achievement of highly effective doses of API at the target site, without prior uptake into the vascular system, while diminishing side effects on further tissues that would only be exposed to API by unwanted distribution.

The barriers studied in this thesis include the skin and the nail plate, where the upper layers of skin can be characterized as a more lipophilic and the nail as a rather hydrophilic membrane, which will be discussed in more detail in the following chapters. In both cases an API must permeate through the barriers to treat the tissue directly beneath i.e., the subcutaneous adipose tissue or the nail bed (Fig. 1). For this purpose, suitable formulations, and test systems to assess these must be developed.

2.2 Skin – Structure and Function

The skin is the largest organ of the human body [2]. As a barrier it protects against physical, chemical, and biological hazards from the outside, such as microorganisms, heat, UV-irradiation, or xenobiotics, and prevents loss of water from the inside [3]. Furthermore, it enables the sensation of heat or cold, as well as touch and pain to register and prevent damage to the body. To fulfill this task, the skin has developed a multilayered structure, each with unique makeup and function (Fig. 2).

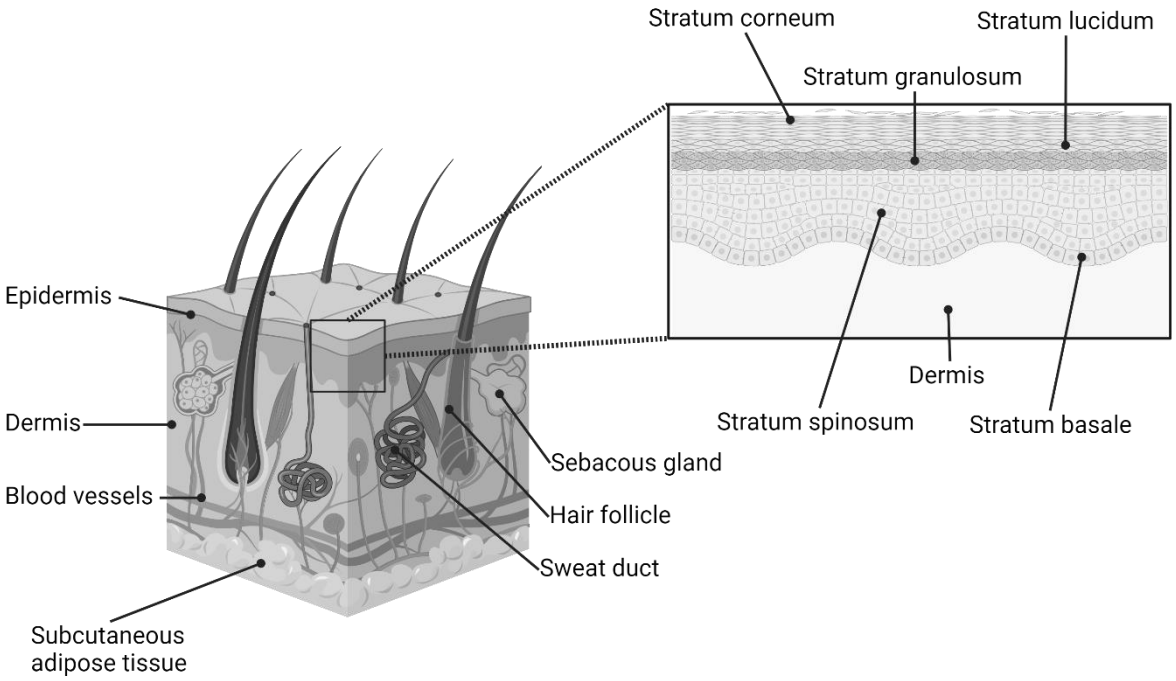

Figure 2: Schematic structure of the human skin with adjacent subcutaneous adipose tissue. Created with BioRender.com.

The epidermis is the outermost skin layer and is itself divided into several strata of keratin containing epithelial cells that grow from the stratum basale over the stratum spinosum, stratum granulosum, and stratum lucidum towards the outermost structure, the stratum corneum (SC). During this journey the cells have died and ejected their nucleus, leaving the keratin filled flattened corneocytes on the skin surface. Combined with the lipophilic intercellular matrix, which is rich in ceramides, cholesterol, and fatty acids that are stacked as bilayers, the resulting structure is referred to one of 'brick and mortar' [4,5].

Below the epidermis, the dermis, which is a layer that is comprised of connective tissue and contains blood vessels and nerves, supplies the epidermis with nutrients. Furthermore, the collagen and elastin inside provide the skin's mechanical strength and elasticity.

The innermost layer is the subcutis, which contains adipose and connective tissue. In addition to energy storage in the adipocytes, this layer helps to insulate the body and protect it against external damage.

2.3 Dermal and transdermal Drug Delivery

Due to its large surface area, the skin has become a viable route of administration for a variety of drugs exploiting a multitude of dosage forms that can target different layers inside the skin for a local therapeutic affect or enable systemic availability.

Formulation approaches for topical drug delivery are manifold and may converge seamlessly into systemic ones. This is due to the interplay of the drug, the barrier and the excipients of the formulation, where careful variation of the excipients of the specific base formulation with respect to the properties of an API may alter the permeability and diffusivity in the barrier, which determines whether a drug reaches its deeper target tissue, is transported to the vasculature, or strands in the upper layers of the skin.

Typical topical dosage forms encompass liquid or semisolid systems, as well as patches. Liquid dosage forms for cutaneous drug delivery are defined in the European Pharmacopoeia (Ph. Eur.) as 'solutions, emulsions, and suspensions with varying viscosity', which also includes more advanced formulation techniques such as nanoparticles, while semi-solid dosage forms include ointments, creams, gels, pastes and poultices that generally are characterized by non-Newtonian flow [6,7]. While no further distinction is made for liquid and semi-solid dosage forms regarding local and systemic exposure, patches are split into two categories, cutaneous and transdermal patches, in which the latter emphasizes the

systemic delivery of an API, whereas the cutaneous patch is to deliver the API locally [8]. Nevertheless, both the cutaneous and the transdermal patch are to supply the API to the tissue over an extended period of time, which further differentiates this dosage form from the liquid and semi-solid forms [8].

Unsurprisingly, not every API can effectively be formulated into one universally applicable vehicle. Instead, an API's unique physicochemical properties, as well as its pharmacological and toxicological potency necessitates adjusting formulations to achieve the desired permeation characteristics.

For example, a rather advanced dosage form, such as a patch in which the drug is typically dissolved in the adhesive, would require both the API and the adhesive polymer to be sufficiently soluble in the same volatile solvents, to enable casting of a blend that results in a homogenous dry product. In the finished product interactions of the drug with the respective adhesive and its solubility therein have to be considered, as they determine the diffusion within and the rate of release of drug from this dosage form [9,10]. As each API has its unique physicochemical and pharmacological properties, development of a certain dosage form might be favorable for one API, but not for another.

Thus, not every API in this work was formulated exclusively in the same dosage form and formulation, but varying forms were investigated when promising formulations were suspected, due to potency and solubility profile.

However, all of these noninvasive delivery approaches have in common that the API is either delivered by passive diffusion through the stratum corneum via an inter- or transcellular pathway, or by uptake through the transappendageal pathways i.e., sweat glands and hair follicles (Fig. 3) [11]. Although the transcellular pathway was shown to be important, especially for hydrophilic compounds, and the transappendageal route was shown to be targetable by utilizing drug nanoparticle suspensions, which due to their size can penetrate into these structures, the intercellular pathway is considered to be the most important route of delivery and can be characterized as lipophilic [12–16]. If API is to be delivered into deeper layers of the skin, to treat non-superficial conditions, it has to further distribute into the viable epidermis below the SC, which itself is a considerable barrier [17]. The barrier properties can be explained by the change in environment from rather lipophilic to hydrophilic, due to the increased water content [18,19]. Thus, the permeation of highly lipophilic compounds was found to be hindered by the viable epidermis [20–22].

Hence, APIs for dermal or transdermal application are generally considered to best display an intermediate octanol-water partition coefficient (LogP) between 1 and 3, a molecular weight below 500 Da, and adequate solubility in water and oil [21,23].

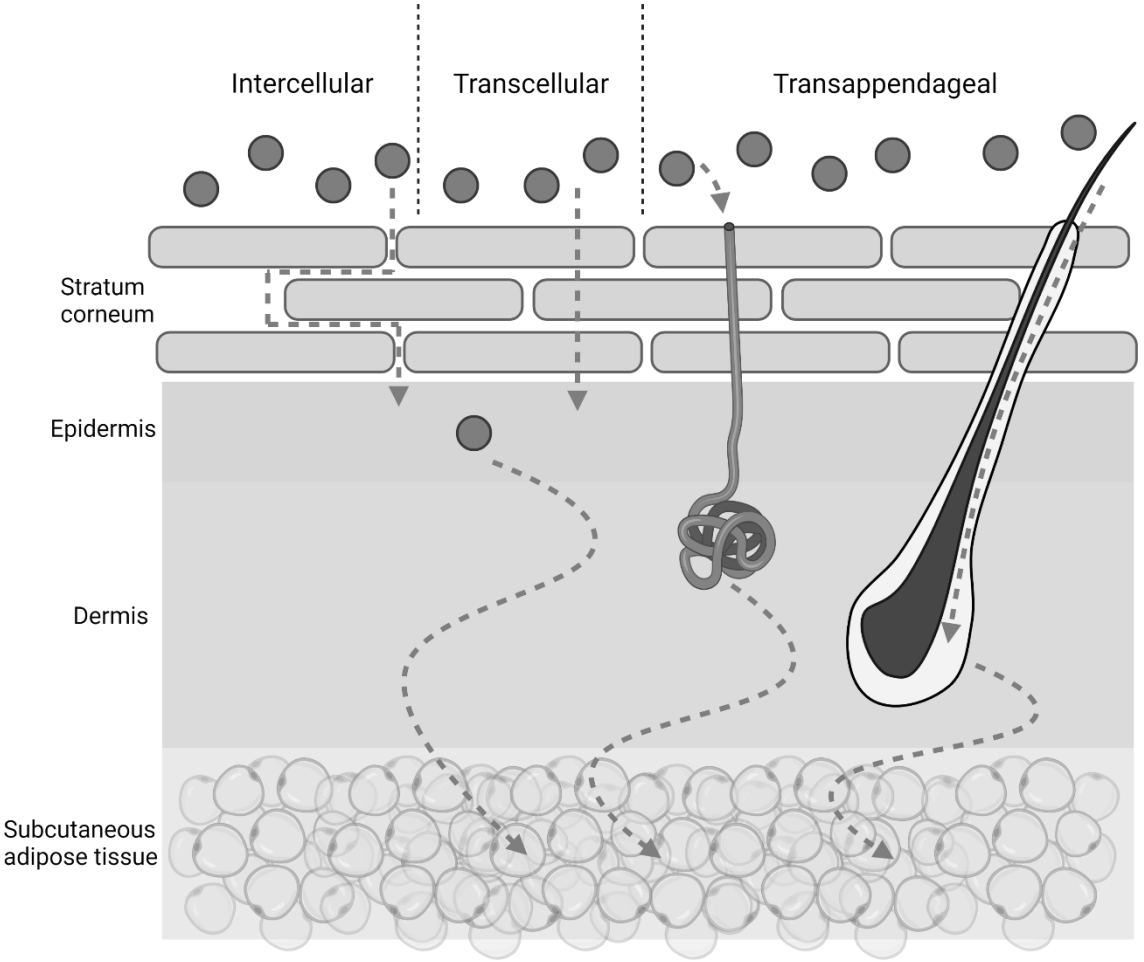

Figure 3: Schematic illustration of (trans-)dermal drug delivery. Pharmaceutical actives (circles) passively cross the stratum corneum via the inter-, transcellular, and transappendageal pathways. Modified from [11]. Created with BioRender.com.

The steady state flux of API that has been released from its formulation follows Fick's first law of diffusion, since the skin can be considered as a membrane. Herein J_{ss} presents the steady state flux that is dependent on the diffusivity D of the drug in the skin, the concentration gradient of drug from its formulation over the skin dC, and the thickness of skin dh (Eq. 1).

$$J_{ss} = -D * \frac{dC}{dh} \qquad \textbf{Eq. 1}$$

From this equation it is apparent that the flux can be enhanced by increasing the concentration of an active in its formulation, as well as by increasing the diffusivity of a drug in the skin, or reduction of the membrane's thickness. As the concentration of a drug is typically limited by its solubility in the applied vehicle, the addition of permeation enhancers like organic solvents that increase the solubility in the vehicle could increase flux. Furthermore, the preparation of drug nanoparticle suspensions was demonstrated to cause an increase in the kinetic solubility, as well as the dissolution velocity of nanoparticles compared to bulk drug due to the large surface area, which was shown to increase penetration of drug into the skin [13,15].

2.4 (Trans-)Dermal Permeation Enhancement

As reduction of the skin's thickness is not suitable for the *in-vivo* application of topical or transdermal formulations, a lot of work has been focused on the increase of diffusivity of drug inside the skin and increasing the APIs' solubility in their respective formulation to increase the available concentration of dissolved drug. The most used technique has become the addition of one or more co-solvents or solutes that act as chemical penetration enhancers to the formulation. These enhancers should be toxicologically harmless and facilitate transport by reversible effects on the skin. For this a multitude of substances from different chemical groups, such as alcohols, glycols, pyrrolidones, sulphoxides, terpenes, surfactants, fatty acids, and esters have been tested for their permeation enhancement potential and their respective modes of action [11]. In the following a selection of penetration enhancers used in this work are described.

From the class of short chain alcohols, ethanol has been used to increase the flux of poorly water soluble compounds such as Estradiol by increasing the solubility, and thus the available active concentration, in the donor formulation [24]. In addition, due to its volatility, evaporation of ethanol may increase the activity of compounds in the formulation as they approach a supersaturated state [25]. Furthermore, ethanol was shown to increase the solubility in the stratum corneum, thus facilitating the partitioning into the skin [26].

Glycols, such as diethylene glycol monoethyl ether (Transcutol®, TC) were shown to be powerful solvents for numerous actives that easily permeated the stratum corneum and thus increased partitioning into this layer, facilitating transport into the viable epidermis for substances that easily partitioned into this structure, while retaining others in the stratum corneum [27].

Dimethyl sulfoxide (DMSO), a polar aprotic solvent which is used as a universal solvent with properties sufficient to solubilize both polar as well as apolar compounds was found to readily permeate the skin [28]. In addition to increasing the solubility for actives in the skin, DMSO was shown to induce stratum corneum disruption by interaction with lipids and further by inducing a change in keratin conformation from α-helical to β-sheet, possibly resulting in a more loosely ordered stratum corneum [29]. However, reports of foul breath and skin irritation after dermal application have limited the broader use of DMSO thus far [11].

2.5 Adipose Tissue and Obesity

Adipose tissue can be divided into two physiological types, namely a white and a brown phenotype. While the white adipose tissue (WAT) is predominantly found around the organs and in the subcutaneous tissue in adults, brown adipose tissue (BAT) is mainly found in the interscapular region of infants and has been found in the cervical, supraclavicular and paravertebral regions in adults [30].

The function of WAT is to protect the organs it surrounds from mechanical shock and provide a solution for energy storage in the form of triglycerides that can be metabolized if need be. In contrast, BAT in a response to cold enables energy consumption by non-shivering thermogenesis, due to the ability to short-circuit the respiratory chain in mitochondria [31]. The difference in function is also manifested in the morphology of the cells. White adipocytes have one large lipid droplet and are generally larger than brown ones whose lipid droplets are numerous and contain a high number of mitochondria [32]. This change of phenotype and function stems from the expression of genes that can be analyzed as browning gene markers to differentiate between both types, because they are exclusively expressed in BAT.

The most important marker gene is Uncoupling-protein-1 (UCP1), which allows the proton gradient formed in the respiratory chain in mitochondria to be relieved without the production of ATP, but instead to be translated into heat [33,34]. Further browning markers which are frequently evaluated are cell death-inducing DFFA-like effector A (CIDEA), which directs the capacity of lipid storage in adipocytes and peroxisome proliferator-activated receptor gamma coactivator 1-alpha (PGC1α), that is a co-activator of the adipogenesis master regulator Peroxisome proliferator activated receptor gamma (PPARy) and induces UCP1 expression and mitochondrial biogenesis [35–38]. Another marker that

was evaluated in this thesis is Type II iodothyronine deiodinase (DIO2) that transforms Thyroxine to Triiodothyronine in brown adipocytes and thus indirectly induces UCP1 expression [39,40].

Despite its physiological function, an excessive energy intake and subsequent strong increase in WAT mass might lead to the pathophysiological state of obesity. Obesity is a known risk factor for a variety of pathological conditions and diseases, especially concerning the cardio-vascular or metabolic system [41]. Nevertheless, every second citizen of the European Union (EU) is overweight and more than 40% of US citizens are considered obese as characterized by a body mass index above 25 and 30, respectively [42,43]. In addition, the proportion of overweight people is steadily increasing, which burdens the health care systems of nations and thus requires pharmacotherapeutic assistance in weight loss [44].

Existing pharmaceutical therapy options include oral administration of anorectics that reduce appetite, e.g. amphetamine analogues and cannabinoid receptor antagonists, or lipase inhibitors that inhibit lipid digestion and thus uptake of fatty acids, as well as injection of glucagon-like peptide 1 agonists to induce a faster feeling of satiety [45]. Albeit some of these were shown to be effective, these treatments either share risks of serious adverse effects, for example of cardiovascular or psychological nature, or are tedious in application, and thus offer only limited patient adherence. Alternative pharmaceutical therapies are therefore urgently needed to support weight loss, while retaining a positive benefit-risk evaluation.

A potential therapeutic approach is the activation of existing BAT and the reprogramming of WAT to burn energy rather than store it, by inducing a brown-like, beige phenotype. The potential benefits on cardiometabolic health of increased amounts of BAT were already demonstrated [46]. Beige adipocytes were shown to exhibit morphological features of both WAT and BAT in form of a large main and further small lipid droplets [47]. Furthermore, it was found that they expressed UCP1 and were capable of thermogenesis [48,49]. This browning of WAT has been observed physiologically as a response to cold [50].

Except from cold, BAT activation and browning of WAT can be induced through small molecules by various pathways that work via the common second messengers cyclic adenosine monophosphate (cAMP) or cyclic guanosine monophosphate [51]. Hence, the activation of the β3-adrenoreceptor (β3ADR) with the agonist mirabegron (MIR) was found to activate BAT and induce browning of WAT in rodents and humans, increasing energy

expenditure and potentially assisting weight loss [52–55]. In doses prescribed as a registered medicine against overactive bladder MIR has been proven to be well tolerated [56]. However, a higher dose that is essential for browning, has limited the oral application of MIR in this case, due to cardiovascular adverse effects [53,55]. Furthermore, recent findings have questioned the role of the β3ADR in the induction of browning, due to its low expression in humans and proposed the highly expressed β1- and β2-adrenoreceptors (β1-/β2ADR) to be more relevant, also arguing that browning by MIR is a result of crosstalk at the other ADRs [57–60].

Since agonists of all βADR subtypes share similar adverse effects, especially of cardiovascular nature, a local delivery of API by the cutaneous route would present a more tolerable and highly promising option in the treatment of metabolic disorders.

2.6 Nail – Structure and Function

The human nail protects the tips of fingers and toes and supports gripping, as well as the manipulation of objects. It is comprised of the nail plate, that is the most visible part, the nail bed, the nail matrix, the enclosing nail folds, and the hyponychium [61].

The plate is grown from cells of the proliferative epithelial tissue of the nail matrix, which is located under the proximal nail fold. The denucleation of these cells results in dense layers of dead and flattened cells that are rich in α-keratin, a protein class that also is the main component of hair and the top layers of skin (Fig. 4) [62,63]. The nail's hardness can be explained by the ratio of 80:20 of hard type to soft type keratin [64,65]. Furthermore, the nail plate can be divided into a dorsal, intermediate, and ventral layer [66]. While the cells and thus the keratin fibers are arranged isotropic in the dorsal and ventral layers, the resistance to longitudinal fracture can be explained by the anisotropic orientation of cells in the intermediate layer, whose keratin fibers run perpendicular to the direction of nail plate growth [67].

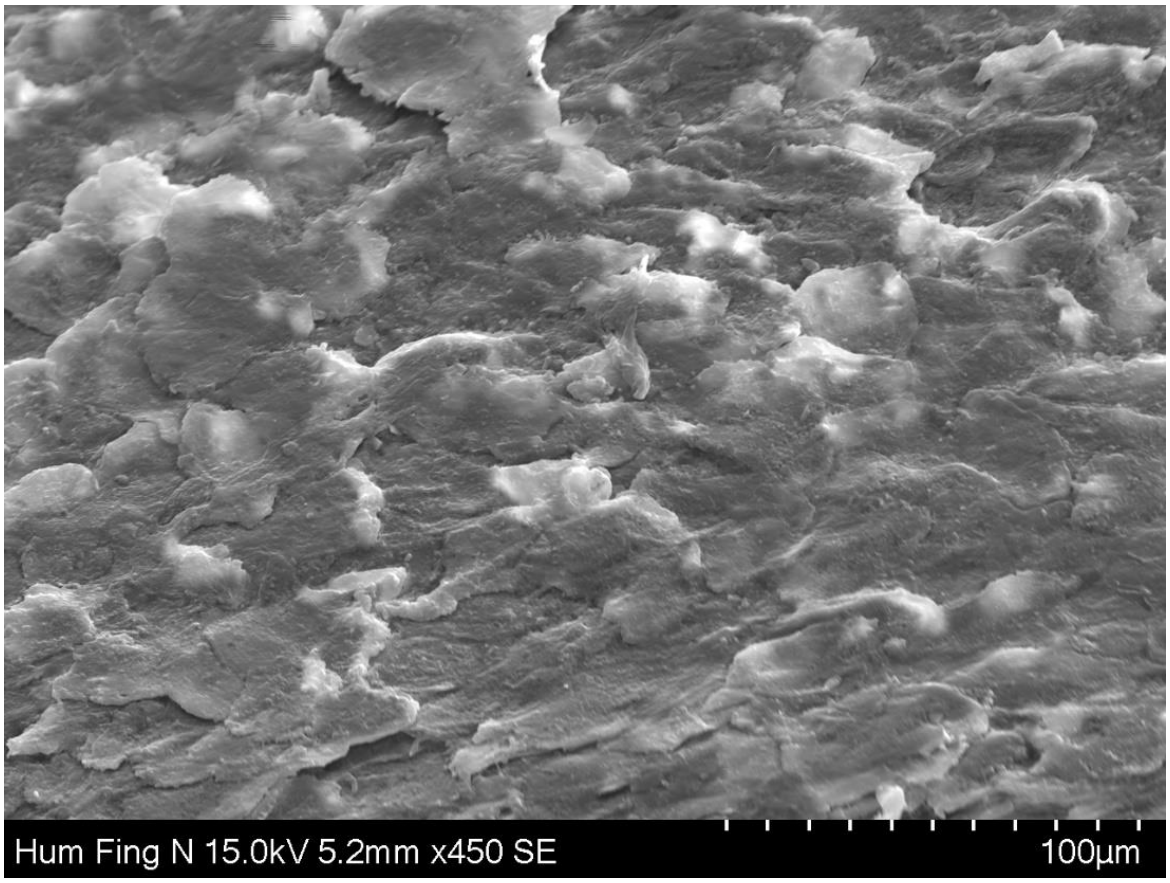

Figure 4: Scanning electron microscopy image of the human nail's dorsal surface. The flattened, dense structure of cells is visible.

When considered as a barrier for drug diffusion the nail plate can be considered as a dense hydrophilic membrane with a lipid content of only 1% and a water content between 14 and 30% depending on the relative humidity of air [66,68,69].

2.7 Ungual and transungual Drug Delivery

Since diseases of the nail might affect each layer of it down to the hyponychium and nail bed, topically applied medicines need to enable penetration of the API into and through the keratin matrix [70].

Although there is no specific monograph for medicines targeting the nail, typical dosage forms are analogous to the cutaneous ones, which were described in chapter 2.3, with a prominent addition in form of lacquer type formulations [71].

Multiple factors influence the permeation of compounds through the nail. It was found that increased molecular weight reduced the permeability of several antimycotic substances in *in-vitro* studies [72].

Furthermore, the permeability of the ionized form of acidic and basic drugs was lower than their uncharged equivalent while maintaining an inversely linear relationship of permeability to molecular weight in both cases [73].

To assess nail permeation complete human nail plates, or clippings thereof can be used in FDC setups with special geometries to account for the nails' curvature. However, complete nail plates are scarcely available, expensive, and clippings are comparably inferior, due to the highly decreased area of diffusion, which, especially in case of poorly permeable drugs, would pose highly demanding requirements to the connected analytics employed [74].

As an alternative membrane animal surrogates e.g. in form of bovine hoof sheets (BHS) have been found to be decently comparable to human nails and several permeation studies have been conducted since [62,72]. Nevertheless, procedures for production of these membranes have only begun to be standardized and variety of acceptor media and membrane thicknesses, often unrepresentative of (patho-)physiological conditions, have been used [75]. Recently even experimental setups utilizing BHS infected with *Trichophyton* species have been tried to mimic pathophysiological conditions and have thereby added to the variability in experimental conditions in nail permeation studies [76].

2.8 Ungual Permeation Enhancement

The chemical permeation enhancers that have been identified differ from those for dermal delivery. For instance, the highly potent dermal permeation enhancer DMSO did not increase permeability of Geraniol over control in the ungual setup [77]. Instead, compounds that break up the dense structure of the nail have shown permeation enhancement potential. The presumed severance of disulfide bonds in the keratin matrix by thiol-group containing substances like N-Acetylcysteine, 2-Mercaptoethanol, and Thioglycolic Acid was found to increase nail plate porosity and therefore to drastically increase permeation [78–80]. In a similar fashion treatment of nail plates with keratinase increased the permeability, further highlighting the importance of keratin disruption [81]. As another popular permeation enhancer, treatment with urea was shown to soften and effectively ablate human nail plate material in patients suffering from onychomycosis, consequently reducing the barrier thickness or even removing it completely [82]. It was further shown to increase delivery of the pharmaceutical actives in several studies [77,83].

2.9 Nail Diseases

The nail is involved in various diseases and disorders. Often the etiology of these conditions might be of autoimmune nature in case of e.g. nail psoriasis, or stem from infection of the nail unit by bacteria or fungi [84]. In each of these cases, topical treatment of the nails presents a favorable way of drug application, as the systemic treatment with considered APIs, such as methotrexate, corticosteroids, or antibacterial and- fungal agents often encompasses serious adverse effects. The most common clinical manifestation of disorders is onychomycosis, the infection of nails by dermatophytes or other fungi [85]. These infections may drastically reduce patients' quality of life, due to associated pain, the unaesthetic appearance, and connected stigma with impact on mental health [86].

3 Aims & Scope

While there are numerous ways for pharmaceutical actives to reach their designated target tissue, those with limited systemic exposure provide the highest safety to patients. This is especially important for APIs with severe adverse effects, narrow therapeutic window, and low tissue specificity.

Fortunately, topical application of formulations on outer barriers of the human body potentially allows for treatment of the barrier itself and the tissue beneath, with limited exposure of the rest of the body. Nevertheless, due to the respective barrier's and API's properties identifying suitable formulations that enable sufficient delivery of API to the desired site of action is challenging.

Both the subcutaneous adipose tissue and the nail bed are tissues, located below excellent barriers in form of the human skin or the nail plate. These barriers efficiently limit the permeation of actives after topical administration and prevent effective treatment, e.g. of obesity in case of adipose tissue or fungal infections of the nail.

Oral treatment of the adipose tissue for the sake of browning, to increase energy expenditure, is problematic, because adrenergic browning agents would need to be applied in high doses and the low organ specificity of these compounds would risk severe adverse effects on the cardiovascular system. Thus, the development of topical formulations that deliver the respective drug to the subcutaneous adipose tissue would potentially enable this novel therapeutic approach for metabolic disorders.

For treatment of onychomycoses, registered antifungal compounds are specific to the metabolism of fungi. However, they often show limited oral bioavailability or risk severe adverse effects on the liver if applied systemically. Delivery by topical application for treatment of the nail plate itself and the underlying nail bed would thus be highly beneficial. To develop effective topical medicines, predictive test systems for permeability assessment are needed. In contrast to skin, where permeation test systems with corresponding guidelines have been developed, standards for ungual permeation experiments have yet to be established, especially when considering the presumably altered barrier properties encountered in diseases of the nail.

Hence, this work focuses on two aspects to advance the development of topical dosage forms, namely identification of suitable formulations as well as the improvement of existing

in-vitro test systems. To this end, the permeation of challenging active ingredients from their respective dosage forms is evaluated either by varying their formulation or by changing the thickness and state of infection of membranes used in Franz Diffusion Cell experiments.

For administration to the skin, topical formulations of the β2ADR agonists formoterol fumarate dihydrate, clenbuterol, salbutamol hemisulfate, and the β3ADR agonist mirabegron should be identified that effectively deliver their API over dermatomized human skin containing both the entire epidermis and parts of the dermis *in-vitro*. Subsequently, initial evidence of efficacy of the identified formulations to brown adipose tissue was to be provided by applying selected formulations on mice *in-vivo*, evaluating expression of browning relevant genes and histologic changes in inguinal WAT.

To improve transungual Franz Diffusion Cell studies, typical topical dosage forms of the antifungal model drug bifonazole were to be produced in addition to an already existing, commercially available, cream and ointment of the same API. To allow picking the optimal membrane for formulation development of different dosage forms and considering an intended use in the treatment of diseased nails, the permeation from these formulations across membranes of bovine hoof as nail plate surrogates should be evaluated in dependence of membrane thickness and an eventual infection by *Trichophyton rubrum*, a common pathogen of onychomycosis.

4 Materials & Methods

For materials and methods used in ungual studies please refer to the corresponding section in ‘Improving Transungual Permeation Study Design by Increased Bovine Hoof Membrane Thickness and Subsequent Infection’ in the appendix.

4.1 Materials

Formoterol fumarate dihydrate (FF), clenbuterol (CLB), salbutamol hemisulfate (SS), and mirabegron (MIR) were of analytical grade or higher and procured from Swapnroop Drugs & Pharmaceuticals (Aurangabad, India). Brij® 98, dimethyl isosorbide (DMI), and triethylamine (99.5%) were products from Acros Organics (Geel, Belgium). Cocoyl caprylocaprate, Poloxamer 407, and Soluplus® were kind gifts from BASF SE (Ludwigshafen, Germany). Hydroxyethyl cellulose 250, isopropyl myristate, Miglyol® 812 (MCT812), polyethylene glycol 300, propylene glycol, and sodium dodecyl sulfate were purchased from Caesar & Loretz GmbH (Hilden, Germany). Sodium fluoride and sodium orthovanadate were bought from Carl Roth (Karlsruhe, Germany). methanol and tetrahydrofuran were purchased from Fisher Scientific (Schwerte, Germany). DowCorning™ BIO-PSA™ 7-4202 was a generous gift from DDP Specialty Electronic Materials (Midland, MI, USA). Transcutol® P was kindly donated by Gattefossé SAS (Saint-Priest Cedex, France). DuroTAK® 387-2054 and DuroTAK® 387-2510 were gifts from Henkel (Düsseldorf-Holthausen, Germany). Pharma grade dimethyl sulfoxide was obtained from ITW Reagents (Monza, Italy). Parteck® MXP was a donation by Merck KGaA (Darmstadt, Germany). Hydroxypropyl Cellulose H and Hydroxypropyl Cellulose SL were kindly donated by Nippon Soda Co., Ltd. (Tokyo, Japan). Dulbecco’s modified eagle medium (DMEM), ethanol abs., ethylene glycol-bis(β-aminoethyl ether)-N,N,N′,N′-tetraacetic acid (EGTA), Nonidet® P 40 substitute (NP-40), and sodium deoxycholate were purchased from Sigma-Aldrich (Taufkirchen, Germany). Orthophosphoric acid 85% was a product of Th. Geyer GmbH & Co. KG (Renningen, Germany). Phosphate buffered saline powder and propan-2-ol were purchased from VWR International GmbH (Darmstadt, Germany). Trizol™ and SYBR™ Green Master Mix were procured from ThermoFisher, Waltham, MA, USA. ProtoScript® II First Strand cDNA Synthesis Kit was purchased from New England Biolabs, MA, USA.

4.2 Tested Active Pharmaceutical Ingredients (APIs)

The APIs in this work were chosen from the classes of β2- and β3ADR agonists (Tab. 1). As such, they share the common backbone of adrenaline derivatives in the form of the phenylethanolamine structure (Fig. 5). Since they are β2ADR selective, FF, CLB, and SS are registered medicines in the EU for treatment of obstructive bronchial diseases. In contrast, MIR is β3ADR selective and registered for use in overactive bladder disease.

Table 1: Tested active pharmaceutical ingredients and their properties. The LogP values were predicted with ChemAxon software and taken from the DrugBank database [87].

	Mirabegron	**Clenbuterol**	**Formoterol Fumarate Dihydrate**	**Salbutamol Hemisulfate**
Molecular Weight [Da]	396.51	277.19	420.46	288.35
Pharmacological Target	β3ADR	β2ADR	β2ADR	β2ADR
LogP (free base form)	2.89	2.33	1.06	0.34
Water Solubility at Room Temperature [µg/mL]	82.0	190.6	568.0	>100,000

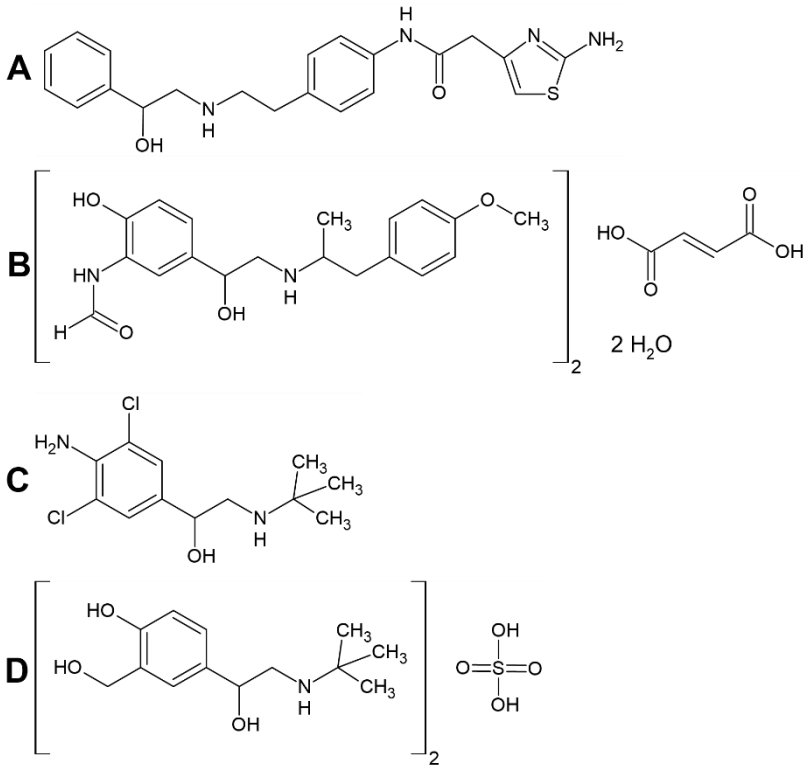

Figure 5: Chemical structures of **A)** mirabegron, **B)** formoterol fumarate dihydrate, **C)** clenbuterol, **D)** salbutamol hemisulfate

4.3 Methods

4.3.1 Solubility Screening of APIs in Excipients and Solvents

For assessment of solubilities of APIs in solvents of various polarities an amount of 100 mg API was added to 4 mL of solvent in a sealable beaker and stirred for 24 h in the dark. The resulting suspensions were centrifuged at 15,000 rpm for 10 min and the supernatant was then filtered over PES or PTFE syringe filters with a 0.22 µm pore diameter. The solutions were analyzed by HPLC-UV and appropriately diluted with 0.1 M HCl or MeOH if needed. Due to the expense of some of the used APIs and the screening character of most solubility assessments the experiments were carried out once or in triplicate. For some solvents, if solubilities were higher than 25 mg/mL, increasing amounts of API were added until no clear solution could be obtained, or 100 mg/mL were reached and the last concentration yielding a clear solution was noted.

4.3.2 Preparation of Gels

Gels were prepared by dissolving the respective API in its solvent mixture and subsequent successive addition of gelling agent under stirring until the agent was completely dissolved.

4.3.3 Preparation of Patches

Patch matrices in the respective producer's solvent composition were mixed with a precisely weighed amount of API under stirring and if necessary, under the addition of a suitable volatile cosolvent to ensure timely and complete dissolution and homogenization of the mixtures. After a clear solution was obtained the mixtures were cast on an occlusive backing liner using a wet film applicator (Multicator 411, Erichsen, Hemer, Germany) at a wet film thickness of 500 µm. Afterwards the patches were allowed to rest for 15 min and subsequently dried in a drying cabinet at 50°C for 30 min. The resulting dry films were covered with a fluoropolymer coated release liner until further use.

4.3.4 Preparation of Nanoparticle Suspensions

Nanoparticle suspensions of mirabegron were prepared by a bottom-up precipitation approach. A volume of 200 µL of a 10% (*w/w*) mirabegron solution in DMSO was added to 10 mL of the respective polymer and tenside solution over 2 min under sonication with an ultrasonic probe at 50% amplitude (Bandelin, Berlin, Germany).

4.3.5 Polarized Light Microscopy (PLM)

A Leica DM 2700M microscope (Leica microsystems, Wetzlar, Germany) equipped with a MicroPublisher 5.0 RTV camera (Teledyne Photometrics, Tucson AZ, USA) was used. Q-Capture Pro 7 software version 7.0.5 was used to take digital images. Solubility studies of CLB in pressure-sensitive adhesive (PSA) matrices were conducted by casting the respective matrix onto microscope slides, with subsequent drying, analogous to preparation of patches.

4.3.6 Scanning Electron Microscopy (SEM)

Micrographs were taken with a Helios G4 CX Dualbeam microscope (Thermo Fisher Scientific, Eindhoven, The Netherlands). Secondary electron images were taken using a 5 kV accelerating voltage at 3 mm working distance with a 'through the lense detector'. Samples were fixed on aluminum stubs using conductive carbon adhesive tape and sputtered with platinum prior to analysis.

4.3.7 Dynamic Light Scattering Particle Size Analysis (DLS)

For DLS measurements nanoparticle suspensions were diluted appropriately with demineralized water and measured at an angle of 173° using an SZ-100 (Horiba, Kyoto, Japan).

4.3.8 High Performance Liquid Chromatography (HPLC)

For every API analysis was conducted on an LC-2040C 3D Plus system with an integrated diode array and a coupled RF-20A fluorescence detector (Shimadzu, Kyoto, Japan), equipped with a C18 reverse phase column (Inertsil ODS-3, 150 mm length, 2.1 mm inner diameter, 3 µm particle size).

For mirabegron and clenbuterol the flow rate was set to 0.3 mL/min and eluent consisted of 25/75 (*%v/v*) methanol (MeOH) and 0.2% (*v/v*) triethylamine (TEA) solution adjusted to pH 3 with orthophosphoric acid. The column temperature was maintained at 40°C and the autosampler temperature was kept at 25°C. The injection volume was 2 µL and the detector was set to 249 nm for mirabegron and 242 nm for clenbuterol, respectively for UV detection. The limit of quantification for both compounds was 100 ng/mL.

For formoterol fumarate dihydrate the flow was set to 0.3 mL/min and a solvent mixture of 35/65 (%*v/v*) MeOH and 0.2% TEA solution adjusted to pH 3 with orthophosphoric acid was used as mobile phase. The column temperature was maintained at 40°C and the autosampler kept at 25°C. The injection volume was 2 µL and the detector was set to 210 nm for UV detection. The limit of quantification was 100 ng/mL.

For salbutamol hemisulfate the flow rate was set to 0.3 mL/min and the eluent consisted of 6/94 (%*v/v*) MeOH and 0.2% (*v/v*) TEA solution adjusted to pH 3 with orthophosphoric acid. The column temperature was maintained at 40°C and the autosampler was kept at 25°C. The injection volume was 2 µL and the fluorometric detection was conducted at an excitation wavelength of 220 nm and an emission wavelength of 310 nm. The limit of quantification was below 100 ng/mL.

4.3.9 Preparation of human Skin Membranes

Human abdominal skin from plastic surgery was obtained from consenting patients and collected immediately after surgery that was performed at Dreifaltigkeits-Krankenhaus, 50389 Wesseling, Germany. Ethical approval was given by the ethics council of the University of Bonn under approval reference 082/20. The subcutaneous adipose tissue was carefully removed with a scalpel and the resulting full thickness skin was frozen at -35°C until use. For permeation experiments skin was thawed at room temperature and subsequently cut to a thickness of 400 µm with a dermatome (Aesculap® Acculan GA643, Tuttlingen, Germany).

4.3.10 Franz Diffusion Cell (FDC) Experiments

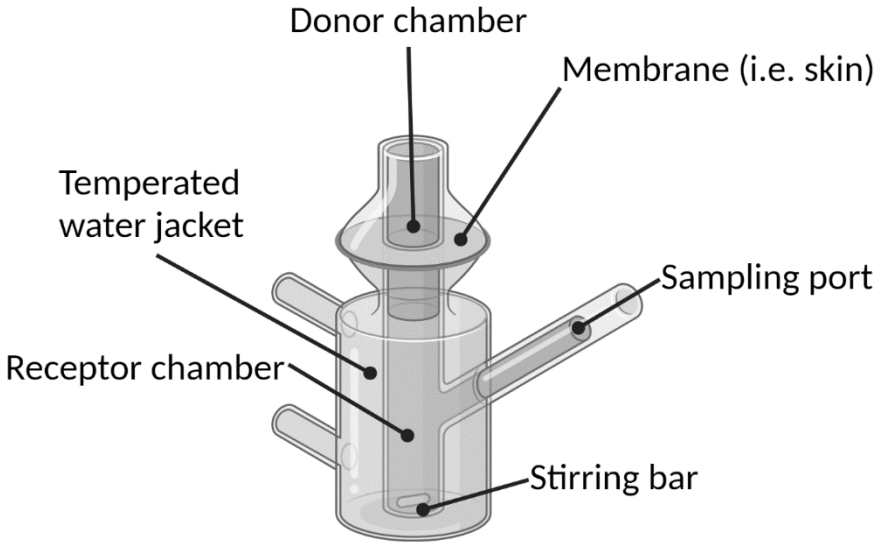

Figure 6: Schematic assembly of a Franz Diffusion Cell. Created with BioRender.com.

Vertical Franz diffusion cells (Fig. 6) with a receptor volume of 8 mL and effective diffusion area of 1 cm² were used for permeation experiments (SES Analysensysteme, Bechenheim, Germany). Human abdominal skin cut to a thickness of 400 µm as in accordance with OECD guideline 408 was placed upon the cells with the stratum corneum facing the air [88]. The skin surface temperature was maintained at 32°C. The receiver consisted of phosphate buffered saline pH 7.4 with 6% (*w/w*) Brij®98, as in accordance with OECD guidelines to ensure sink conditions [89]. A volume of 200 µL of formulation was applied to the skin in the donor compartment and samples of 0.5 mL were taken at defined timepoints and immediately replaced with fresh receptor solution.

4.3.11 Treatment of live human abdominal Tissue *ex-vivo*

Human abdominal skin with underlying subcutaneous fatty tissue was cut into appropriately sized rectangular pieces after surgery without prior freezing and placed into petri dishes that were filled with 20 mL of DMEM containing 10% fetal bovine serum and 1% penicillin/streptomycin. A volume of 0.2 mL formulation was applied to the skin with a syringe and spread across a rectangular area of 6 cm². Dishes were closed and incubated in a drying cabinet for 3 d at 32°C to simulate the outer skin temperature. After incubation, skin was taken from the dishes and fatty tissue directly adjacent to the dermis was sampled for further analysis of gene expression by real-time PCR.

4.3.12 Treatment of Mice with Gels *in-vivo*

The animal studies were performed at the University of Bourgogne Franche-Comté (Besançon, France). All experiments were in compliance with French legislation on animal experimentation within the framework of the Exp An N2 EA4267 2015-2020 project, previously approved by the CEBEA 58 ethics committee. Wild type (WT) C57BL/6 mice were split into groups of eight and treated with verum and a placebo, respectively. Mice were carefully shaved on the flanks with an electric razor 24 h before application. 50 mg of gel were applied once a day to each flank for 10 d. 24 h after the last application of gel the animals were sacrificed and inguinal white adipose tissue (WATi) was removed and analyzed for browning marker expression by qPCR, western blot and histologically after hematoxylin and eosin, as well as UCP1 antibody staining.

4.3.13 Preparation of histologic Sections

Tissue samples were fixed in 4% paraformaldehyde solution, dehydrated with ethanol (EtOH), embedded in paraffin and cut with a microtome. Sections were stained with hematoxylin and eosin (H&E) and with UCP1 specific antibodies, respectively.

4.3.14 Isolation of RNA and Real-time Polymerase Chain Reaction (qPCR)

Tissues were homogenized with Trizol for mRNA extraction and treated with chloroform with subsequent precipitation by addition of propan-2-ol and washing with 75% EtOH. The concentration of isolated RNA was spectrophotometrically analyzed with a Nanodrop 200 (ThermoFisher Scientific, Waltham, MA, USA).

Synthesis of cDNA was conducted with a ProtoScript II First Strand cDNA Synthesis Kit according to the manufacturer's instructions. Analysis of amplification was performed by staining with SYBR Green Master Mix and measurement on a QuantStudio 5 qPCR system (ThermoFisher, Waltham, MA, USA). The $2^{-\Delta CT}$ method was used to calculate the relative mRNA expression of genes normalized to the housekeeping genes Hypoxanthine Phosphoribosyltransferase 1 (HPRT) for murine- and Ribosomal Protein L13a (RPL13A) for human samples [90]. For primer sequences used please refer to Tables 2 and 3.

Table 2: Primer sequences used for qPCR of murine genes.

Name	Direction	Sequence 5'-3'
UCP1	Forward	TAAGCCGGCTGAGATCTTGT
	Reverse	GGCCTCTACGACTCAGTC
CIDEA	Forward	GTCAAAGCCACGATGTACGAGAT
	Reverse	CGTCATCTGTGCAGCATAGGA
PGC1α	Forward	CCCTGCCATTGTTAAGAC
	Reverse	GCTGCTGTTCCTGTTTTC
DIO2	Forward	GCGATGGCAAAGATAGGTGA
	Reverse	GAATGGAGCTGGGTGTAGCA
TNFα	Forward	CCCTCACACTCAGATCATCTTCT
	Reverse	GCTACGACGTGGGCTACAG
HPRT	Forward	GTCCCAGCGTCGTGATTAGC
	Reverse	TCATGACATCTCGAGCAAGTCTTT

Table 3: Primer sequences used for qPCR of human genes.

Name	Direction	Sequence 5'-3'
UCP1	Forward	TGCCCAACTGTGCAATGAA
	Reverse	CCAGGATCCAAGTCGCAAGA
CIDEA	Forward	GGGTCTCCAACCATGACAGG
	Reverse	GAGGGCATCCAGAGTCTTGC
PGC1α	Forward	CTGTGTCACCACCCAAATCCTTAT
	Reverse	TGTGTCGAGAAAAGGACCTTGA
DIO2	Forward	GTCACTGGTCAGCGTGGTTTT
	Reverse	TTCTTCACATCCCCCAATCCT
RPL13A	Forward	GGACCGTGCGAGGTATGCT
	Reverse	ATGCCGTCAAACACCTTGAGA

4.3.15 Western Blot

To isolate proteins a radioimmunoprecipitation assay lysis buffer containing 50 mM Tris pH 7.5, 150 mM sodium chloride, 1% NP-40, 0.5% sodium deoxycholate, 0.1% sodium dodecyl sulfate, 0.1 mM EDTA, 0.1 mM EGTA, 1 mM Na_3VO_4, 10 mM NaF, containing a protease inhibitor cocktail (Roche, Basel, Switzerland), was used. The protein content was quantified by Bradford assay. Proteins were separated by 12% SDS-PAGE and transferred to a nitrocellulose membrane. For immunoblot primary antibodies of UCP1 (Sigma-Aldrich, Taufkirchen, Germany) and Calnexin and secondary anti-rabbit antibodies were used. Amersham ECL Western Blotting reagent was used to visualize proteins and detection was performed with an ImageQuant LAS 4000 mini (GE Healthcare, Chicago, IL, USA). Quantification was conducted using ImageJ software [91].

4.3.16 Statistical Evaluation

Tests for statistical significance were conducted using the software GraphPad Prism 8. Depending on the number of samples in each group, whether multiple comparisons needed to be accounted for and whether groups were of the same standard deviation, different tests for statistical significance were performed, that are properly denoted in the respective sections of the results.

5 Results & Discussion

5.1 *Browning of Adipose Tissue by topical Delivery of Adrenoreceptor Agonists*

5.1.1 Formulation of β2ADR Agonists

The primary receptor involved in activation of human BAT and browning of WAT is still disputed and recent findings have suggested the β2ADR to be the dominant receptor in humans instead of the β3ADR [58,92].

To investigate the feasibility of browning by topical delivery of β2ADR agonists, the registered APIs formoterol, clenbuterol, and salbutamol were chosen due to their different potency, receptor selectivity, and classification as long- (LABA) or short acting beta agonists (SABA), as well as their varying solubility profiles (Tab. 4).

Table 4: Classes of tested agonists and their respective affinities to human βADR [93,94]

Substance	**Class**	**Log K_D**		
		β1	β2	β3
Formoterol	LABA	-6.11	-8.63	-5.82
Clenbuterol	LABA	-6.62	-7.90	-5.35
Salbutamol	SABA	-4.68	-6.01	-3.98

Identifying suitable solvent systems for FF to obtain liquid or semisolid formulations was explored first as it is a highly selective and potent agonist, that is however poorly soluble in water and lipids. Thus, despite its reputation as a doping agent, formulations of CLB were explored as an alternative, as it is commercially available in its free base form, which is still poorly soluble in water, but exhibits a preferable solubility in various excipients compared to FF, even allowing for formulation of a patch of CLB [95]. In the end, SS as a commonly used SABA with well-known risk profile was formulated as a compound of high water solubility.

The prepared formulations were investigated for their permeative potential over human skin *in-vitro* and were partially tested in a mouse model for their efficacy on browning adipose tissue *in-vivo*.

5.1.1.1 Formoterol Fumarate Dihydrate

Formoterol was used in a study by Blondin et al. in which they challenged the β3ADR as the primary receptor for activating BAT and driving lipolysis of WAT and instead proposed a

mediation by β2ADR [58]. Furthermore, the oral application of formoterol in doses typically used in inhalative asthma therapy increased energy expenditure and fat oxidation in a clinical study, however without elucidating the localization of these processes [96]. In contrast, the effects on WATi were studied by Ohyama et al. by daily intraperitoneal injection of C57Bl/6 mice with 1 mg/kg formoterol for one week, which significantly increased mRNA expression of UCP1, CIDEA and DIO2 [97]. Although compared to injection of the β3-agonist CL316234 in the same dose, the expression of UCP1 was more than a magnitude lower for formoterol, the occurrence of multilocular adipocytes in WATi was observed in the same study. Therefore, FF was chosen as a β2ADR agonist for browning by topical drug delivery.

Table 5: Solubility of formoterol fumarate dihydrate in water, tetrahydrofuran (THF), dimethyl isosorbide (DMI), propylene carbonate (PC), Transcutol® (TC), Miglyol® 812 (MCT812), cocoyl caprylocaprate (CC), ethanol (EtOH), polyethylene glycol 300 (PEG300), propylene glycol (PG), dimethyl formamide (DMF), dimethyl sulfoxide (DMSO), and N-Methyl-2-pyrrolidone (NMP).

Solvent	Solubility [mg/mL]
Water	0.568
THF	0.960
DMI	0.773
PC	0.068
TC	6.992
MCT812	-
CC	-
EtOH	7.259
PEG300	15.589
PG	>25
DMF	>25
DMSO	>25
NMP	>25

Strikingly, FF was insoluble in the apolar excipients MCT812 and cocoyl caprylocaprate as no amount of dissolved FF could be detected, which is surely due to its salt form (Tab. 5). Then again, the solubility of FF was also low in highly polar PC. In water, THF, and DMI the solubility was below 1 mg/mL and about a magnitude higher in polar protic solvents containing alcoholic groups, such as EtOH or TC: The highest solubility was found in polar

aprotic solvents, such as DMSO, DMF, and NMP. Thus, the permeation from a 6.17% (*w/w*) (equivalent to 5% formoterol free base) solution in pure DMSO across human abdominal skin was assessed in a first feasibility study, resulting in a flux of 8.2 ± 2.4 µg/(cm²×h) with a lag time of 0.8 ± 0.6 h (Fig. 7).

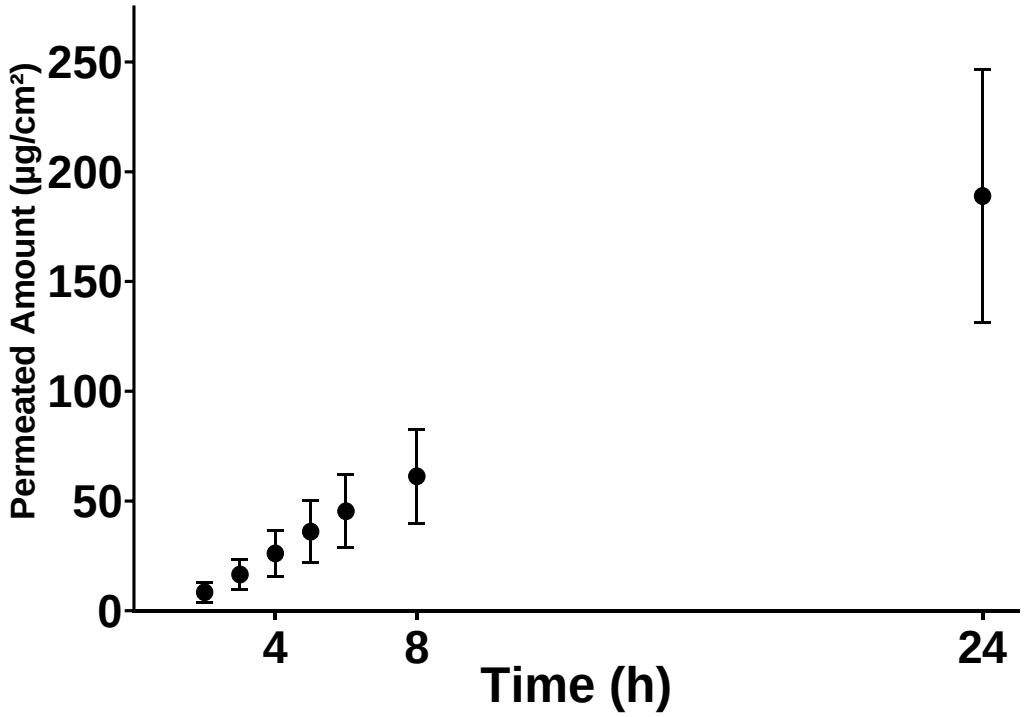

Figure 7: Permeation time profile of formoterol fumarate dihydrate from a 6.17% (*w/w*) solution in pure dimethyl sulfoxide. Data is presented as mean ± SD, n = 6.

Permeation experiments on rat skin with FF in different solvents, such as PG, 50% EtOH, or N-Methyl-2-pyrrolidone (NMP), showed a similar need of the polar aprotic solvent NMP to achieve sufficient solubilization and permeability [98]. This agrees with a permeation experiment conducted by us with 3% (*w/w*) FF in neat PG, in which no detectable amount permeated human skin in 24 h. In further studies by the same group transdermal patches of FF were prepared with NMP and l-menthol as permeation enhancers. Although application of a formulation containing each 12% NMP and l-menthol on rats *in-vivo* resulted in quantifiable plasma concentrations, only amounts in the nanogram range from formulations containing at the most 7.7% NMP and 22.1% l-menthol were found to permeate human skin *in-vitro* [99,100]. Furthermore, NMP is classified as a reproductive toxicant and the presented results thus highlight DMSO as an alternative base or permeation enhancer to NMP in delivery of FF [101]. Due to this dependance on presence of polar aprotic solvents

and the availability of alternative β2ADR agonists, further work was focused on these compounds with superior solubility profile.

5.1.1.2 Clenbuterol

Due to the poor solubility of FF in pharmaceutically acceptable excipients or permeation from them and the indicated dependence on polar aprotic permeation enhancers, clenbuterol was chosen as a rather lipophilic β2-agonist with low molecular weight. Studies with WT and UCP1 deficient C57Bl/6 mice revealed that injection of clenbuterol increased oxygen consumption in the WT group to a greater extent than in UCP1 deficient mice compared to saline respectively, which was attributed to the activation of BAT [102]. Furthermore, CLB was previously shown to increase lipolysis in rat adipocytes in cell culture, hinting at a potential effective use in weight loss [105]. The solubility of clenbuterol was determined in polar solvents such as propylene carbonate, water, binary mixtures of water with EtOH, TC and DMI, as well as in the neat apolar excipients MCT812 and IPM (Tab. 6-7).

Table 6: Solubility of clenbuterol in water, isopropyl myristate (IPM), Miglyol® 812 (MCT812), and propylene carbonate (PC). For dimethyl isosorbide (DMI), polyethylene glycol 300 (PEG300), propylene glycol (PG), Transcutol® (TC), and ethanol (EtOH), the solubility was above 25 mg/mL. Data is presented as mean ± SD; n = 3.

Solvent	Solubility [mg/mL]
Water	0.191 ± 0.009
IPM	4.261 ± 0.099
MCT812	6.582 ± 0.349
PC	19.712 ± 0.227
DMI	> 25
PEG 300	> 25
PG	> 25
TC	> 25
EtOH	> 25

Table 7: Solubility of clenbuterol in binary mixtures of water with increasing amounts of ethanol (EtOH), dimethyl isosorbide (DMI), and Transcutol® (TC). Data is presented as mean ± SD; n = 3.

Volume Fraction of Solvent in Water (%)	**Solubility [mg/mL]**		
	EtOH	TC	DMI
12.5	-	1.188 ± 0.016	1.305 ± 0.106
25	0.344 ± 0.020	2.147 ± 0.025	2.323 ± 0.078
50	2.475 ± 0.355	5.590 ± 0.056	10.762 ± 0.022
75	15.448 ± 1.048	19.660 ± 1.404	52.538 ± 1.705

As a result of its low water solubility, solutions of clenbuterol in binary solvent mixtures of water with the known permeation enhancers EtOH, TC, and DMI, as well as a solution based on EtOH and IPM were prepared to assess their ability to facilitate clenbuterol permeation. For vehicles in EtOH the drug load of clenbuterol was set to 1%, while DMI and TC containing vehicles had to be adjusted to 0.1 and 0.4% respectively, due to reduced solubility. The exact compositions and their code are given in Table 8. In FDC experiments, the EtOH containing formulations showed the highest permeated amounts after 24 h, albeit connected to high lag times (Fig. 8, Tab. 8).

Table 8: Compositions, resulting flux and extrapolated lag times of the clenbuterol (CLB) formulations containing water, ethanol (EtOH), Transcutol® (TC), isopropyl myristate (IPM), and dimethyl isosorbide (DMI), tested in FDC permeation experiments. Data is presented as mean ± SD; n = 3-6.

Code	**% (*w/v*) CLB**	**% (*v/v*) Solvent**					**Flux (µg/(cm²×h))**	**Lag Time (h)**
		H_2O	EtOH	TC	IPM	DMI		
EtOH_IPM	1	-	90	-	10	-	32.45 ± 5.85	7.3 ± 0.1
EtOH_W	1	25	75	-	-	-	12.68 ± 0.60	5.8 ± 0.6
TC_W	0.4	50	-	50	-	-	1.83 ± 0.26	1.4 ± 0.9
DMI_W	0.1	87.5	-	-	-	12.5	1.37 ± 1.14	20.3 ± 1.5

In contrast, for the DMI containing formulation, CLB was only detectable in the receiver after 22 h, resulting in the lowest permeated amount and the longest lag time of the tested formulations. The TC containing formulation showed the lowest lag time of 1.4 h and a flux of 1.8 µg/(cm²×h). As the oral dose of CLB for the treatment of asthma is only 40 µg per

day and the TC formulation showed similar permeated amounts to this oral intake after 24 h, as well as a low lag time it was chosen for further *in-vivo* experiments in mice [103,104].

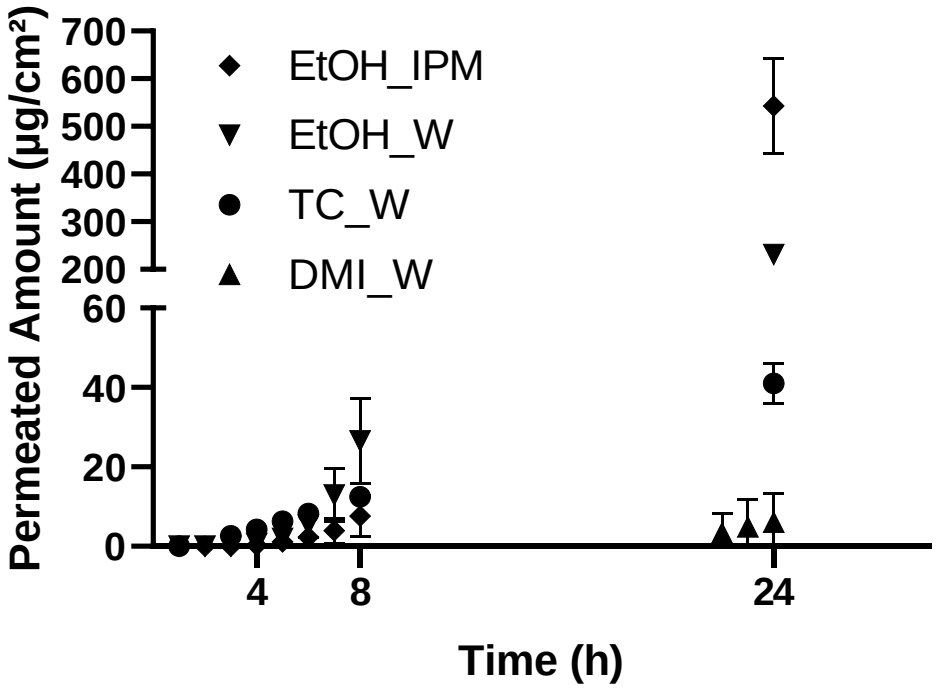

Figure 8: Permeation time profiles of clenbuterol from four binary mixtures of ethanol (EtOH), water (W), Transcutol® (TC), and dimethyl isosorbide (DMI). For exact compositions please refer to Tab. 8. Data is presented as mean ± SD; n = 3-6.

Histologic sections of inguinal tissue of mice treated with this formulation, gelled with an added on 2.5% (*w/w*) HPC-H for easier application, revealed morphologic changes from uni- to multilocular adipocytes, which is typical for brown and beige adipocytes (Fig. 9). However, no increase in UCP1 expression on the protein level could be observed in immunostained sections. On gene level, this was supported by the unchanged expression of UCP1 or DIO2 compared to placebo (Fig. 10). However, the browning markers CIDEA and

PGC1α were significantly increased over placebo treated controls (Fig. 10). TNFα was not increased when compared to control.

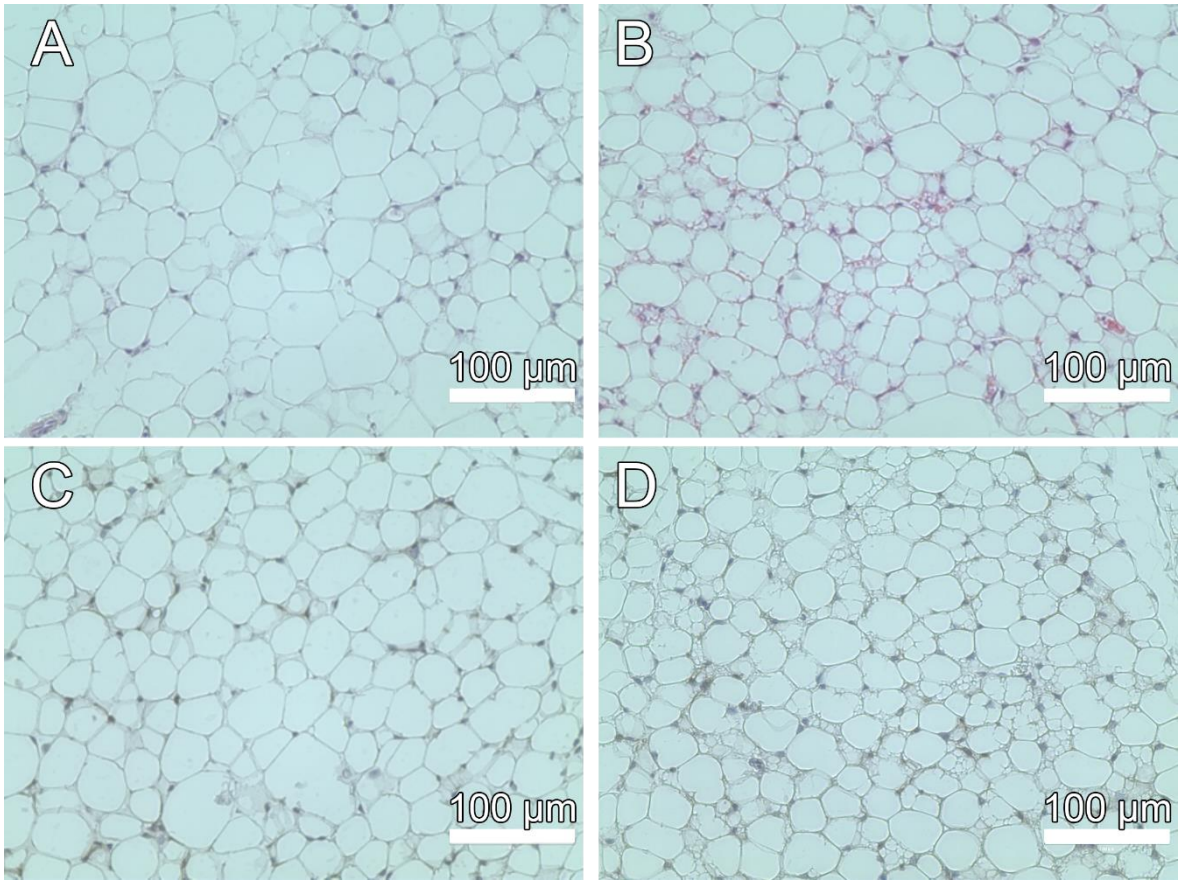

Figure 9: Histologic sections of inguinal white adipose tissue of mice after treatment with placebo and 0.4% (w/v) clenbuterol containing gel based on a 50/50 (%*v/v*) mixture of water and Transcutol® for 10 d. H&E stains showed an increase in lipid droplets and reduction in adipocyte size in verum treated mice **(B)** compared to placebo **(A)**. No differences in UCP1 expression from antibody-stained sections could be observed between placebo **(C)** and verum treated groups **(D)**. However, a change in cell morphology is visible in these sections as well.

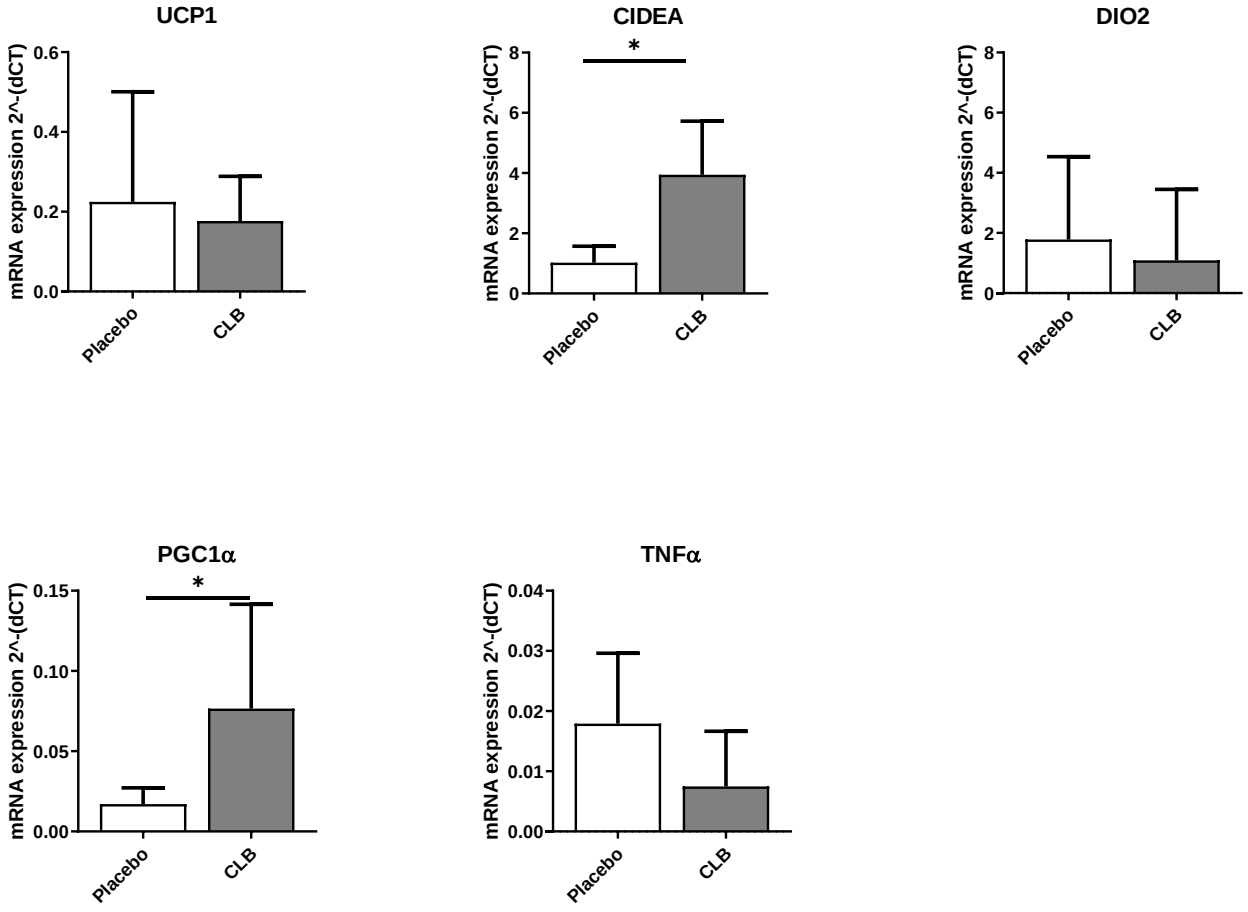

Figure 10: Treatment of mice with 0.4% (w/v) clenbuterol containing gel based on a 50/50 (%*v/v*) mixture of water and Transcutol® for 10 d significantly increased mRNA expression of the browning markers CIDEA and PGC1α, while UCP1, DIO2 and TNFα were not significantly changed in WATi compared to placebo. Data is presented as mean ± SD; n = 3-8. Analysis of significance was conducted by Student's t-test for CIDEA and by Welch's t-test for PGC1α to account for differing SD. *$p < 0.05$

Since CLB induced first signs of browning in murine WATi after exposition to only low doses of drug, as derived from FDC permeation experiments, the formulation of pressure-sensitive adhesive patches on polyacrylate and silicon base was explored as an alternative, extended-release approach. Assessment of drug solubility with PLM in strength escalation studies of clenbuterol in hydroxylated DuroTAK® 2510 (DT2510) and carboxylated DuroTAK® 387-2054 (DT2054) polyacrylate PSA, as well as amine compatible silicone BIO-PSA™ 7-4202 (BP4202) revealed a high solubility of clenbuterol in polyacrylate matrices whereas a 5% (*w/w*) drug load in BP4202 induced crystal growth already (Fig. 11). Between the polyacrylate matrices the hydroxylated matrix showed a lower solubility than the carboxylated one with an estimated solubility between 5 and 15%, whereas DT2054 displayed no crystal growth even at a drug load of 30%.

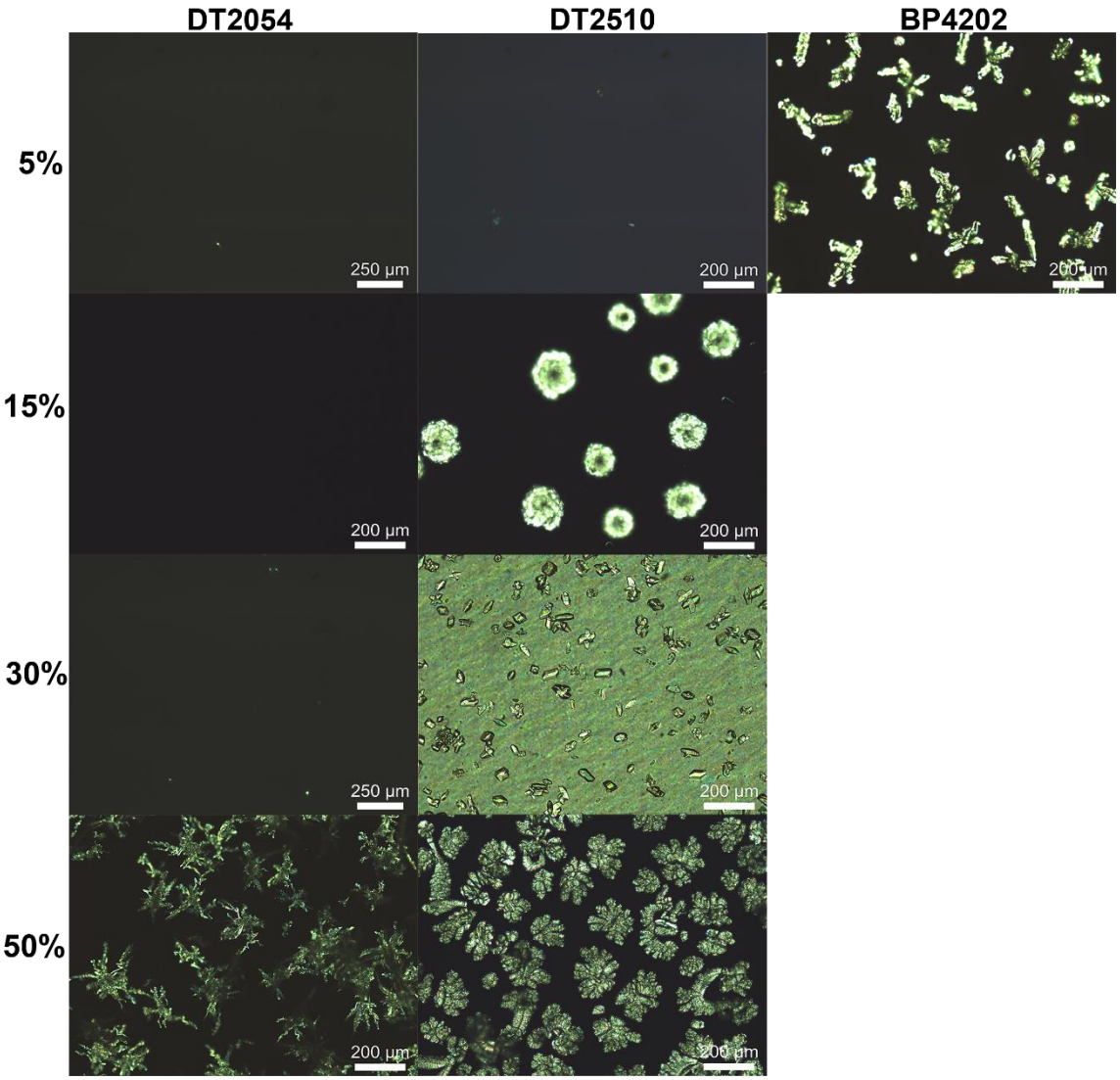

Figure 11: Polarized light microscopy images of DuroTAK® 387-2054 (DT2054), DuroTAK® 2510 (DT2510), and BIO-PSA™ 7-4202 (BP4202) matrices loaded with 5, 15, 30, and 50% (*w/w*) clenbuterol. No crystal growth could be observed in DT2054 matrix up to and including 30% drug load, whereas DT2510 showed crystal growth from 15% and BP4202 from 5% drug load.

Due to their drug loading potential the polyacrylate matrices were tested for their release across a non-retentive dialysis membrane. The permeation from both patches followed a matrix typical extended release kinetic as derived from the linearity when plotting the amount of drug against the square root of time (Fig. 12A). However, the permeated amount of clenbuterol from DT2510 was more than tenfold higher than from DT2054. This could be due to a strong interaction of the carboxy functions of DT2054 with the amine groups of

clenbuterol, which has also been observed in permeation studies of carboxy functionalized matrices with the APIs donepezil and tacrine [106,107].

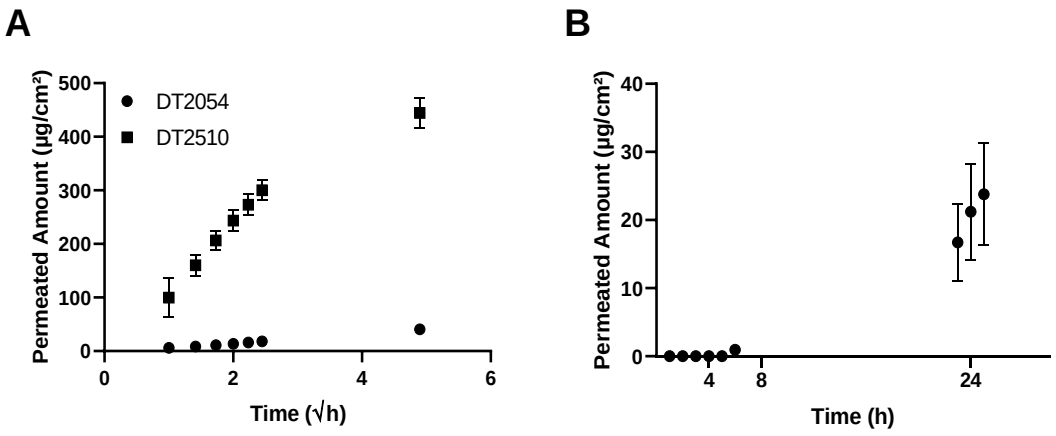

Figure 12: (A) Permeation time profiles of patches containing 5% (*w/w*) clenbuterol on DuroTAK® 387-2054 (DT2054) and DuroTAK® 387-2510 (DT2510) base across a dialysis membrane with 50 kDa molecular weight cutoff. **(B)** Permeation time profile of a patch with 5% (*w/w*) clenbuterol on DT2510 base across human abdominal skin dermatomed to a thickness of 400 µm. Data is presented as mean ± SD, n = 6.

Drug loads of roughly 13% (*w/w*) could be achieved by Göpferich et al. by incorporating clenbuterol in thin films of the neutral polyacrylate matrix Eudragit® NE30D, with similar crystal growth occurring at higher concentrations [108]. The group further proved their films to deliver clenbuterol across isolated human cadaver SC and provide detectable plasma concentrations *in-vivo* [109,110]. However, the presented release of their thin film was inferior to the herein presented results across a dialysis membrane and addition of a tackifier would surely be needed for such a film to be sufficiently adhesive to skin. Thus, the patch containing 5% (*w/w*) clenbuterol in DT2510 was chosen to be tested on human skin and 23.5 µg were found to permeate in 24 h with a flux of 3.5 ± 1.4 µg/(cm²×h) observed between 23 and 25 h, connected to an extrapolated lag time of 17.6 ± 2.1 h, although first amounts of clenbuterol were already detected in the receiver after 6 h (Fig. 12B). This could be explained by the provided occlusion of the patch that might have altered the hydration of the upper skin layers over time, continuously increasing partitioning of clenbuterol into the skin until an equilibrium was reached.

5.1.1.3 Salbutamol Hemisulfate

Recently, adding on to the results of Blondin et al., the effect of salbutamol on the activation of human BAT *in-vivo* was highlighted by Straat et al., who found that a bolus injection of salbutamol increased energy expenditure and glucose uptake in BAT [58,92]. In contrast to the long acting CLB and FF, salbutamol is a short acting beta agonist and was found to be decently soluble in water in its hemisulfate form and thus was investigated as an alternative β2ADR agonist with a known and well tolerated risk profile [94]. Furthermore, first studies of transdermal SS delivery had already been conducted, in which SS was formulated as a transdermal patch, achieving significant permeation across human and murine skin *in-vitro*, as well as decent plasma concentrations after *in-vivo* application that could improve the pulmonary function of the human test subjects [111–113].

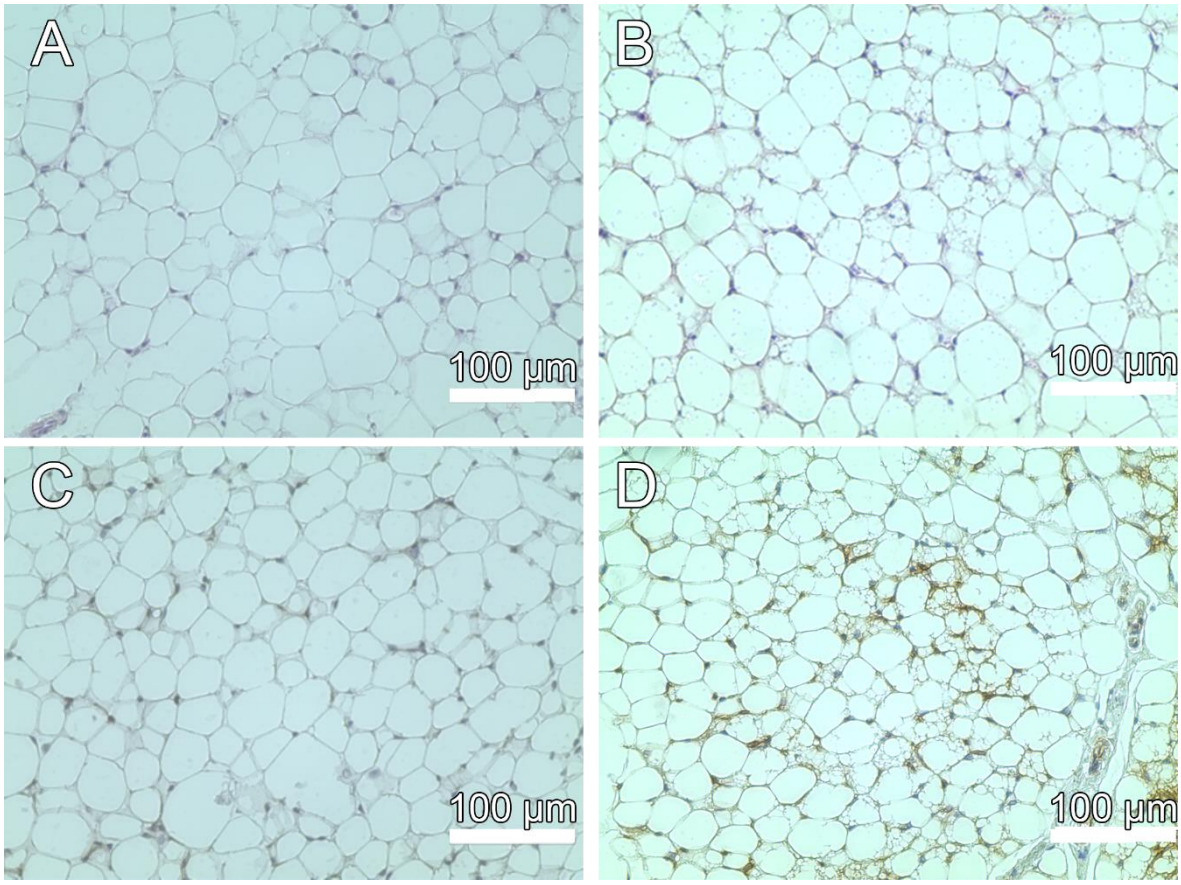

Figure 13: Histologic sections of inguinal white adipose tissue of mice after treatment with placebo or 10% (*w/w*) salbutamol hemisulfate containing gel, referring to the weight of solution, on base of a 50/50 (%*w/w*) mixture of water and ethanol for 10 d. H&E stains showed an increase in lipid droplets and reduction in adipocyte size in verum treated mice **(B)** compared to placebo **(A)**. No differences in UCP1 antibody-stained sections could be observed between placebo **(C)** and verum treated groups **(D)**.

Previous studies concluded that salbutamol hemisulfate was decently soluble in binary mixtures of water and short chain alcohols, and Lee et al. tested the permeation of SS across human skin, achieving high human skin permeation of over 400 µg/cm² in 24 h from solutions with EtOH as alcohol component [114,115].

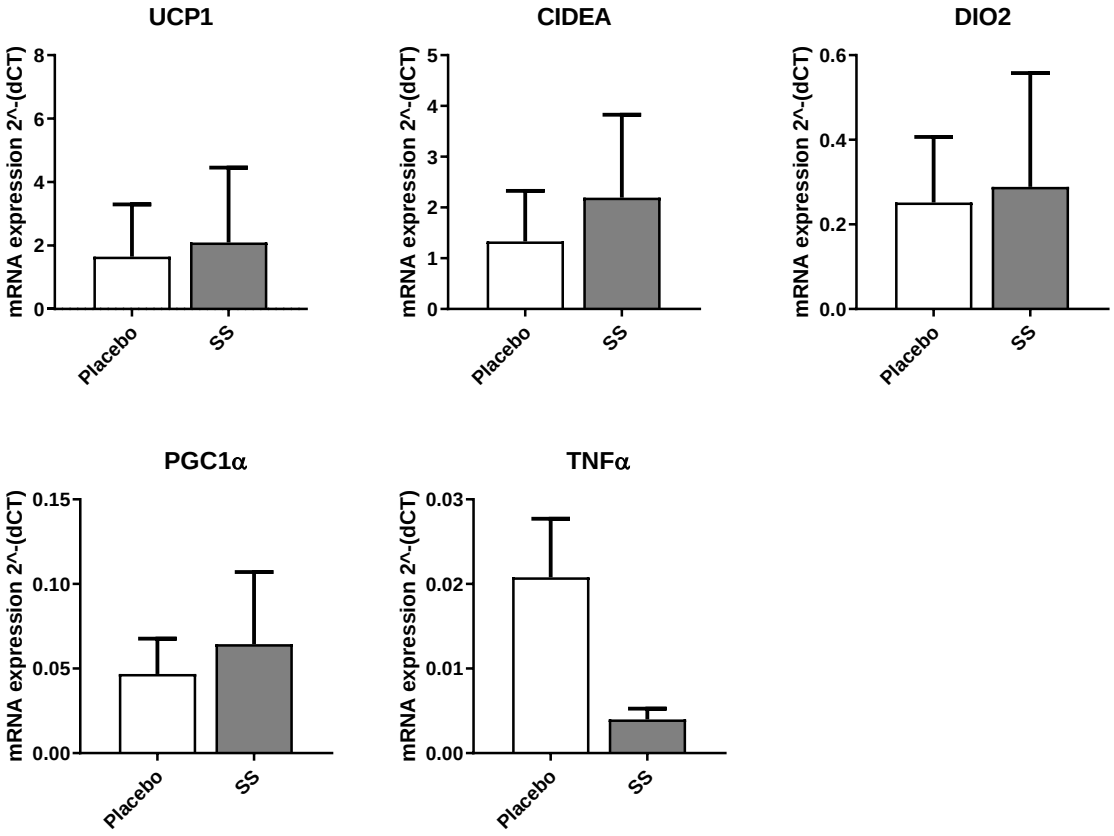

Figure 14: Treatment of mice with 10% (*w/w*) salbutamol hemisulfate (SS) containing gel, referring to the weight of solution, on base of a 50/50 (%*w/w*) mixture of water and ethanol for 10 d did not significantly increase mRNA expression of browning markers in WATi, although verum treated groups showed an increased trend for all browning marker genes. TNFα was not increased compared to placebo. Data is presented as mean ± SD; n = 8. Analysis of significance was conducted by Student's t-test.

Adding on to these results a solution of 10% (*w/w*) salbutamol hemisulfate in a 50/50 (%*w/w*) mixture of water and EtOH was gelled with 5% (*w/w*) HPC-H, added on to the total weight of solution. Application of this gel on mice *in-vivo* resulted in a histologically observable small induction of multilocular adipocytes in WATi (Fig. 13). However, analogous to the clenbuterol treated mice, no induction of UCP1 was observable by immunostaining. This was confirmed by analysis of WATi for expression of browning gene markers by qPCR, in which no significant, albeit increased trend in upregulation was observed (Fig. 14).

Despite the high permeated amount from solution shown by Lee et al. *in-vitro*, the rapid evaporation of EtOH on the murine skin *in-vivo* could have resulted in inadequate time for permeation enhancement and thus insufficient amounts of SS in WAT, especially due to its lower potency compared to CLB [114]. This is further supported as a 10% purely aqueous solution of SS was shown by the same group to allow only around 2 µg/cm² of SS to permeate human skin in 24 h [114]. Thus, the addition of a less volatile permeation enhancer would surely improve delivery *in-vivo*.

In a first attempt, high permeated amounts of 212.2 ± 84.4 µg/cm² SS after 24 h were achieved by a gel of 2.5% (*w/w*) SS on solvent base of a 50/50 (%*w/w*) mixture of water and DMSO, gelled with an additional 4% (*w/w)* HEC 250, referring to the total weight of solution (Fig. 15). Comparing this solvent system to the one on base of EtOH, the permeated amount was almost doubled, when normalized to the concentration of SS. Accordingly, formulations based on binary mixtures of water and DMSO could be more suitable platforms for further iterations that could be tested *in-vivo*. Alternatively, further known permeation enhancers, such as PG or TC with adequate volatility could be explored.

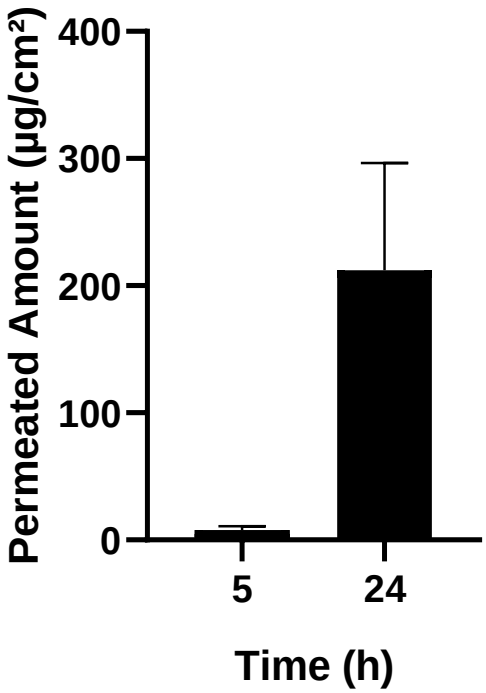

Figure 15: Permeation of salbutamol hemisulfate from a 2.5% (*w/w*) gel, referring to the weight of solution, on base of a 50/50 (%*w/w*) mixture of water and dimethyl sulfoxide over 400 µm thick dermatomed human abdominal skin . Data is presented as mean ± SD, n = 6.

5.1.2 Formulations of β3ADR Agonist Mirabegron

5.1.2.1 Mirabegron Solutions and Gels for topical Delivery

The application of a supratherapeutic dose of the β3ADR MIR was found to induce activation of BAT in humans *in-vivo* [53]. High local doses from topical application could thus be assumed to result in similar results, circumventing associated side effects. However, due to the low water solubility of mirabegron and the non-observable permeation from a purely aqueous suspension across human skin in a pretrial, delivery from a solely aqueous vehicle was deemed insufficient for reaching the subcutaneous tissue. Thus, MIR's solubility was determined in various organic solvents and excipients (Tab. 9). Organic solvents from the classes of polar aprotic solvents, such as NMP and DMSO, short chain alcohols like MeOH and EtOH, as well as the glycols PG, PEG 300 and TC allowed high amounts of MIR to be dissolved. In contrast, the solubility of MIR in more apolar excipients like Maisine® CC, IPM or Squalene was poor.

Table 9: Solubility of mirabegron in ethanol (EtOH), methanol (MeOH), N-Methyl-2-pyrrolidone (NMP), dimethyl sulfoxide (DMSO), propylene glycol (PG), polyethylene glycol 300 (PEG300), Transcutol® (TC), Maisine® CC, isopropyl myristate (IPM), and squalene.

Solvent	Solubility [mg/mL]
EtOH	>30
MeOH	>100
NMP	>100
DMSO	>100
PG	>50
PEG300	>50
TC	>100
Maisine® CC	2.8
IPM	0.100
Squalene	0.013

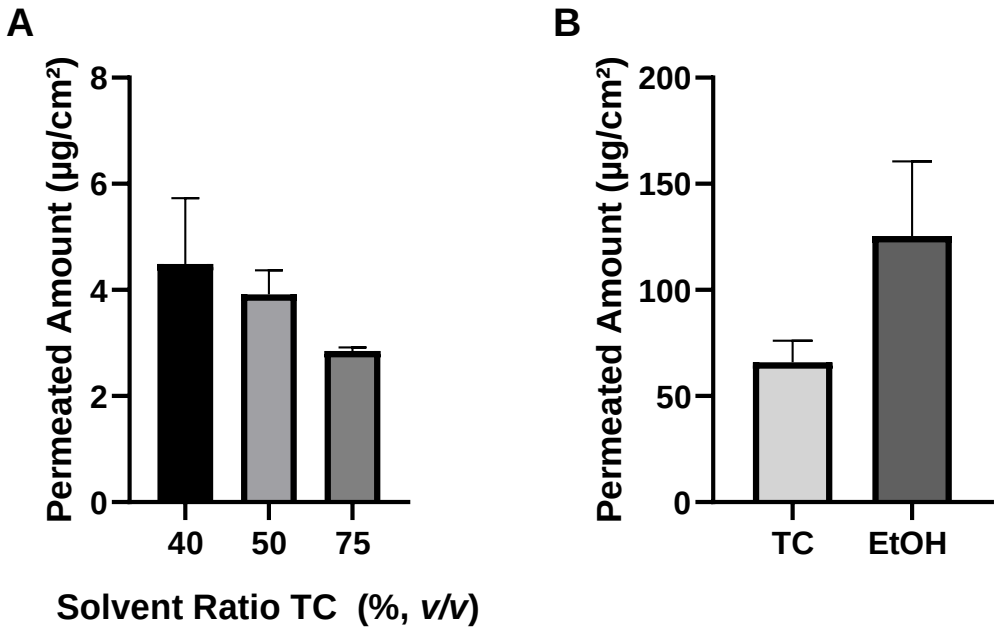

Figure 16: Permeated amount of mirabegron across human abdominal skin dermatomed to a thickness of 400 µm after 24 h from **(A)** 3% (*w/w*) solutions in binary mixtures of Transcutol® (TC) and water and **(B)** of 10% (*w/w*) solutions of mirabegron in a 50% (*w/w*) binary mixture of TC and ethanol (EtOH) with dimethyl sulfoxide respectively. Data is presented as mean ± SD; A) n = 5; B) n = 4-6.

As TC is commonly used as a permeation enhancer in transdermal delivery systems, binary mixtures of TC and water were prepared and the permeated amount of a 3% (*w/w*) solution of MIR after 24 h was assessed (Fig. 16A). Despite the high MIR concentration in the donor compartment for each mixture, no more than 4.5 µg of MIR were detected in the receiver compartment from the best performing mixture. Interestingly the permeated amount of MIR decreased with increasing amounts of TC. To the same end, permeated MIR out of a 3% (*w/w*) solution in neat TC or the chemically similar PG was not detectable in the receiver after 24 h under the same experimental conditions. Furthermore, when dissolved in a binary mixture of either TC or EtOH with an equal amount of the potent penetration enhancer DMSO, the permeated amount from the TC vehicle was almost half of the EtOH one, ruling out usage of TC for further formulations (Fig. 16B).

Therefore, EtOH was chosen as a more suitable solvent base for MIR, because of its known penetration enhancement potential, known risk profile and sufficient solubility. However, when used as neat solvent only 2.9 µg of MIR permeated the skin from a 3% (*w/w*) solution in 24 h (Data not shown). To explore addition of another permeation enhancer other than DMSO, isopropyl myristate was added in a concentration of 10% (*w/w*) referring to the

solvent mixture and a 3% (*w/w*) solution of MIR was tested. In contrast to neat EtOH, an amount of 381.5 ± 114.4 µg permeated after 24 h with a flux of 22.5 ± 7.4 µg/(cm²×h) (Fig. 17). Nevertheless, the lag time was found to be 6.8 ± 1.1 h and no MIR could be detected in the receiver in a follow up finite dose experiment, in which 10 µL/cm² of solution were applied.

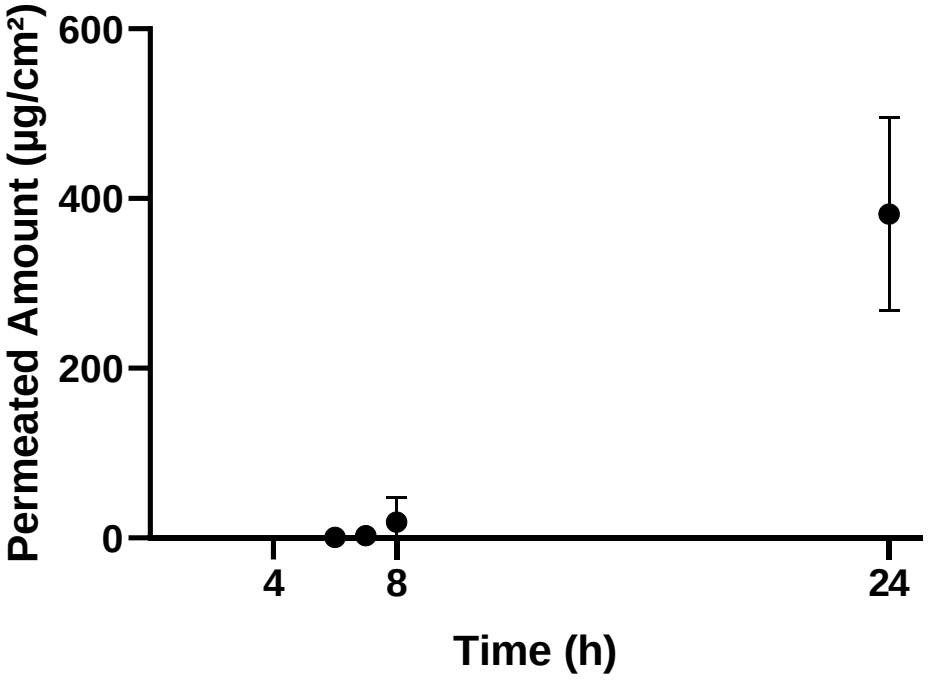

Figure 17: Permeation time profile of mirabegron from a 3% (*w/w*) solution in a binary mixture of Ethanol and isopropyl myristate (90/10, %*w/w*, referring to the solvent mixture) over human abdominal skin dermatomed to a thickness of 400 µm. Data is presented as mean ± SD, n = 6.

This was attributed to the rapid evaporation of EtOH and subsequent crystallization of MIR on the skin surface, rendering further partitioning into the upper layers of the SC impossible. To allow for a longer active delivery period on skin and the promising results of the binary mixture with EtOH, DMSO was chosen as primary solvent due to its low volatility, yet high skin permeability. Because the solubility of MIR in binary mixtures of DMSO with water was low and since EtOH proved to allow permeation of MIR in general, EtOH was chosen as co-solvent to maintain a high potential solubility of MIR in binary mixtures (Tab. 10). Furthermore, the formulations could benefit from an increase in active concentration upon rapid evaporation of EtOH after application, due to its high volatility, while DMSO would remain on the skin providing sufficient solubility on the surface and prolonged permeation enhancement. Permeation experiments with binary mixtures of 5, 10, and 50% (*w/w*) DMSO

content and neat DMSO were conducted. As the solubility of MIR in a 5% DMSO mixture was limited to roughly 25 mg/mL, the concentration of MIR was adjusted to 2% (*w/w*). For this formulation no permeation profile could be established, but 0.3 ± 0.5 µg of MIR were found to have permeated the skin after 24 h. The increased content of DMSO in the other mixtures allowed for a drug load of 5% in these systems. Gels of these solvent mixtures were prepared by addition of 5% (*w/w*) HPC-H to 10 and 50% DMSO and 2% (*w/w*) HEC250 to 100% DMSO, each referring the total weight of solution.

Table 10: Solubility of mirabegron in binary mixtures of dimethyl sulfoxide (DMSO) with water and ethanol (EtOH). Data is presented as mean ± SD; n = 3.

Volume Fraction of DMSO in Solvent (%)	**Solubility [mg/mL]**	
	Water	EtOH
1	0.175 ± 0.020	17.524 ± 0.693
5	0.278 ± 0.057	24.804 ± 0.274
10	0.484 ± 0.044	> 50

For all of these formulations, permeation time profiles could be established, revealing that significant amounts of mirabegron permeated the skin within 24 h. With rising DMSO content the permeated amount of MIR after 24 h increased from 38.7 ± 5.5 µg/cm² for 10%, over 95.7 ± 23.8 µg/cm² for 50% to 197.3 ± 38.6 µg/cm² in case of 100% DMSO as solvent component (Fig. 18A). Likewise, significant differences in flux could be observed with over a two- and fourfold increase from 1.96 ± 0.26 µg/(cm²×h) for 10% DMSO compared to 4.70 ± 1.13 µg/(cm²×h) for 50% and 9.19 ± 1.62 µg/(cm²×h) for 100% DMSO (Fig. 18B). The lag time sank from 4.67 ± 0.77 h, over 3.63 ± 0.66 h to 2.58 ± 0.68 h in the same order (Fig. 18C). This could be explained by the superior solubility of MIR in DMSO compared to EtOH.

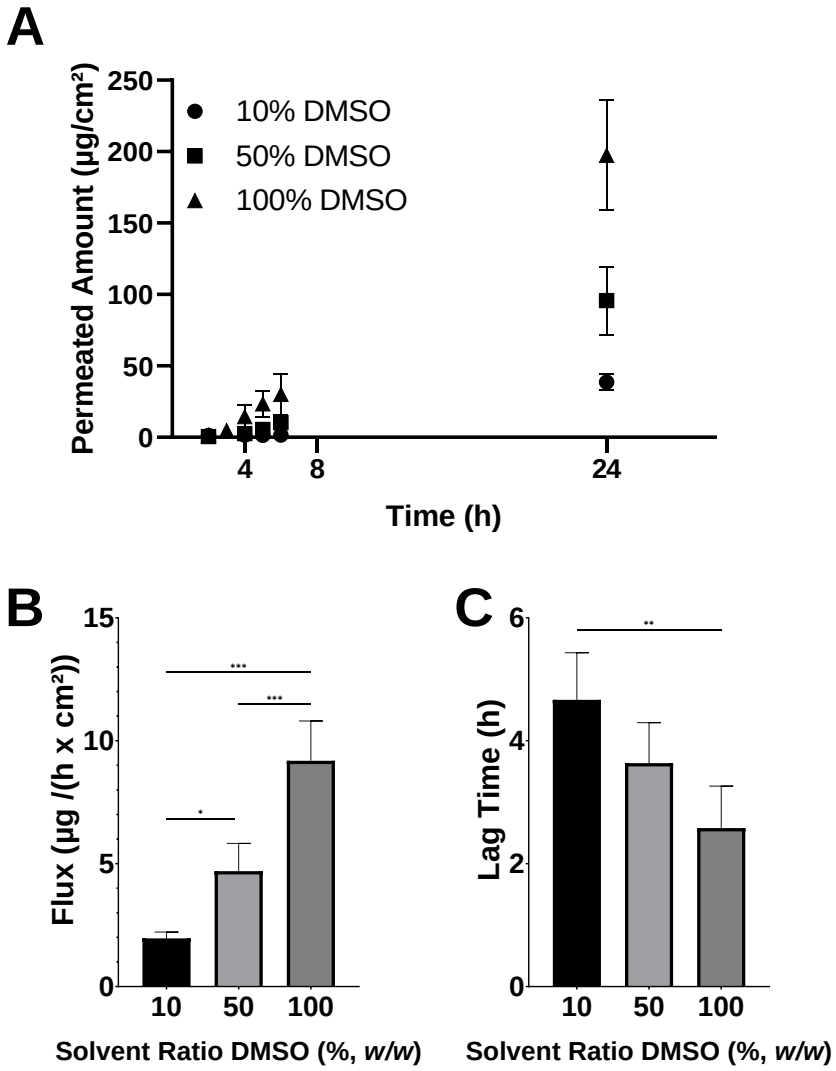

Figure 18: (A) Permeation time profiles of mirabegron (MIR) out of 5% (*w/w*) MIR containing gels on dimethyl sulfoxide (DMSO) and ethanol binary mixture base across human abdominal skin dermatomized to a thickness of 400 µm. **(B)** Resulting fluxes were significantly increased from 10 over 50 to 100% DMSO respectively. **(C)** Lag time was significantly reduced from 10 to 100% DMSO with a visible trend over 50%. Data is presented as mean ± SD, n = 4-6, Analysis of significance was conducted by one-way ANOVA corrected by Tukey's post-hoc test for multiple comparisons *p < 0.05, **p < 0.01, ***p < 0.001.

Resulting from a higher DMSO concentration in the vehicle and therefore permeation of it through the skin, the solubility properties of the skin could have been increasingly altered towards a favorable environment of MIR, promoting partitioning into the skin [116]. This is also confirmed by the insignificant increase of flux upon increasing the drug load in 50% DMSO from 5% over 10% to 20% (*w/w*) which resulted in similar permeation time profiles and no significant differences in permeated amount after 24 h and identical lag times which indicated that transport was rapidly saturated for each solvent system due to limited solubility of MIR in the skin. (Fig. 19). Furthermore, DMSO was reported to dehydrate lipid

membranes and to form pores of itself that could facilitate transport as a form of shunt route [117,118]. Similar dependency on DMSO content in formulation was found by Otterbach et al. for transport of Estradiol out of transdermal patches promoting the idea of a pull effect of DMSO [119]. Although DMSO was reported as a potential irritant to the skin, leading to erythema and further to foul breath even after dermal application, several *in-vivo* studies have shown that high concentrations in formulations are tolerated well and the most common adverse event upon application was dry skin in various clinical studies [11,120,121]. As an escalation of drug load did not lead to significantly increased permeation 5% were chosen for *in-vivo* and *ex-vivo* studies.

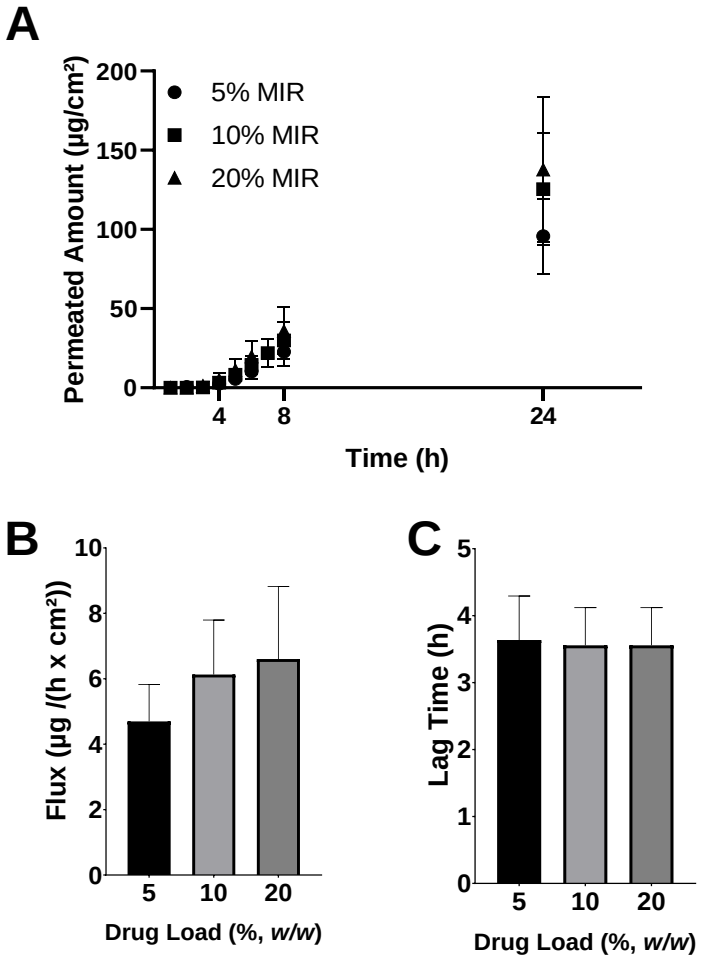

Figure 19: (A) Permeation time profiles of mirabegron (MIR) from gels with 5, 10, and 20% (*w/w*) drug load containing 50% (*w/w*) dimethyl sulfoxide and 50% (*w/w*) ethanol as solvent components each. Similar permeated amounts were observed for all formulations with insignificant differences in flux **(B)** and lag time **(C)**, respectively. Data is presented as mean ± SD, n = 5-6. Analysis of significance was conducted by one-way ANOVA corrected by Tukey's post-hoc test for multiple comparisons.

To reduce the number of animals in the *in-vivo* study only 10% and 100% DMSO based gels were chosen as placebo groups to gain a baseline readout from solvent exposure at high and low EtOH and DMSO contents.

Application of placebo gels to the flanks of WT C57BL/6 mice for 10 d did not induce any morphological signs of browning, such as multilocular morphology or reduction of adipocyte size and thus only one placebo is depicted for comparisons (Fig. 20).

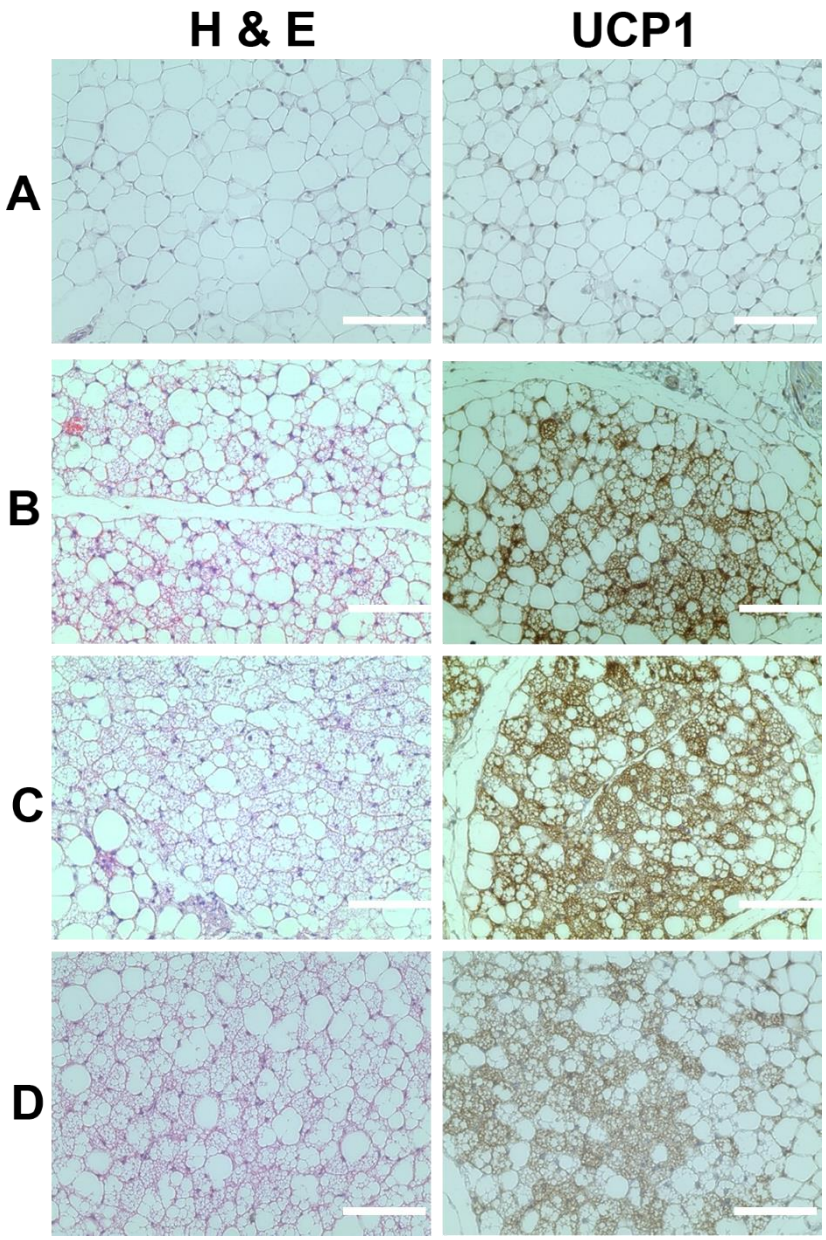

Figure 20: Representative images of H&E and UCP1 antibody-stained murine inguinal white adipose tissue after treatment with gels based on dimethyl sulfoxide (DMSO) and ethanol mixtures in form of **(A)** Placebo and 5% (*w/w*) mirabegron (MIR) containing gels, referring to the weight of solution with **(B)** 10%, **(C)** 50%, and **(D)** 100% (*w/w*) DMSO content, referring to the solvent mixture. The size of adipocytes was reduced for MIR treated mice in comparison to placebo for every DMSO content. Likewise, the size of lipid droplets was reduced in the treated groups and the amount

of them increased. Immunostaining revealed increased expression of UCP1 for all MIR treated groups. Scale bar equals 100 µm.

In contrast, treatment with MIR containing gels led to a pronounced reduction in lipid droplet size inside the adipocytes and their amount increased. Accordingly, immunostaining for UCP1 revealed extensively stained areas for verum treated samples, while placebo treated samples resembled H&E stained ones. This confirmed successful browning of WATi for all tested formulations from a morphological perspective (Fig. 20) [32]. Furthermore, the expression of BAT specific gene markers was increased after each verum application. The mRNA expression for placebo treated groups was statistically indistinguishable for each gene as confirmed by Student's t-test and the results were therefore pooled for further analyses. The expression of UCP1 was significantly increased by 8.9-fold for 10% DMSO compared to placebo, as well as 12.9-fold for 50% DMSO. Only a 2.8-fold increase was observed for 100% DMSO, that statistically was insignificant (Fig. 21). For CIDEA significant changes were observed in form of a 4.5-, 5.4-, and 3.6-fold increase for 10, 50, and 100% DMSO over placebo, respectively. Treatment with 10 and 50% DMSO resulted in a significant 2.2- and 2.6-fold increase of PGC1α over placebo, respectively. As with UCP1, treatment with 100% DMSO showed an increasing trend over placebo. In contrast to the other browning markers, the expression of DIO2, as well as the inflammation marker TNFα, were not increased or even reduced compared to placebo for any gel.

Although the formulation containing neat DMSO as solvent component was expected to result in the highest browning marker gene expression, derived from the greatest flux from FDC experiments, UCP1 expression was markedly lower than both other verum gels and indifferent to placebo also for expression of PGC1α. However, the increased trends, significant increase in CIDEA expression and positive UCP1 antibody staining in histology sections (Fig. 20) and western blot (Fig. 22A) confirmed delivery of MIR and UCP1 expression. This inferior impact on mRNA expression could have been the result of β3ADR desensitization, which was reported previously for long term exposure to ligands, which would fit the constant delivery associated with transdermal application, that would be highest for 100% DMSO [122–124]. The removed stimulus could thus result in a reduced expression of browning markers downstream. The non-increased TNFα gene expression indicates a sufficient tolerability of the chosen formulations.

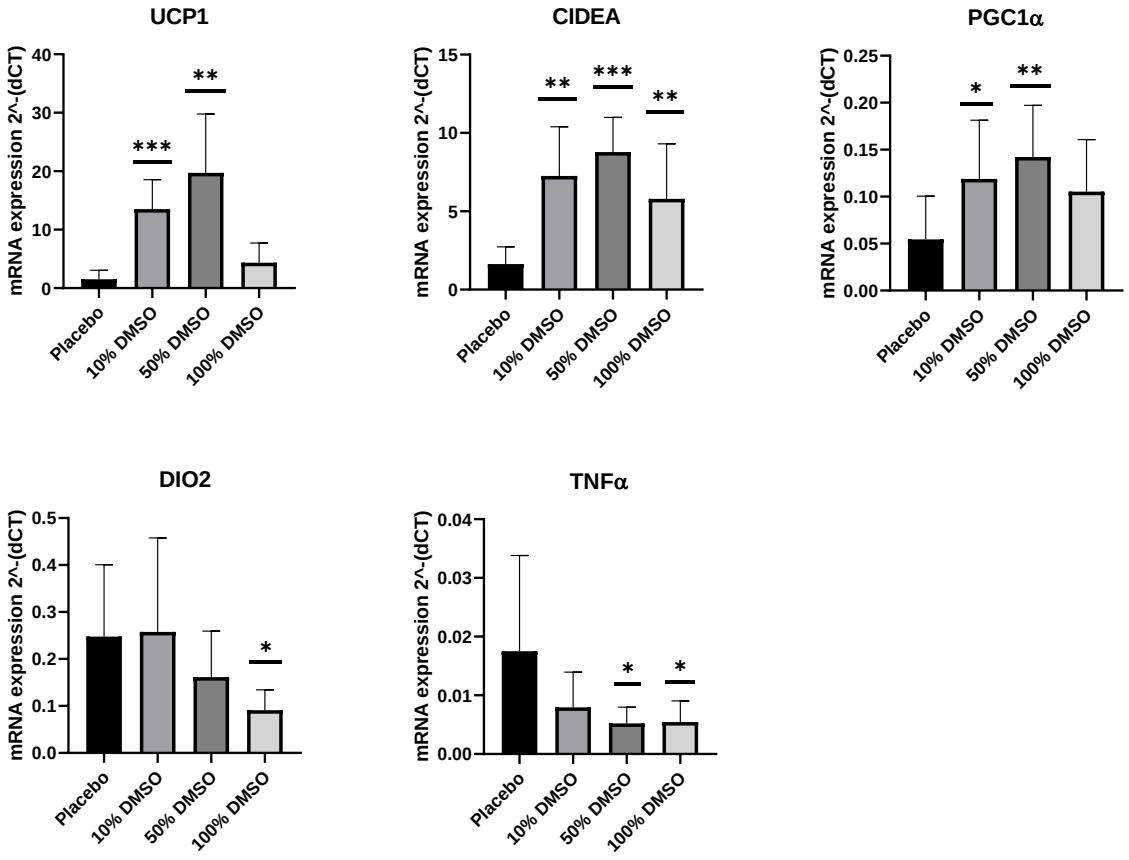

Figure 21: Treatment of mice with 5% (*w/w*) mirabegron containing gels, referring to the weight of solution, on dimethyl sulfoxide - ethanol base, containing 10%, 50%, and 100% (*w/w*) DMSO, referring to the solvent mixture, increased expression of adipose tissue browning markers UCP1, CIDEA, and PGC1α, while DIO2 and inflammation marker TNFα were equal to placebo or even reduced in inguinal white adipose tissue. Data are presented as mean ± SD; n = 8-14. Analysis of significance was conducted by Brown-Forsythe and Welch ANOVA corrected by Dunnett's T3 post-hoc test for multiple comparisons; *p < 0.05, **p < 0.01, ***p < 0.001 compared to Placebo.

Continuing from gene level, analysis of protein expression by western blot revealed bands of UCP1 for all MIR containing gels, while no bands were observable for both placebo gels (Fig. 22A). No differences were observed in quantitative analysis of UCP1 expression normalized to Calnexin between both tested placebos (analysis by Student's t-test). Therefore, they were pooled for the following analysis of verum groups. MIR treated groups displayed significantly increased expression of UCP1 compared to placebo, with no significant difference between them respectively, proving that all formulations effectively browned WATi and the delivered amount of 10% DMSO was already sufficient (Fig. 22B).

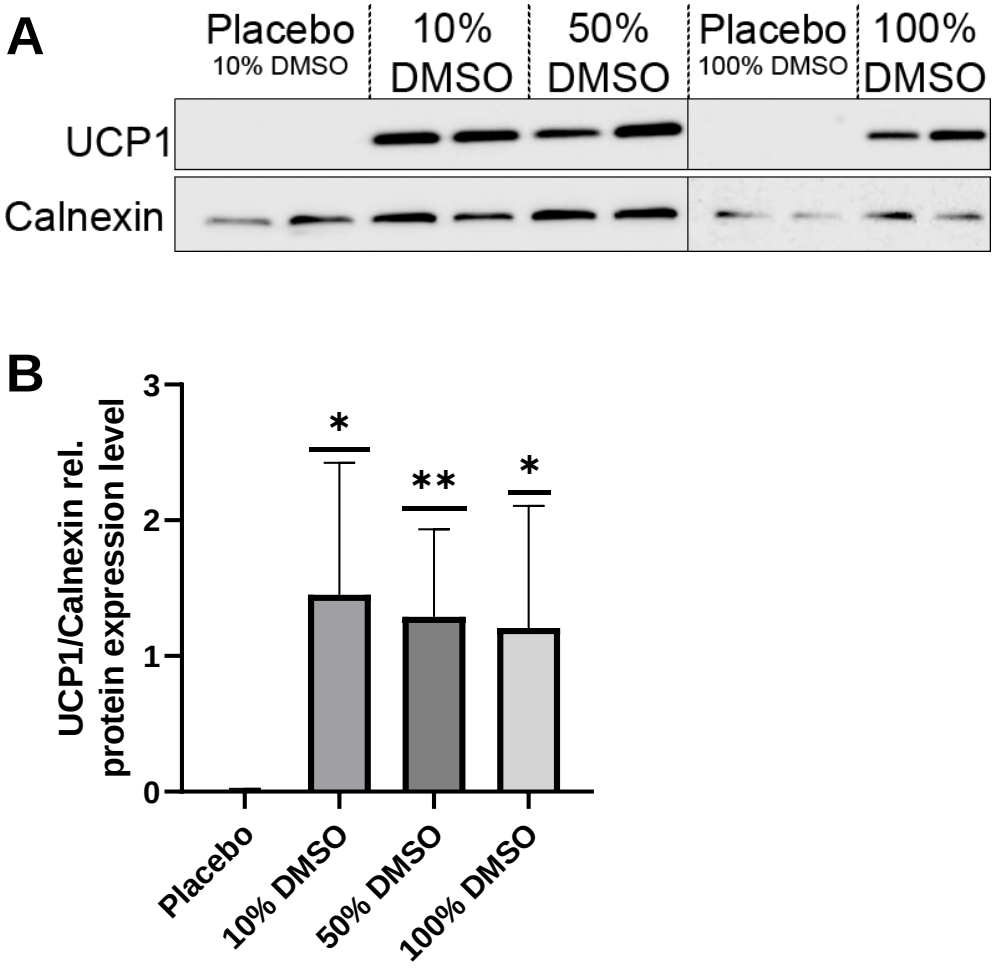

Figure 22: (A) Western Blot of UCP1 versus Calnexin of WATi of mice treated with gels based on mixtures of dimethyl sulfoxide (DMSO) and ethanol. Gels contained 10%, 50%, or 100% DMSO, referring to the solvent mixture. Gels contained either 5% (*w/w*) mirabegron (MIR) referring to the weight of solution or were applied as placebo. UCP1 bands are visible for verum treated groups in contrast to placebo treated groups. **(B)** Intensity analysis of protein expression level of UCP1 normalized to Calnexin significantly increased upon treatment with MIR containing gels compared to pooled placebo. Data are presented as mean ± SD; n = 8-11. Analysis of significance was conducted by Brown-Forsythe and Welch ANOVA corrected by Dunnett's T3 test for multiple comparisons; *$p < 0.05$, **$p < 0.01$ compared to Placebo.

Following the positive murine results, freshly excised human abdominal tissue was incubated with MIR gel and assessed for increases in browning gene markers. As human skin is considerably thicker than murine skin and the available time frame for tissue incubation was drastically shorter than for *in-vivo* experiments, the 100% DMSO gel was chosen for this feasibility study to supply the highest deliverable amount of MIR to the subcutaneous adipose tissue, despite the superiority of 50% DMSO on gene expression in the murine model [125]. To allow permeation of MIR through the whole skin and distribution into the subcutaneous WAT, samples were incubated for three days before

evaluation. A singular application of MIR gel increased gene marker expression of CIDEA, PGC1α, and DIO2 significantly with a 2.8-, 5.2-, and 6.1-fold increase, respectively (Fig. 23). Despite the level of UCP1 being elevated 2.7-fold, the increase was statistically insignificant (Fig. 23).

Although the increases in CIDEA, PGC1α, and DIO2 confirm the delivery of MIR to the subcutaneous WAT, the singular application of a clinically relevant dose could have been insufficient to induce a significant effect on UCP1 over the short duration of incubation. However, incubation of the excised tissue for more than three days would surely lead to its excessive decay and a cellular reaction to MIR stimulus might have already been impacted in the selected time frame. Thus, an extension of the experiment was virtually impossible and clinical trials with human subjects would need to be conducted to affirm the efficacy and tolerability in humans. Furthermore, recent studies have questioned the assumed primary role of the β3ADR as the target for adrenergic browning [57–60]. The low expression of the β3ADR in human WAT compared to rodents could therefore further explain the discrepancies between the mouse model and the *ex-vivo* results [126–128].

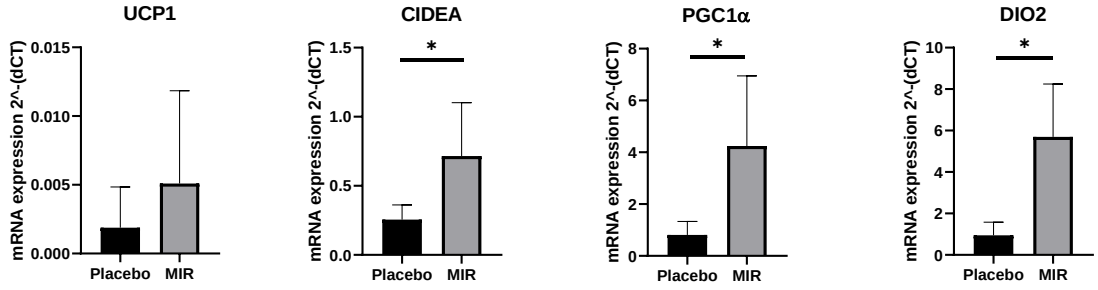

Figure 23: Effect of a singular treatment of freshly excised human skin with adhering subcutaneous adipose tissue with 5% (*w/w*) mirabegron (MIR) containing gel, referring to the weight of solution, on base of neat dimethyl sulfoxide on the expression of adipose tissue browning markers. CIDEA, PGC1α, and DIO2 were significantly upregulated compared to placebo after 3 d. Data are presented as mean ± SD; n = 3. Statistical analysis was conducted by one sided Mann Whitney test; *$p \leq 0.05$.

5.1.2.2 Mirabegron Nanoparticle Suspensions

Nanoparticles have been shown to be possible enhancers of dermal and transdermal permeation. To create nanoparticle suspensions, top down particle size reduction approaches e.g. via ball milling and bottom up approaches e.g. anti-solvent precipitation methods have been used [129]. Nanocrystals of the highly hydrophobic drug itraconazole were prepared by Willmann et al. by a ball milling top down procedure and stabilized through addition of steric and electrostatic stabilizers i.e. the neutral polymer HPC-SL and the non-ionic and ionic surfactants polysorbate 80 and SDS, respectively [130].

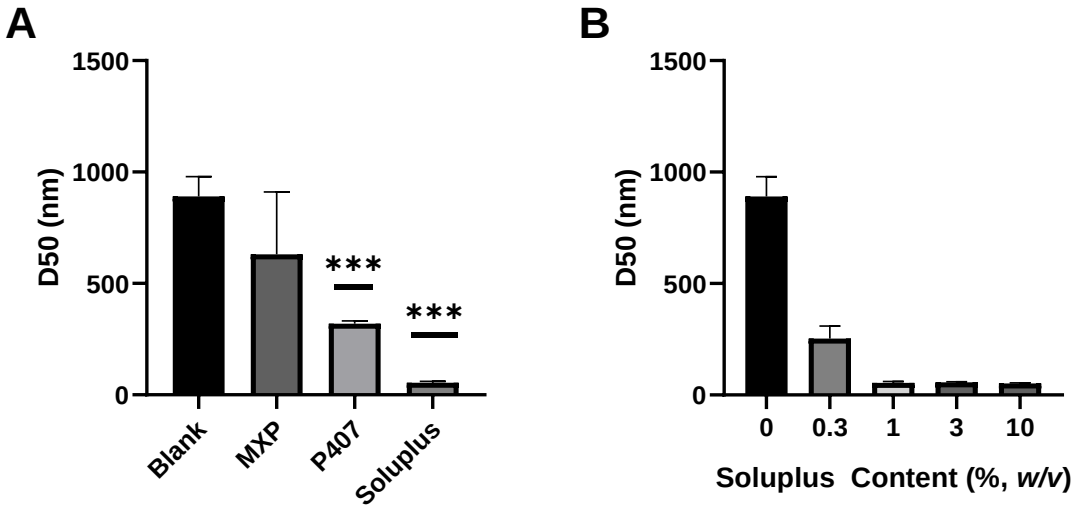

Figure 24: (A) Influence of 1% (*w/v*) Parteck® MXP (MXP), Poloxamer 407 (P407), and Soluplus® on the median particle size of MIR nanocparticles analyzed by dynamic light scattering. The presence of P407 and Soluplus® significantly reduced the particle size compared to neat suspension, while MXP showed no significant reduction. Data is presented as mean ± SD; n = 5. Statistical analysis was conducted by Brown-Forsythe and Welch ANOVA with Dunnett's T3 post-hoc test for comparing multiple solutions with added polymer versus blank solution, respectively, ***$p \leq 0.001$. **(B)** Increasing the amount of Soluplus® reduced the median particle size of MIR nanoparticles from neat suspension over 0.3% up to 1%. Further addition of Soluplus® to 3 and 10% led to no further decrease in median particle size, respectively.

This combination of excipients was taken up in this approach of sonoprecipitation of mirabegron from a 10% (*w/v*) solution of MIR in DMSO into an aqueous solution of 1% HPC-SL and 0.1% SDS, which is below its critical micelle concentration [131]. However, despite reports of synergistic stabilization potential of these compounds, the resulting particles only displayed a high median particle size of 890 ± 88.92 µm (Fig. 24A, Tab. 11) [132]. Thus, ternary mixtures of the previously used stabilizers with Poloxamer 407, Soluplus®, and Parteck® MXP, each in 1% concentration, were tested for their stabilizing

potential. The addition of Soluplus® drastically reduced the particle size, while P407 still showed a significant reduction and MXP addition yielded particles of similar size to neat suspension (Fig. 24A).

As Soluplus® was found to exhibit the highest stabilization potential, further concentrations were tested and a continuous decrease in particle size was observed from the neat suspension over 0.3 to 1%. Yet, higher concentrations of 3 and 10% Soluplus® did not result in a further reduction of the particle size (Fig. 24B, Tab. 11). A similar phenomenon was observed for the stabilization of Itraconazole nanocrystals by Poloxamer 407 in antisolvent precipitation, where increasing stabilizer concentrations led to a threshold in particle size, which was attributed to a reached unity of mixing and precipitation time [133]. Likewise, in this case a concentration of 1% Soluplus® could have been sufficient to effectively diffuse to and coat the surface of the precipitating drug and thereby inhibit condensation and coagulation, whereas the lower concentrations would only result in an incoherent coverage [133]. Soluplus® was used in concentrations of 1 to 1.5% in a study of Gajera et al., resulting in amorphous nanoparticles of clotrimazole with a median diameter below 150 nm in a sonoprecipitation process, highlighting the potential of low Soluplus® concentrations on the reduction of particle size [134].

Table 11: Influence of the Soluplus® stabilizer concentration on the particle size of mirabegron nanoparticles. Data is presented as mean ± SD, n = 5.

(*%w/v*) Soluplus®	**D10 (nm)**	**D50 (nm)**	**D90 (nm)**
0	411.48 ± 43.45	890.26 ± 88.92	2744.10 ± 190.51
0.3	190.14 ± 48.45	253.64 ± 55.68	396.98 ± 79.07
1	41.42 ± 4.10	54.70 ± 5.32	85.12 ± 7.41
3	43.00 ± 1.69	57.18 ± 1.68	91.06 ± 1.62
10	39.68 ± 2.20	51.74 ± 2.17	76.94 ± 1.67

The particles in the 1% Soluplus® containing suspension were imaged with SEM. Their particle size was found to correspond with DLS measurements and no decisive morphology was observed (Fig. 25). Thus, no clear deduction of crystalline solid state could be made, suggesting that particles might have precipitated in an amorphous state. Previous studies using a similar antisolvent ultrasonic precipitation method for the preparation of Cefuroxim axetil nanoparticles also yielded amorphous nanoparticles [135]. Furthermore, Yonashiro et al. argued in a study utilizing antisolvent precipitation from DMSO into an HPMC solution

that a spherical morphology or one similar to the here presented could be an indicator of an amorphous solid state in aqueous suspensions [136].

In an FDC permeation experiment the 1% Soluplus® suspension delivered 5.5 ± 1.6 µg/cm² of MIR across 400 µm thick human abdominal skin in 24 h (Fig. 26). Interestingly, the permeated amount of MIR was drastically increased compared to the 2% solution of MIR in the binary solvent mixture of 5% DMSO and 95% EtOH, despite the reduced drug load and DMSO content, as well as absence of EtOH. This could be due to the increased distribution coefficient from the mostly aqueous suspension, in which dissolved and permeated API is instantly replaced, because of the increased rate of dissolution of nanoparticles [137,138]. Furthermore, the kinetic solubility of nanoparticles was found to increase with decreasing particle size, further suggesting a higher available concentration of dissolved MIR for skin permeation [138,139].

Therefore, formulating MIR in nanoparticle suspension and exploiting its poor solubility in water could be an alternative to the purely organic formulation approaches that rely on greater amounts of DMSO.

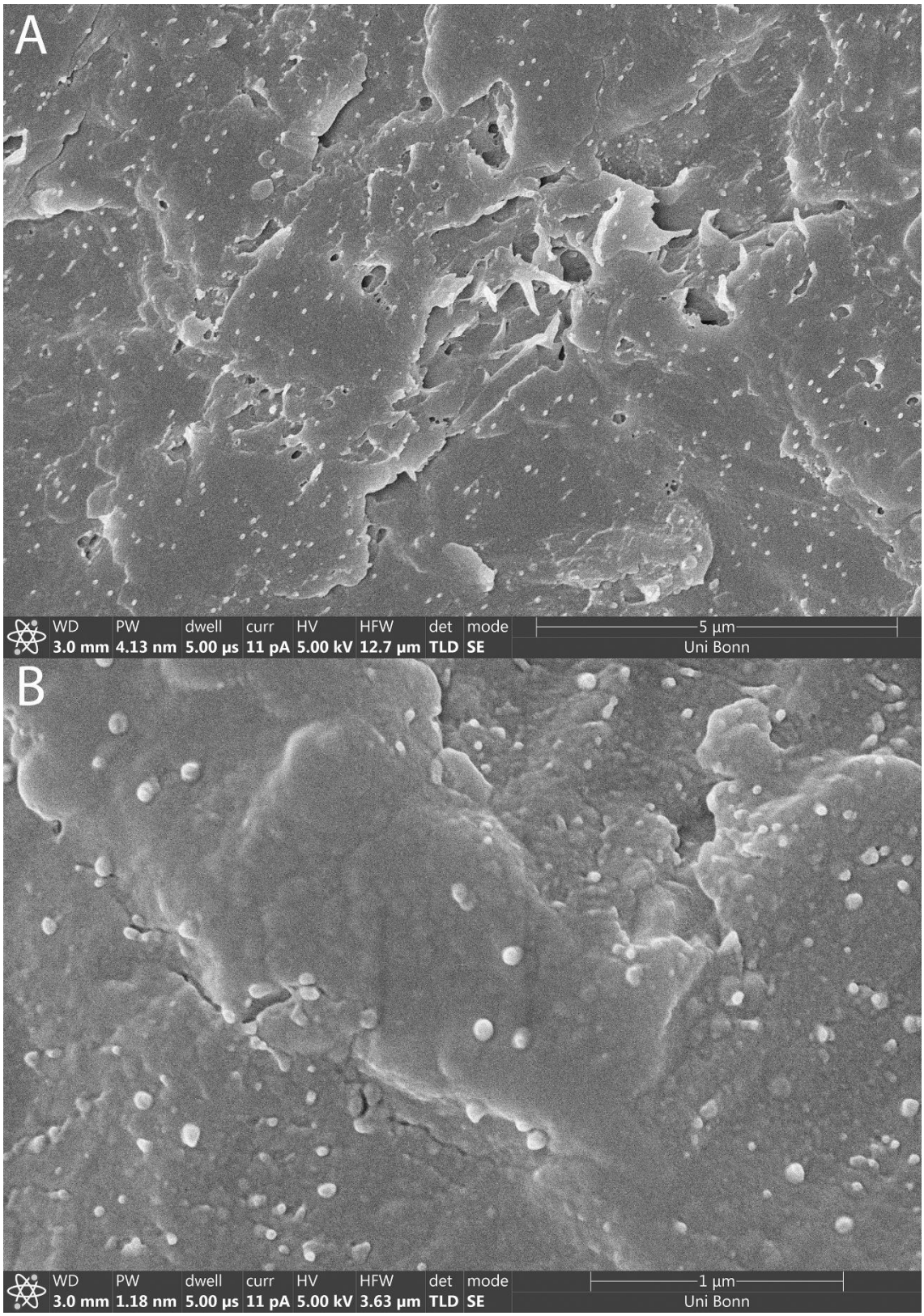

Figure 25: Scanning electron micrographs of a mirabegron nanoparticle suspension containing 0.2% (*w/v*) mirabegron, 0.1% (*w/v*) sodium lauryl sulfate, 1% HPC-SL (*w/v*), and 1% Soluplus® (*w/v*). **(A)** Overview and **(B)** detail image of precipitated polymer matrix. Nanoparticles are visible as brighter structures on the darker polymeric matrix.

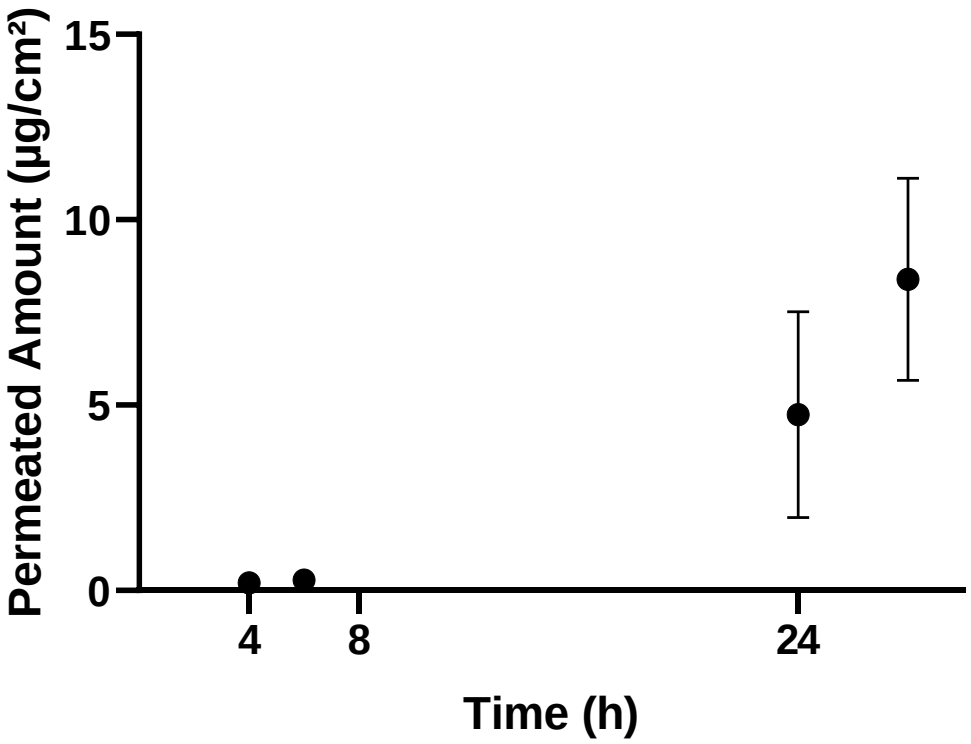

Figure 26: Permeation time profile of mirabegron from a 0.2% (*w/v*) nanoparticle suspension containing 2% (*v/v*) DMSO, 1% (*w/v*) Soluplus, 1% HPC-SL (*w/v*), and 0.1% (*w/v*) SDS. Data is presented as mean ± SD, n = 6.

For some time browning adipose tissue by β3ADR activation has been a hope for improving metabolic diseases and obesity through its functionality to increase energy expenditure by non-shivering thermogenesis [140]. Cypess et al. demonstrated the ability of mirabegron to increase activity of BAT in humans after oral application of 50 mg and 200 mg [55]. However, for high effects on BAT activity a dose of 200 mg of drug was needed. Application of this higher than regulatory approved for dose resulted in disproportionately higher plasma concentrations leading to increased adverse effects on the cardiovascular system e.g. increased heart rate and elevated blood pressure, in several studies [53,55,141]. In addition to activation of BAT, application of MIR was shown to induce browning by expression of BAT typical thermogenesis relevant proteins in human subcutaneous WAT [54]. To circumvent the adverse effects connected to high dose oral treatment, drug targeting to WAT and BAT is needed allowing for a maximum effect in these tissues, while enabling maintenance of a highly tolerable available plasma concentration. Several approaches have been developed and utilized for the efficient delivery of a variety of browning agents. Another chemically similar β3ADR agonist, CL-316243, was shown to lead to WAT

browning in rodent models after infusion [142,143]. A transdermal approach for this compound was taken by Than et al. who described effective browning of rat WAT by microneedle patch delivery, as well as patch delivered implantable micro lances [144,145]. They observed an increase in browning gene marker expression as well as a reduction in adipose tissue mass and total body weight. Another microneedle patch for the same active agent by Xie et al. increased UCP1 protein expression, as well as BAT weight, while decreasing WATi in diet-induced obese mice [146]. Thus, feasibility of WAT browning by transdermal delivery of β3-agonists was shown, however CL-316243 has not been registered with any drug regulatory agencies and extensive trials concerning safety would have to be conducted for market approval, whereas MIR has the advantage of an already known long term risk profile for oral administration [56]. One can assume that risks for dermal application of MIR are similar or even less, since oral administration typically results in higher plasma concentrations and associated adverse reactions compared to transdermal application [147]. Furthermore, despite reports of high tolerability when using the right needle geometry and biocompatible needle material, physical damage to the skin of an area of this size would still pose risk of infection and come with costly production under aseptic conditions or with an appropriate sterilization method [148,149]. In addition, a gel or liquid formulation could easily be applied to any site of the body offering patients an intuitive, reliable, and versatile approach, thus increasing adherence.

While the presented results suggest a superiority of MIR for topical browning by presumed β3ADR activation, different studies have argued that human thermogenesis is independent of the β3ADR or found activation of β1- or β2ADRs to be more important adrenergic pathways, also arguing that induction of browning by MIR is a result of crosstalk at the other βADRs [57–60]. As β2 is the predominant βADR subtype in human adipocytes in contrast to β3 in mice, further research needs to be conducted to clarify the ability of β2- and β3ADR agonists to brown human adipose tissue. such as formoterol that was already shown to increase energy expenditure in humans should be conducted [96]. Since the associated adverse effects mimic those of MIR, topical drug delivery should again be preferred. Apart from adrenergic substances, as activation of BAT and browning is depending on increased cAMP levels as common link, further classes of API could also be studied. For instance, first promising approaches have been conducted by activation of adenosine receptor A2B, inhibition of phosphodiesterase type 5 or delivery of antioxidant resveratrol [150–153].

5.2 Improving Transungual Permeation Study Design by Increased Bovine Hoof Membrane Thickness and Subsequent Infection

This chapter summarizes the results of the following publication:

Kappes, Sebastian[1]; Faber, Thilo[1]; Nelleßen, Lotta[1]; Yesilkaya, Tanju[2]; Bock, Udo[3]; Lamprecht, Alf[1,4]. Improving Transungual Permeation Study Design by Increased Bovine Hoof Membrane Thickness and Subsequent Infection. Pharmaceutics 2021, 13, 2098. https://doi.org/10.3390/ pharmaceutics13122098

[1] Department of Pharmaceutics, Institute of Pharmacy, University of Bonn, Gerhard-Domagk-Str. 3, 53121 Bonn, Germany

[2] Bayer Vital GmbH, 51373 Leverkusen, Germany

[3] Bock Project Management, 54456 Tawern, Germany

[4] PEPITE EA4267, University of Burgundy/Franche-Comté, 25000 Besançon, France

Summary

Almost five percent of the North American and European population is affected by fungal nail infection [154]. These infections are mainly caused by the dermatophyte *Trichophyton rubrum* and result in brittleness, discoloration, and deformation of the nail plate and subsequently can impact psychological well-being or, if left untreated, spread to adjacent tissues and cause pain and a general reduction in patients' quality of life [86,155]. Although highly effective antifungal actives are available, treatment is often insufficient, due to risk of severe adverse effects upon oral treatment, and topical application requires meticulous patient adherence often over months [156]. This is due to the dense keratin matrix of the nail plate, which can be considered hydrophilic and thus limits the permeation of the typically highly lipophilic antifungal agents through this barrier [62,66]. To develop formulations of these APIs that can effectively deliver the drug into the nail plate, predictive *in-vitro* test systems are needed. For this purpose, membranes composed of bovine hoof (Bovine Hoof Sheets, BHS) have been established as surrogates for the human nail in Franz Diffusion Cell permeation experiments [72,75]. However, ungual permeation experiments mostly relied on 100 to 200 µm thick BHS, when human nails usually are between 250 and 600 µm thick [157]. Furthermore, the structure of nails to be treated could often have been altered by infection [86]. Thus, the BHS' structure was investigated by (focused ion beam) scanning electron microscopy and X-ray microtomography. It was discovered that the membranes

already contained porous structures in the non-infected state that are naturally incorporated in the bovine hoof [158]. Infection of the membranes resulted in a dense growth of fungi over the entirety of the membrane surface and a cross-section fracture revealed fungal growth inside the matrix as well. To test the influence of membrane thickness on the resolution of permeation profiles from different dosage forms the bifonazole containing commercial products Canesten® Extra Creme (CRE) and Canesten® Extra Salbe (SAL), as well as Canesten® Extra Salbe without the contained ungual penetration enhancer urea (SAL w/o) were taken as semisolid, immediate release references [83]. Furthermore, an ethanolic solution (SOL), a nail lacquer made of Eudragit® RL (LAC), and a patch with DuroTAK® 2054 as matrix (PAT), each with equal drug load to the commercial products, were prepared and, if applicable, solid state was analyzed by polarized light microscopy, differential scanning calorimetry and X-ray diffraction to ensure the drug was dissolved in the respective matrix. Upon normalizing fluxes obtained from FDC permeation experiments over the course of 6 d to a thickness of 100 µm significant differences for each tested immediate release formulation were found between the 100 and 400 µm setup, while PAT and LAC did not differ significantly. Furthermore, while fluxes from CRE, SAL, and SAL w/o were similar in the 100 µm setup, increasing the thickness to 400 µm resulted in significantly higher flux from SAL compared to CRE and SAL w/o. The observed differences were connected to the porous structure of the membrane, whose pores were more likely to end inside the membrane in the 400 µm thick ones instead of reaching throughout and resulting in more shunt routes for transport in the 100 µm BHS. Because of these shunt routes, flux from extended-release dosage forms whose release of API was the rate limiting process were still differentiable in the 100 µm setup, while resolution of flux from instant release formulations profited from the more retentive 400 µm BHS. Furthermore, the increased flux from SAL over SAL w/o could be explained by the high content of urea in SAL that acted as a penetration enhancer.

FDC permeation experiments with SAL and CRE on infected membranes yielded similar results for infected and non-infected BHS for both dosage forms. However, the flux from CRE showed an increasing trend, which could indicate a higher permeability of infected 400 µm membranes compared to the healthy ones, that was not observable with SAL due to the strong penetration enhancement in the healthy setup. Interestingly, application of SAL resulted in ablation of the top layer of infected membrane in the daily exchange of formulation, as indicated by a loss of color on the BHS surface. This could also be attributed

to the high amount of urea in SAL which acted as a keratolytic agent and the removal of SAL during the daily formulation exchange with a plastic scraper [159].

Concluding, a step towards a more physiological, and rational experimental setup in ungual permeation studies was taken by highlighting the applicability of BHS of differing thickness and infection status. However, further studies should be conducted to establish standards for the *in-vitro* testing of dosage forms and therapeutic regimens.

In this study I took part in the conceptualization of the experiments and in developing the methodology. The experiments were performed or supervised by me. I curated the data and wrote the manuscript.

6 Conclusion and Outlook

In this work the goal of advancing the development of topical dosage forms by identifying formulation approaches of β-adrenergic agents for topical administration to treat the subcutaneous adipose tissue, and by improving FDC setups in ungual permeation studies was successfully achieved.

From the class of β2ADR agonists, CLB was found to be deliverable from solvent systems of various binary mixtures and even in the form of a patch *in-vitro*, whereas FF proved to be dependent on the inclusion of polar aprotic solvents. In contrast to these compounds, SS was formulable in highly aqueous solvent mixtures with high possible drug load. Application of a CLB and SS gel on mice *in-vivo* resulted in histologic changes in WATi for both agonists and an upregulation of browning gene markers in the case of CLB, demonstrating delivery to the target tissue and a certain efficacy of these gels. However, the observed effects were not as pronounced as could be suspected from the *in-vitro* permeation experiments.

Vastly superior results in the murine model were obtained by application of MIR gels, which increased the expression of various browning markers, most notably UCP1, and led to a pronounced change in adipose tissue morphology toward a brown/beige phenotype. These results were obtained by formulating MIR in completely gels based completely on organic solvents, in which the permeated amount of MIR was strongly dependent on the contained amount of DMSO, which increased the amount permeated and decreased the lag time with increasing ratio of DMSO. Despite the highest permeation *in-vitro*, the application of a gel based on pure DMSO was inferior in inducing gene expression of browning markers compared to gels containing less DMSO, highlighting the importance of identifying formulations with tolerable amounts of penetration enhancers and appropriate doses of delivered API. Nevertheless, the gel based on pure DMSO was shown to increase browning markers in human adipose tissue in an *ex-vivo* setting, proving the general feasibility of topical browning in humans.

Taken together, the presented results suggest superiority of MIR for browning of WAT over both CLB and SS. Nonetheless, recent studies on the importance of the β2ADR for the activation of BAT in humans insinuate a limited response of murine WATi to delivered CLB and SS due to the different expression of βADRs in humans and rodents. Moreover, the physicochemical properties of the formulations change rapidly after application *in-vivo* due to evaporation and uptake of each respective compound, which might not have been

mimicked completely in FDC experiments. Thus, the delivery of CLB and SS to the adipose tissue could have been overestimated from the *in-vitro* experiments. However, the inclusion of DMSO in tolerable doses as a potent permeation enhancer of low volatility into the formulations of β2ADR agonists could further improve their delivery to the adipose tissue *in-vivo* similarly to MIR, which could also be exploited for FF in the future. Nanoparticle formulations could then be used to potentially reduce the amount of DMSO, if needed in these cases.

Overall, the herein identified formulations of both β2- and β3ADR agonists present foundations that could be tested in humans *in-vivo* to establish if and which formulations are more efficacious in browning human subcutaneous WAT. Alternatively, they could enable development of more advanced formulation iterations in case of ultimate clarification of the determining βADR in browning of WAT in humans. The exploitation of topical browning agent application and the therapy of metabolic disorders by adipose tissue browning are still in their infancy and this work demonstrates a first feasibility utilizing βADR agonists. Complementary to these results, further APIs of this class or even compounds with completely different pharmacological background could be tested for their applicability via the skin.

The results obtained in the transungual studies highlighted the necessity of choosing an appropriate membrane for formulation development of topical medicines for ungual application. While BHS of 100 µm thickness allowed adequate assessment of permeation characteristics in an acceptable time frame in the case of dosage forms that were themselves rate-limiting, immediate release dosage forms benefited from the higher barrier function of 400 µm BHS, which allowed better discrimination between them. In addition, infection of membranes increased permeability and further allowed exploring effects of the formulation on ablation of the infected BHS substance. The obtained results will allow a more rational decision for membranes of different thickness depending on the topical dosage form to be tested in *in-vitro* permeation experiments. Furthermore, the effects of other nail conditions could be studied, to obtain even more predictive systems for each respective condition.

7 References

1. Zhong H, Chan G, Hu Y, Hu H, Ouyang D. A Comprehensive Map of FDA-Approved Pharmaceutical Products. Pharmaceutics. 2018;10:263.

2. Hadgraft J. Skin deep. Eur J Pharm Biopharm. 2004;58:291–9.

3. Abd E, Yousef SA, Pastore MN, Telaprolu K, Mohammed YH, Namjoshi S, et al. Skin models for the testing of transdermal drugs. Clin Pharmacol. 2016;8:163–76.

4. Iwai I, Han H, Hollander L den, Svensson S, Öfverstedt L-G, Anwar J, et al. The Human Skin Barrier Is Organized as Stacked Bilayers of Fully Extended Ceramides with Cholesterol Molecules Associated with the Ceramide Sphingoid Moiety. Journal of Investigative Dermatology. 2012;132:2215–25.

5. Boncheva M. The physical chemistry of the stratum corneum lipids. International Journal of Cosmetic Science. 2014;36:505–15.

6. Council of Europe. Flüssige Zubereitungen zur kutanen Anwendung. European Pharmacopoeia. 10.7. Strasbourg, France; 2023. p. 9587 ff.

7. Council of Europe. Halbfeste Zubereitungen zur kutanen Anwendung. European Pharmacopoeia. 10.5. Strasbourg, France; 2022. p. 8305 ff.

8. Council of Europe. Pflaster. European Pharmacopoeia. 10.5. 2022. p. 8314 ff.

9. Liu C, Hui M, Quan P, Fang L. Drug in adhesive patch of palonosetron: Effect of pressure sensitive adhesive on drug skin permeation and in vitro-in vivo correlation. Int J Pharm. 2016;511:1088–97.

10. Yasunori M, Takemasa K, Kenji S. Diffusion of drugs in acrylic-type pressure-sensitive adhesive matrix. II. Influence of interaction. Journal of Controlled Release. 1992;18:113–21.

11. Lane ME. Skin penetration enhancers. International Journal of Pharmaceutics. 2013;447:12–21.

12. Jepps OG, Dancik Y, Anissimov YG, Roberts MS. Modeling the human skin barrier — Towards a better understanding of dermal absorption. Advanced Drug Delivery Reviews. 2013;65:152–68.

13. Vidlářová L, Romero GB, Hanuš J, Štěpánek F, Müller RH. Nanocrystals for dermal penetration enhancement – Effect of concentration and underlying mechanisms using curcumin as model. European Journal of Pharmaceutics and Biopharmaceutics. 2016;104:216–25.

14. Pelikh O, Eckert RW, Pinnapireddy SR, Keck CM. Hair follicle targeting with curcumin nanocrystals: Influence of the formulation properties on the penetration efficacy. Journal of Controlled Release. 2021;329:598–613.

15. Romero GB, Chen R, Keck CM, Müller RH. Industrial concentrates of dermal hesperidin smartCrystals® – production, characterization & long-term stability. International Journal of Pharmaceutics. 2015;482:54–60.

16. Chen L, Han L, Lian G. Recent advances in predicting skin permeability of hydrophilic solutes. Advanced Drug Delivery Reviews. 2013;65:295–305.

17. Andrews SN, Jeong E, Prausnitz MR. Transdermal Delivery of Molecules is Limited by Full Epidermis, Not Just Stratum Corneum. Pharm Res. 2013;30:1099–109.

18. Warner RR, Myers MC, Taylor DA. Electron Probe Analysis of Human Skin: Determination of the Water Concentration Profile. Journal of Investigative Dermatology. 1988;90:218–24.

19. Caspers PJ, Lucassen GW, Puppels GJ. Combined In Vivo Confocal Raman Spectroscopy and Confocal Microscopy of Human Skin. Biophysical Journal. 2003;85:572–80.

20. Yamaguchi K, Mitsui T, Aso Y, Sugibayashi K. Structure–Permeability Relationship Analysis of the Permeation Barrier Properties of the Stratum Corneum and Viable Epidermis/Dermis of Rat Skin. Journal of Pharmaceutical Sciences. 2008;97:4391–403.

21. Roberts MS, Cheruvu HS, Mangion SE, Alinaghi A, Benson HAE, Mohammed Y, et al. Topical drug delivery: History, percutaneous absorption, and product development. Advanced Drug Delivery Reviews. 2021;177:113929.

22. Magnusson BM, Cross SE, Winckle G, Roberts MS. Percutaneous Absorption of Steroids: Determination of in vitro Permeability and Tissue Reservoir Characteristics in Human Skin Layers. Skin Pharmacology and Physiology. 2006;19:336–42.

23. Brown MB, Martin GP, Jones SA, Akomeah FK. Dermal and Transdermal Drug Delivery Systems: Current and Future Prospects. Drug Delivery. 2006;13:175–87.

24. Pershing LK, Lambert LD, Knutson K. Mechanism of Ethanol-Enhanced Estradiol Permeation Across Human Skin in Vivo. Pharm Res. 1990;7:170–5.

25. Moser K, Kriwet K, Kalia YN, Guy RH. Enhanced skin permeation of a lipophilic drug using supersaturated formulations. Journal of Controlled Release. 2001;73:245–53.

26. Megrab NA, Williams AC, Barry BW. Oestradiol permeation across human skin, silastic and snake skin membranes: The effects of ethanol/water co-solvent systems. International Journal of Pharmaceutics. 1995;116:101–12.

27. Osborne DW, Musakhanian J. Skin Penetration and Permeation Properties of Transcutol®—Neat or Diluted Mixtures. AAPS PharmSciTech. 2018;19:3512–33.

28. Ursin C, Hansen CM, Van Dyk JW, Jensen PO, Christensen IJ, Ebbehoej J. Permeability of Commercial Solvents Through Living Human Skin. American Industrial Hygiene Association Journal. 1995;56:651–60.

29. Anigbogu ANC, Williams AC, Barry BW, Edwards HGM. Fourier transform raman spectroscopy of interactions between the penetration enhancer dimethyl sulfoxide and human stratum corneum. International Journal of Pharmaceutics. 1995;125:265–82.

30. Gesta S, Tseng Y-H, Kahn CR. Developmental Origin of Fat: Tracking Obesity to Its Source. Cell. 2007;131:242–56.

31. van Marken Lichtenbelt WD, Vanhommerig JW, Smulders NM, Drossaerts JMAFL, Kemerink GJ, Bouvy ND, et al. Cold-Activated Brown Adipose Tissue in Healthy Men. N Engl J Med. 2009;360:1500–8.

32. Zhang F, Hao G, Shao M, Nham K, An Y, Wang Q, et al. An Adipose Tissue Atlas: An Image-Guided Identification of Human-like BAT and Beige Depots in Rodents. Cell Metabolism. 2018;27:252-262.e3.

33. Cannon B, Nedergaard J. Brown adipose tissue: function and physiological significance. Physiol Rev. 2004;84:277–359.

34. Fedorenko A, Lishko PV, Kirichok Y. Mechanism of Fatty-Acid-Dependent UCP1 Uncoupling in Brown Fat Mitochondria. Cell. 2012;151:400–13.

35. Abreu-Vieira G, Fischer AW, Mattsson C, de Jong JMA, Shabalina IG, Rydén M, et al. Cidea improves the metabolic profile through expansion of adipose tissue. Nat Commun. 2015;6:7433.

36. Puri V, Ranjit S, Konda S, Nicoloro SMC, Straubhaar J, Chawla A, et al. Cidea is associated with lipid droplets and insulin sensitivity in humans. Proc Natl Acad Sci U S A. 2008;105:7833–8.

37. Lin J, Handschin C, Spiegelman BM. Metabolic control through the PGC-1 family of transcription coactivators. Cell Metabolism. 2005;1:361–70.

38. Ahmadian M, Suh JM, Hah N, Liddle C, Atkins AR, Downes M, et al. PPARγ signaling and metabolism: the good, the bad and the future. Nat Med. 2013;19:557–66.

39. Jesus LA de, Carvalho SD, Ribeiro MO, Schneider M, Kim S-W, Harney JW, et al. The type 2 iodothyronine deiodinase is essential for adaptive thermogenesis in brown adipose tissue. J Clin Invest. 2001;108:1379–85.

40. Guilherme A, Yenilmez B, Bedard AH, Henriques F, Liu D, Lee A, et al. Control of Adipocyte Thermogenesis and Lipogenesis through β3-Adrenergic and Thyroid Hormone Signal Integration. Cell Reports. 2020;31:107598.

41. Powell-Wiley TM, Poirier P, Burke LE, Després J-P, Gordon-Larsen P, Lavie CJ, et al. Obesity and Cardiovascular Disease: A Scientific Statement From the American Heart Association. Circulation [Internet]. 2021 [cited 2022 Feb 17];143. Available from: https://www.ahajournals.org/doi/10.1161/CIR.0000000000000973

42. Eurostat. Body mass index (BMI) by sex, age and educational attainment level [Internet]. 2022 [cited 2022 Feb 28]. Available from: https://appsso.eurostat.ec.europa.eu/nui/show.do?dataset=hlth_ehis_bm1e&lang=en

43. Hales CM. Prevalence of Obesity and Severe Obesity Among Adults: United States, 2017–2018. 2020;8.

44. OECD, European Union. Obesity among adults [Internet]. Paris: OECD; 2020 Nov. Available from: https://www.oecd-ilibrary.org/social-issues-migration-health/health-at-a-glance-europe-2020_8cdeadfa-en

45. Bessesen DH, Gaal LFV. Progress and challenges in anti-obesity pharmacotherapy. The Lancet Diabetes & Endocrinology. 2018;6:237–48.

46. Becher T, Palanisamy S, Kramer DJ, Eljalby M, Marx SJ, Wibmer AG, et al. Brown adipose tissue is associated with cardiometabolic health. Nat Med. 2021;27:58–65.

47. Cinti S. Transdifferentiation properties of adipocytes in the adipose organ. American Journal of Physiology-Endocrinology and Metabolism. 2009;297:E977–86.

48. Bartesaghi S, Hallen S, Huang L, Svensson P-A, Momo RA, Wallin S, et al. Thermogenic Activity of UCP1 in Human White Fat-Derived Beige Adipocytes. Molecular Endocrinology. 2015;29:130–9.

49. Cero C, Lea HJ, Zhu KY, Shamsi F, Tseng Y-H, Cypess AM. β3-Adrenergic receptors regulate human brown/beige adipocyte lipolysis and thermogenesis. JCI Insight. 2021;6:139160.

50. Kern PA, Finlin BS, Zhu B, Rasouli N, McGehee RE, Westgate PM, et al. The Effects of Temperature and Seasons on Subcutaneous White Adipose Tissue in Humans: Evidence for Thermogenic Gene Induction. J Clin Endocrinol Metab. 2014;99:E2772–9.

51. Pfeifer A, Hoffmann LS. Brown, beige, and white: the new color code of fat and its pharmacological implications. Annu Rev Pharmacol Toxicol. 2015;55:207–27.

52. de Souza CJ, Hirshman MF, Horton ES. CL-316,243, a beta3-specific adrenoceptor agonist, enhances insulin-stimulated glucose disposal in nonobese rats. Diabetes. 1997;46:1257–63.

53. Cypess AM, Weiner LS, Roberts-Toler C, Franquet Elía E, Kessler SH, Kahn PA, et al. Activation of human brown adipose tissue by a β3-adrenergic receptor agonist. Cell Metab. 2015;21:33–8.

54. Finlin BS, Memetimin H, Confides AL, Kasza I, Zhu B, Vekaria HJ, et al. Human adipose beiging in response to cold and mirabegron. JCI Insight [Internet]. 2018 [cited 2021 Jun 18];3. Available from: https://insight.jci.org/articles/view/121510

55. Baskin AS, Linderman JD, Brychta RJ, McGehee S, Anflick-Chames E, Cero C, et al. Regulation of Human Adipose Tissue Activation, Gallbladder Size, and Bile Acid Metabolism by a β3-Adrenergic Receptor Agonist. Diabetes. 2018;67:2113–25.

56. Kato D, Tabuchi H, Uno S. Three-year safety, efficacy and persistence data following the daily use of mirabegron for overactive bladder in the clinical setting: A Japanese post-marketing surveillance study. Low Urin Tract Symptoms. 2019;11:O152–61.

57. de Jong JMA, Wouters RTF, Boulet N, Cannon B, Nedergaard J, Petrovic N. The β3-adrenergic receptor is dispensable for browning of adipose tissues. American Journal of Physiology-Endocrinology and Metabolism. 2017;312:E508–18.

58. Blondin DP, Nielsen S, Kuipers EN, Severinsen MC, Jensen VH, Miard S, et al. Human Brown Adipocyte Thermogenesis Is Driven by β2-AR Stimulation. Cell Metabolism. 2020;32:287-300.e7.

59. Riis-Vestergaard MJ, Richelsen B, Bruun JM, Li W, Hansen JB, Pedersen SB. Beta-1 and Not Beta-3 Adrenergic Receptors May Be the Primary Regulator of Human Brown Adipocyte Metabolism. The Journal of Clinical Endocrinology & Metabolism. 2020;105:e994–1005.

60. Mattsson CL, Csikasz RI, Chernogubova E, Yamamoto DL, Hogberg HT, Amri E-Z, et al. β1-Adrenergic receptors increase UCP1 in human MADS brown adipocytes and rescue cold-acclimated β3-adrenergic receptor-knockout mice via nonshivering thermogenesis. American Journal of Physiology-Endocrinology and Metabolism. 2011;301:E1108–18.

61. Baswan S, Kasting GB, Li SK, Wickett R, Adams B, Eurich S, et al. Understanding the formidable nail barrier: A review of the nail microstructure, composition and diseases. Mycoses. 2017;60:284–95.

62. Walters KA, Abdalghafor HM, Lane ME. The human nail – Barrier characterisation and permeation enhancement. International Journal of Pharmaceutics. 2012;435:10–21.

63. Bragulla HH, Homberger DG. Structure and functions of keratin proteins in simple, stratified, keratinized and cornified epithelia. J Anat. 2009;214:516–59.

64. Kitahara T, Ogawa H. The extraction and characterization of human nail keratin. Journal of Dermatological Science. 1991;2:402–6.

65. Lynch MH, O'Guin WM, Hardy C, Mak L, Sun TT. Acidic and basic hair/nail ("hard") keratins: their colocalization in upper cortical and cuticle cells of the human hair follicle and their relationship to "soft" keratins. Journal of Cell Biology. 1986;103:2593–606.

66. Kobayashi Y, Miyamoto M, Sugibayashi K, Morimoto Y. Drug Permeation through the Three Layers of the Human Nail Plate. Journal of Pharmacy and Pharmacology. 1999;51:271–8.

67. Farren L, Shayler S, Ennos AR. The fracture properties and mechanical design of human fingernails. Journal of Experimental Biology. 2004;207:735–41.

68. Walters KA, Flynn GL. Permeability characteristics of the human nail plate. International Journal of Cosmetic Science. 1983;5:231–46.

69. Farran L, Ennos AR, Eichhorn SJ. The effect of humidity on the fracture properties of human fingernails. Journal of Experimental Biology. 2008;211:3677–81.

70. Piraccini BM, Alessandrini A. Onychomycosis: A Review. Journal of Fungi. 2015;1:30–43.

71. Vikas A, Rashmin P, Mrunali P, Chavan RB, Kaushik T. Mechanistic Insights of Formulation Approaches for the Treatment of Nail Infection: Conventional and Novel Drug Delivery Approaches. AAPS PharmSciTech. 2020;21:67.

72. Mertin D, Lippold BC. In-vitro permeability of the human nail and of a keratin membrane from bovine hooves: prediction of the penetration rate of antimycotics through the nail plate and their efficacy. J Pharm Pharmacol. 1997;49:866–72.

73. Kobayashi Y, Komatsu T, Sumi M, Numajiri S, Miyamoto M, Kobayashi D, et al. In vitro permeation of several drugs through the human nail plate: relationship between physicochemical properties and nail permeability of drugs. European Journal of Pharmaceutical Sciences. 2004;21:471–7.

74. Elsayed MMA. Development of topical therapeutics for management of onychomycosis and other nail disorders: A pharmaceutical perspective. Journal of Controlled Release. 2015;199:132–44.

75. Bonetti M, Bracchi M, Musitelli G, Perugini P. Production and characterization of bovine hoof membranes as standardized in vitro model for nail studies. International Journal of Pharmaceutics. 2021;120409.

76. Temporiti MEE, Guerini M, Baiguera RM, Buratti S, Desiderio A, Goppa L, et al. Efficacy of Bovine Nail Membranes as In Vitro Model for Onychomycosis Infected by Trichophyton Species. Journal of Fungi. 2022;8:1133.

77. Miron D, Cornelio R, Troleis J, Mariath J, Zimmer AR, Mayorga P, et al. Influence of penetration enhancers and molecular weight in antifungals permeation through bovine hoof

membranes and prediction of efficacy in human nails. European Journal of Pharmaceutical Sciences. 2014;51:20–5.

78. Kobayashi Y, Miyamoto M, Sugibayashi K, Morimoto Y. Enhancing effect of N-acetyl-l-cysteine or 2-mercaptoethanol on the in vitro permeation of 5-fluorouracil or tolnaftate through the human nail plate. Chem Pharm Bull (Tokyo). 1998;46:1797–802.

79. Patel MM, Vora ZM. Formulation development and optimization of transungual drug delivery system of terbinafine hydrochloride for the treatment of onychomycosis. Drug Deliv and Transl Res. 2016;6:263–75.

80. Khengar RH, Jones SA, Turner RB, Forbes B, Brown MB. Nail Swelling as a Pre-formulation Screen for the Selection and Optimisation of Ungual Penetration Enhancers. Pharm Res. 2007;24:2207–12.

81. Mohorčič M, Torkar A, Friedrich J, Kristl J, Murdan S. An investigation into keratinolytic enzymes to enhance ungual drug delivery. International Journal of Pharmaceutics. 2007;332:196–201.

82. Tietz H-J, Hay R, Querner S, Delcker A, Kurka P, Merk HF. Efficacy of 4 weeks topical bifonazole treatment for onychomycosis after nail ablation with 40% urea: a double-blind, randomized, placebo-controlled multicenter study. Mycoses. 2013;56:414–21.

83. Yang F, Yu X, Shao W, Guo P, Cao S, Wang M, et al. Co-delivery of terbinafine hydrochloride and urea with an in situ film-forming system for nail targeting treatment. International Journal of Pharmaceutics. 2020;585:119497.

84. Lee DK, Lipner SR. Optimal diagnosis and management of common nail disorders. Annals of Medicine. 2022;54:694–712.

85. Lipner SR, Scher RK. Onychomycosis: Clinical overview and diagnosis. Journal of the American Academy of Dermatology. 2019;80:835–51.

86. Stewart CR, Algu L, Kamran R, Leveille CF, Abid K, Rae C, et al. Effect of onychomycosis and treatment on patient-reported quality-of-life outcomes: A systematic review. Journal of the American Academy of Dermatology [Internet]. 2020 [cited 2021 May 19]; Available from: https://www.sciencedirect.com/science/article/pii/S0190962220310203

87. Wishart DS, Feunang YD, Guo AC, Lo EJ, Marcu A, Grant JR, et al. DrugBank 5.0: a major update to the DrugBank database for 2018. Nucleic Acids Research. 2018;46:D1074–82.

88. OECD. Test No. 428: Skin Absorption: In Vitro Method [Internet]. Paris: Organisation for Economic Co-operation and Development; 2004 [cited 2022 Nov 8]. Available from: https://www.oecd-ilibrary.org/environment/test-no-428-skin-absorption-in-vitro-method_9789264071087-en

89. OECD. GUIDANCE NOTES ON DERMAL ABSORPTION STUDIES Series on Testing and Assessment No. 156 Second Edition [Internet]. Organisation for Economic Co-operation and Development; 2011. Available from: https://www.oecd.org/officialdocuments/publicdisplaydocumentpdf/?cote=ENV-JM-MONO(2011)36%20&doclanguage=en

90. Livak KJ, Schmittgen TD. Analysis of relative gene expression data using real-time quantitative PCR and the 2(-Delta Delta C(T)) Method. Methods. 2001;25:402–8.

91. Schneider CA, Rasband WS, Eliceiri KW. NIH Image to ImageJ: 25 years of image analysis. Nat Methods. 2012;9:671–5.

92. Straat ME, Hoekx CA, van Velden FHP, Pereira Arias-Bouda LM, Dumont L, Blondin DP, et al. Stimulation of the beta-2-adrenergic receptor with salbutamol activates human brown adipose tissue. Cell Reports Medicine. 2023;4:100942.

93. Baker JG. The selectivity of β-adrenoceptor agonists at human β1-, β2- and β3-adrenoceptors. British Journal of Pharmacology. 2010;160:1048–61.

94. Hostrup M, Onslev J. The beta2-adrenergic receptor – a re-emerging target to combat obesity and induce leanness? The Journal of Physiology. 2022;600:1209–27.

95. Jessen S, Solheim SA, Jacobson GA, Eibye K, Bangsbo J, Nordsborg NB, et al. Beta2-adrenergic agonist clenbuterol increases energy expenditure and fat oxidation, and induces mTOR phosphorylation in skeletal muscle of young healthy men. Drug Testing and Analysis. 2020;12:610–8.

96. Lee P, Day RO, Greenfield JR, Ho KKY. Formoterol, a highly β2-selective agonist, increases energy expenditure and fat utilisation in men. Int J Obes. 2013;37:593–7.

97. Ohyama K, Nogusa Y, Shinoda K, Suzuki K, Bannai M, Kajimura S. A Synergistic Antiobesity Effect by a Combination of Capsinoids and Cold Temperature Through Promoting Beige Adipocyte Biogenesis. Diabetes. 2016;65:1410–23.

98. Kakubari I, Nakamura N, Takayasu T, Yamauchi H, Takayama S, Takayama K. Effects of Solvents on Skin Permeation of Formoterol Fumarate. Biological and Pharmaceutical Bulletin. 2006;29:146–9.

99. Kakubari I, Shinkai N, Kawakami J, Uruno A, Takayasu T, Yamauchi H, et al. Formulation and Evaluation of Ethylene–Vinyl Acetate Copolymer Matrix Patches Containing Formoterol Fumarate. Biological and Pharmaceutical Bulletin. 2006;29:513–6.

100. Kakubari I, Sasaki H, Takayasu T, Yamauchi H, Takayama S, Takayama K. Effects of Ethylcellulose and 2-Octyldodecanol Additives on Skin Permeation and Irritation with Ethylene–Vinyl Acetate Copolymer Matrix Patches Containing Formoterol Fumarate. Biological and Pharmaceutical Bulletin. 2006;29:1717–22.

101. EFSA Panel on Food Additives and Flavourings (FAF), Younes M, Aquilina G, Castle L, Engel K-H, Fowler P, et al. Scientific opinion on flavouring group evaluation 414 (FGE.414): 2-hydroxy-4-methoxybenzaldehyde. EFSA Journal. 2021;19:e06883.

102. van Beek SMM, Kalinovich A, Schaart G, Bengtsson T, Hoeks J. Prolonged β2-adrenergic agonist treatment improves glucose homeostasis in diet-induced obese UCP1−/− mice. American Journal of Physiology-Endocrinology and Metabolism. 2021;320:E619–28.

103. Fachinformation - Spasmo-Mucosolvan® Tabletten [Internet]. 2022 [cited 2023 May 11]. Available from: https://mein.sanofi.de/produkte/spasmo-mucosolvan/downloads?id=/resources/SPC/0900972f803324ca/data&pdfName=0900972f803324ca

104. Barry AR, Graham MM. Case report and review of clenbuterol cardiac toxicity. Journal of Cardiology Cases. 2013;8:131–3.

105. Kim H-K, Della-Fera MA, Hausman DB, Baile CA. Effect of clenbuterol on apoptosis, adipogenesis, and lipolysis in adipocytes. J Physiol Biochem. 2010;66:197–203.

106. Subedi RK, Ryoo J-P, Moon C, Chun M-K, Choi H-K. Formulation and in vitro evaluation of transdermal drug delivery system for donepezil. Journal of Pharmaceutical Investigation. 2012;42:1–7.

107. Kim J-H, Cho Y-J, Choi H-K. Effect of vehicles and pressure sensitive adhesives on the permeation of tacrine across hairless mouse skin. International Journal of Pharmaceutics. 2000;196:105–13.

108. Göpferich A, Lee G. Determining the solubility and crystal form of clenbuterol in thin films of eudragit NE30D. Drug Development and Industrial Pharmacy. 1992;18:319–31.

109. Göpferich A, Lee G. Measurement of drug diffusivity in stratum corneum membranes and a polyacrylate matrix. International Journal of Pharmaceutics. 1991;71:245–53.

110. Göpferich A, Lee G. An improved diffusion/compartmental model for transdermal drug delivery from a matrix-type device. International Journal of Pharmaceutics. 1991;71:237–43.

111. El-Gendy NA, Sabry NA, El-Attar M, Omar E, Mahmoud M. Transdermal delivery of salbutamol sulphate: Formulation and evaluation. Pharmaceutical Development and Technology. 2009;14:216–25.

112. Murthy SN, Hiremath SR. Clinical pharmacokinetic and pharmacodynamic evaluation of transdermal drug delivery systems of salbutamol sulfate. International Journal of Pharmaceutics. 2004;287:47–53.

113. Murthy SN, Rani S, Hiremath R. Formulation and Evaluation of Controlled-Release Transdermal Patches of Theophylline–Salbutamol Sulfate. Drug Development and Industrial Pharmacy. 2001;27:1057–62.

114. Lee SM. Effect of skin from different species and comparisons of penetration enhancers on transdermal delivery of Salbutamol hemisulfate. Rheinische Friedrich-Wilhems-Universität Bonn; 2023.

115. Ali HSM, York P, Blagden N, Khoubnasabjafari M, Acree WE, Jouyban A. Solubility of salbutamol and salbutamol sulphate in ethanol+water mixtures at 25°C. Journal of Molecular Liquids. 2012;173:62–5.

116. Williams AC, Barry BW. Penetration enhancers. Advanced Drug Delivery Reviews. 2012;64:128–37.

117. Cheng C-Y, Song J, Pas J, Meijer LHH, Han S. DMSO Induces Dehydration near Lipid Membrane Surfaces. Biophysical Journal. 2015;109:330–9.

118. Lundborg M, Wennberg CL, Narangifard A, Lindahl E, Norlén L. Predicting drug permeability through skin using molecular dynamics simulation. Journal of Controlled Release. 2018;283:269–79.

119. Otterbach A, Lamprecht A. Enhanced Skin Permeation of Estradiol by Dimethyl Sulfoxide Containing Transdermal Patches. Pharmaceutics. 2021;13:320.

120. Baer PA, Thomas LM, Shainhouse Z. Treatment of osteoarthritis of the knee with a topical diclofenac solution: a randomised controlled, 6-week trial [ISRCTN53366886]. BMC Musculoskeletal Disorders. 2005;6:44.

121. Simon LS, Grierson LM, Naseer Z, Bookman AAM, Shainhouse ZJ. Efficacy and safety of topical diclofenac containing dimethyl sulfoxide (DMSO) compared with those of topical placebo, DMSO vehicle and oral diclofenac for knee osteoarthritis. PAIN. 2009;143:238–45.

122. Valentine JM, Ahmadian M, Keinan O, Abu-Odeh M, Zhao P, Zhou X, et al. **β**3-Adrenergic receptor downregulation leads to adipocyte catecholamine resistance in obesity. J Clin Invest [Internet]. 2022 [cited 2023 Jan 10];132. Available from: https://www.jci.org/articles/view/153357

123. Okeke K, Angers S, Bouvier M, Michel MC. Agonist-induced desensitisation of β3-adrenoceptors: Where, when, and how? British Journal of Pharmacology. 2019;176:2539–58.

124. Atgié C, Faintrenie G, Carpéné C, Bukowiecki LJ, Géloën A. Effects of Chronic Treatment with Noradrenaline or a Specific β3-Adrenergic Agonist, CL 316 243, on Energy Expenditure and Epididymal Adipocyte Lipolytic Activity in Rat. Comparative Biochemistry and Physiology Part A: Molecular & Integrative Physiology. 1998;119:629–36.

125. Hammond SA, Tsonis C, Sellins K, Rushlow K, Scharton-Kersten T, Colditz I, et al. Transcutaneous immunization of domestic animals: opportunities and challenges. Adv Drug Deliv Rev. 2000;43:45–55.

126. Deng C, Paoloni-Giacobino A, Kuehne F, Boss O, Revelli J-P, Moinat M, et al. Respective degree of expression of β1, β2- and β3-adrenoceptors in human brown and white adipose tissues. British Journal of Pharmacology. 1996;118:929–34.

127. Lafontan M, Berlan M. Fat cell adrenergic receptors and the control of white and brown fat cell function. Journal of Lipid Research. 1993;34:1057–91.

128. Langin D, Tavernier G, Lafontan M. Regulation of beta3-adrenoceptor expression in white fat cells*. Fundamental & Clinical Pharmacology. 1995;9:97–106.

129. Kalhapure RS, Palekar S, Patel K, Monpara J. Nanocrystals for controlled delivery: state of the art and approved drug products. Expert Opinion on Drug Delivery. 2022;0:1–14.

130. Willmann A-C, Berkenfeld K, Faber T, Wachtel H, Boeck G, Wagner KG. Itraconazole Nanosuspensions via Dual Centrifugation Media Milling: Impact of Formulation and Process Parameters on Particle Size and Solid-State Conversion as Well as Storage Stability. Pharmaceutics. 2022;14:1528.

131. Mandal AB, Nair BU, Ramaswamy D. Determination of the critical micelle concentration of surfactants and the partition coefficient of an electrochemical probe by using cyclic voltammetry. Langmuir. 1988;4:736–9.

132. Li M, Alvarez P, Orbe P, Bilgili E. Multi-faceted Characterization of Wet-milled Griseofulvin Nanosuspensions for Elucidation of Aggregation State and Stabilization Mechanisms. AAPS PharmSciTech. 2018;19:1789–801.

133. Matteucci ME, Hotze MA, Johnston KP, Williams RO. Drug Nanoparticles by Antisolvent Precipitation: Mixing Energy versus Surfactant Stabilization. Langmuir. 2006;22:8951–9.

134. Gajera BY, Shah DA, Dave RH. Development of an amorphous nanosuspension by sonoprecipitation-formulation and process optimization using design of experiment methodology. International Journal of Pharmaceutics. 2019;559:348–59.

135. Dhumal RS, Biradar SV, Yamamura S, Paradkar AR, York P. Preparation of amorphous cefuroxime axetil nanoparticles by sonoprecipitation for enhancement of bioavailability. European Journal of Pharmaceutics and Biopharmaceutics. 2008;70:109–15.

136. Yonashiro H, Higashi K, Morikawa C, Ueda K, Itoh T, Ito M, et al. Morphological and Physicochemical Evaluation of Two Distinct Glibenclamide/Hypromellose Amorphous Nanoparticles Prepared by the Antisolvent Method. Mol Pharmaceutics. 2018;15:1587–97.

137. Stahr P-L, Grewal R, Eckert GP, Keck CM. Investigating hesperetin nanocrystals with tailor-made sizes for the prevention and treatment of Alzheimer's disease. Drug Deliv and Transl Res. 2021;11:659–74.

138. Colombo M, Staufenbiel S, Rühl E, Bodmeier R. In situ determination of the saturation solubility of nanocrystals of poorly soluble drugs for dermal application. International Journal of Pharmaceutics. 2017;521:156–66.

139. Romero GB, Arntjen A, Keck CM, Müller RH. Amorphous cyclosporin A nanoparticles for enhanced dermal bioavailability. International Journal of Pharmaceutics. 2016;498:217–24.

140. Cohen P, Kajimura S. The cellular and functional complexity of thermogenic fat. Nat Rev Mol Cell Biol. 2021;22:393–409.

141. Loh RKC, Formosa MF, La Gerche A, Reutens AT, Kingwell BA, Carey AL. Acute metabolic and cardiovascular effects of mirabegron in healthy individuals. Diabetes, Obesity and Metabolism. 2019;21:276–84.

142. Himms-Hagen J, Cui J, Danforth E, Taatjes DJ, Lang SS, Waters BL, et al. Effect of CL-316,243, a thermogenic beta 3-agonist, on energy balance and brown and white adipose tissues in rats. American Journal of Physiology-Regulatory, Integrative and Comparative Physiology. 1994;266:R1371–82.

143. Himms-Hagen J, Melnyk A, Zingaretti MC, Ceresi E, Barbatelli G, Cinti S. Multilocular fat cells in WAT of CL-316243-treated rats derive directly from white adipocytes. American Journal of Physiology-Cell Physiology. 2000;279:C670–81.

144. Than A, Liang K, Xu S, Sun L, Duan H, Xi F, et al. Transdermal Delivery of Anti-Obesity Compounds to Subcutaneous Adipose Tissue with Polymeric Microneedle Patches. Small Methods. 2017;1:1700269.

145. Than A, Duong PK, Zan P, Liu J, Leow MK-S, Chen P. Lancing Drug Reservoirs into Subcutaneous Fat to Combat Obesity and Associated Metabolic Diseases. Small. 2020;16:2002872.

146. Xie Y, Shao R, Lin Y, Wang C, Tan Y, Xie W, et al. Improved Therapeutic Efficiency against Obesity through Transdermal Drug Delivery Using Microneedle Arrays. Pharmaceutics. 2021;13:827.

147. Alexander A, Dwivedi S, Ajazuddin, Giri TK, Saraf S, Saraf S, et al. Approaches for breaking the barriers of drug permeation through transdermal drug delivery. Journal of Controlled Release. 2012;164:26–40.

148. Larrañeta E, Lutton REM, Woolfson AD, Donnelly RF. Microneedle arrays as transdermal and intradermal drug delivery systems: Materials science, manufacture and commercial development. Materials Science and Engineering: R: Reports. 2016;104:1–32.

149. Vicente-Perez EM, Larrañeta E, McCrudden MTC, Kissenpfennig A, Hegarty S, McCarthy HO, et al. Repeat application of microneedles does not alter skin appearance or barrier function and causes no measurable disturbance of serum biomarkers of infection, inflammation or immunity in mice in vivo. European Journal of Pharmaceutics and Biopharmaceutics. 2017;117:400–7.

150. Gnad T, Scheibler S, von Kügelgen I, Scheele C, Kilić A, Glöde A, et al. Adenosine activates brown adipose tissue and recruits beige adipocytes via A2A receptors. Nature. 2014;516:395–9.

151. Armani A, Marzolla V, Rosano GMC, Fabbri A, Caprio M. Phosphodiesterase type 5 (PDE5) in the adipocyte: a novel player in fat metabolism? Trends in Endocrinology & Metabolism. 2011;22:404–11.

152. Mitschke MM, Hoffmann LS, Gnad T, Scholz D, Kruithoff K, Mayer P, et al. Increased cGMP promotes healthy expansion and browning of white adipose tissue. The FASEB Journal. 2013;27:1621–30.

153. Zu Y, Zhao L, Hao L, Mechref Y, Zabet-Moghaddam M, Keyel PA, et al. Browning white adipose tissue using adipose stromal cell-targeted resveratrol-loaded nanoparticles for combating obesity. Journal of Controlled Release. 2021;333:339–51.

154. Sigurgeirsson B, Baran R. The prevalence of onychomycosis in the global population – A literature study. Journal of the European Academy of Dermatology and Venereology. 2014;28:1480–91.

155. Summerbell RC, Kane J, Krajden S. Onychomycosis, Tinea Pedis and Tinea Manuum Caused by Non-Dermatophytic Filamentous Fungi Nicht-Dermatophyten-Fadenpilze als Erreger von Onychomykosen, Tinea pedis und Tinea manuum. Mycoses. 1989;32:609–19.

156. Lipner SR, Scher RK. Onychomycosis: Treatment and prevention of recurrence. Journal of the American Academy of Dermatology. 2019;80:853–67.

157. Murdan S. Drug delivery to the nail following topical application. International Journal of Pharmaceutics. 2002;236:1–26.

158. Wang B, Zhou B, Zhang X, Wang B. Microstructure and mechanical properties of an alpha keratin bovine hoof wall. Journal of the Mechanical Behavior of Biomedical Materials. 2020;104:103689.

159. Celleno L. Topical urea in skincare: A review. Dermatologic Therapy. 2018;31:e12690.

8 List of Publications

Parts of this work have been published as follows:

Peer-reviewed journal articles

Kappes, S., Faber, T., Nelleßen, L., Yesilkaya, T., Bock, U., & Lamprecht, A. (2021). Improving Transungual Permeation Study Design by Increased Bovine Hoof Membrane Thickness and Subsequent Infection. *Pharmaceutics*, *13*(12). https://doi.org/10.3390/pharmaceutics13122098

Conference submissions and poster entries

Kappes, S., Nelleßen, L., Faber, T., Yesilkaya, T., Bock, U., & Lamprecht, A. (2022, 10.03). *Improving transungual permeation studies with bovine hoof membranes in vitro: Impact of thickness and infection with Trichophyton rubrum*. 88th Annual Meeting of the German Society for Experimental and Clinical Pharmacology and Toxicology (DGPT), Bonn.

Kappes, S., Faber, T., Bode, L., Krüger, C., Lamprecht, A., Nenoff, P., Uhrlaß, S., & Bock, U. (2023, 29.04). *Etablierung eines mit Trichophyton rubrum infizierten Rinderhuf-Modells zur Untersuchung der Permeation und In vitro-Aktivität von Antimykotika*. 52. DDG-Tagung, Berlin.

Appendix

The following pages entail the full publication “Improving Transungual Permeation Study Design by Increased Bovine Hoof Membrane Thickness and Subsequent Infection” by Sebastian Kappes, Thilo Faber, Lotta Nelleßen, Tanju Yesilkaya, Udo Bock and Alf Lamprecht, which was published in the journal Pharmaceutics by MDPI, Basel, Switzerland. This paper is available as an open access article at https://doi.org/10.3390/pharmaceutics13122098, and it is licensed under CC BY 4.0 (https://creativecommons.org/licenses/by/4.0/). © 2021 by the authors.

pharmaceutics

MDPI

Article

Improving Transungual Permeation Study Design by Increased Bovine Hoof Membrane Thickness and Subsequent Infection

Sebastian Kappes [1], Thilo Faber [1], Lotta Nelleßen [1], Tanju Yesilkaya [2], Udo Bock [3] and Alf Lamprecht [1,4,*]

[1] Department of Pharmaceutics, Institute of Pharmacy, University of Bonn, Gerhard-Domagk-Str. 3, 53121 Bonn, Germany; kappes.sebastian@uni-bonn.de (S.K.); thilo.faber@uni-bonn.de (T.F.); s6annell@uni-bonn.de (L.N.)
[2] Bayer Vital GmbH, 51373 Leverkusen, Germany; tanju.yesilkaya@bayer.com
[3] Bock Project Management, 54456 Tawern, Germany; udo.bock@bock-pm.com
[4] PEPITE EA4267, University of Burgundy/Franche-Comté, 25000 Besançon, France
* Correspondence: alf.lamprecht@uni-bonn.de; Tel.: +49-228-735-243; Fax: +49-228-735-268

Abstract: Ungual formulations are regularly tested using human nails or animal surrogates in Franz diffusion cell experiments. Membranes sometimes less than 100 µm thick are used, disregarding the higher physiological thickness of human nails and possible fungal infection. In this study, bovine hoof membranes, healthy or infected with *Trichophyton rubrum*, underwent different imaging techniques highlighting that continuous pores traversed the entire membrane and infection resulted in fungal growth, both superficial, as well as in the membrane's matrix. These membrane characteristics resulted in substantial differences in the permeation of the antifungal model substance bifonazole, depending on the dosage forms. Increasing the thickness of healthy membranes from 100 µm to 400 µm disproportionally reduced the permeated amount of bifonazole from the liquid and semisolid forms and allowed for a more pronounced assessment of the effects by excipients, such as urea as the permeation enhancer. Similarly, an infection of 400-µm membranes drastically increased the permeated amount. Therefore, the thickness and infection statuses of the membranes in the permeation experiments were essential for a differential readout, and standardized formulation-dependent experimental setups would be highly beneficial.

Keywords: ungual permeation model; onychomycosis; bovine hoof; bifonazole; scanning electron microscopy

Citation: Kappes, S.; Faber, T.; Nelleßen, L.; Yesilkaya, T.; Bock, U.; Lamprecht, A. Improving Transungual Permeation Study Design by Increased Bovine Hoof Membrane Thickness and Subsequent Infection. *Pharmaceutics* **2021**, *13*, 2098. https://doi.org/10.3390/pharmaceutics13122098

Academic Editor: Heather Benson

Received: 29 October 2021
Accepted: 1 December 2021
Published: 6 December 2021

1. Introduction

Almost five percent of the North American and European population is affected by fungal nail infection, mainly occurring on the toenails [1]. Such infections are mostly caused by dermatophytes and, to a lesser extent, by yeasts or molds. The dermatophyte *Trichophyton rubrum* (*T. rubrum*) alone accounts for about 90% of cases overall [2]. Common symptoms, including discoloration, brittleness, and deformation of the nail plate, can affect one's psychological well-being and, in severe cases, even lead to social isolation. If left untreated, such infections may spread to live tissue, promoting superinfections with additional microbial pathogens, ultimately causing pain and possibly impacting patients' mobility and general quality of life [3]. Despite the availability of highly effective antifungal agents, treatment is often insufficient, with high recurrence rates [4], as orally available actives carry the risk of severe side effects, and topical treatment usually requires monthlong treatment. This is due to the excellent barrier function of the nail, which consists of fused, flattened keratinocytes. The lipid content in the nail is low compared to the stratum corneum, and the resulting matrix can generally be described as hydrophilic [5,6]. Fungi growing inside and below the nail can therefore hardly be reached by active agents, as their typically highly lipophilic nature limits their partitioning into and diffusion through this matrix.

With cases of onychomycosis increasing and problematic drug-resistant strains of pathogens emerging [7,8], the development of formulations that surpass the limits imposed by the nail barrier has become increasingly important. Hence, adequate test systems to reliably assess the delivery of actives out of these formulations are needed. Typically, permeation studies are performed using Franz diffusion cells (FDC) equipped with different membranes. While human nails would provide the most realistic results, human cadaver nails require specialized diffusion cell geometry because of their curvature and are limited in availability. Besides the infectious risk, the variability of nail thicknesses and surface areas may lead to the high variability of study outcomes. Alternatively, nail clippings still do not eliminate an impractical curvature and provide only a small diffusion area, constraining their regular use in FDC setups. Synthetic membranes may enable the assessment of intrinsic release properties of formulations. However, they lack the physiological properties of a keratinous matrix, disregarding, for instance, the protein binding of substances, and are only a few micrometers thin. This disregard for the special density and properties of the keratinous matrix would lead to a high overestimation of permeations in vivo.

Therefore, bovine hoof sheets (BHS) were established as an in vitro surrogate for human nails in transungual permeation studies, as they are composed of α-keratin with a high sulfur content, comparable to human nails [9]. Following the established protocols for production resulted in membranes with reproduceable thicknesses and homologous morphology, possibly reducing the variance of in vitro permeation results [10]. Usually, 100–200-µm-thick BHS are used in permeation studies. Since, however, human nails are typically between 250 µm and 600 µm thick [11], such a thin BHS might also lead to the overestimation of antifungal drug permeation, due to a lack of barrier thickness and integrity. In addition, these models disregard the pathological state of nail infections, since they are mechanically, not sufficiently, stable after infection, which presumably impacts the permeation behaviors of actives.

In this work, it was investigated whether increasing the healthy BHS dimensions from 100 µm to a more physiologically relevant thickness of 400 µm and the subsequent infection with *T. rubrum* would be beneficial in providing ameliorated mechanical properties. In parallel, we elucidated to what extent the flux from different ungual dosage forms is impacted by such a difference in BHS thickness. For this purpose, bifonazole was chosen as an antifungal model substance and formulated as an ethanolic solution, nail patch, and nail lacquer with equal drug load, which were tested for their respective permeation behaviors. Two commercial products: Canesten® Extra Salbe and Canesten® Extra Creme served as the semisolid references. For interpretation of the results, extensive characterization of the BHS was conducted with different imaging techniques.

2. Materials and Methods

2.1. Materials

Bifonazole (BFZ) was purchased from TCI Deutschland GmbH (Eschborn, Hesse, Germany). Canesten® Extra Creme (CRE) and Canesten® Extra Salbe with (SAL) and without urea (SAL *w*/*o*) were kindly donated by Bayer Vital GmbH (Leverkusen, Germany). DuroTAK 2054 (DT) was a gift from Henkel AG & Co. KGaA (Düsseldorf, Germany), and Eudragit RL PO (RLPO) was donated by Evonik Industries (Essen, Germany). A spectra/Por®6, molecular weight cutoff 50-kDa dialysis membrane was purchased from Carl Roth (Karlsruhe, Germany). A ScotchPak™ 9733 backing liner was kindly donated by 3M (St. Paul, MN, USA). Ethanol absolute 99.8% was purchased from VWR International GmbH (Darmstadt, Germany). Triacetin, sodium phosphate dibasic dihydrate, and sodium chloride were purchased from Sigma Aldrich (Steinheim, Baden-Württemberg, Germany). Potassium dihydrogen phosphate was purchased from Carl Roth (Karlsruhe, Germany). Potassium chloride was purchased from Merck (Darmstadt, Germany). The chemicals used for the dosage form or buffer preparation were of analytical grade or higher.

2.2. Preparation of Solution (SOL)

One percent (*w/w*) BFZ was dissolved in absolute ethanol at room temperature under stirring until a clear solution was obtained.

2.3. Preparation of Lacquer (LAC)

Twenty percent (*w/w*) RLPO and 1% (*w/w*) BFZ referring to the dry film mass were completely dissolved in ethanol under stirring, and 5% (*w*/*w*) triacetin was added subsequently analogous to Yang et al. [12]. A solid-state analysis was conducted using escalated drug loads of 10 and 20% (*w*/*w*) to enhance the sensitivity of the methods to recrystallization in the matrix.

2.4. Preparation of Patch (PAT)

One percent (*w*/*w*) BFZ related to the solid content of an adhesive in the solution was added to the matrix and dissolved under stirring. The solution was then cast onto backing liner with a wet film applicator (Multicator 411, Erichsen, Hemer, Germany) with a wet film thickness of 1000 µm. The patches were allowed to rest at an ambient temperature for 15 min and then dried at a temperature of 65 °C for 30 min. Before application, the patches were cut into rectangular pieces of 2 cm^2. The patch matrices with enhanced drug loads of 10 and 20% (*w*/*w*) were prepared to increase the sensitivity of the methods and were subsequently assessed for crystallinity.

2.5. Polarized Light Microscopy (PLM)

PLM images were taken with a Leica DM 2700M (Leica microsystems, Wetzlar, Germany) equipped with a MicroPublisher 5.0 RTV camera (Teledyne Photometrics, Tucson AZ, USA). Images were captured using Q-Capture Pro 7 software version 7.0.5. Samples were prepared by casting the respective matrix directly onto microscope slides, followed by the same drying procedure employed in preparation of the final dosage forms.

2.6. Differential Scanning Calorimetry (DSC)

DSC measurements were conducted using a Mettler-Toledo DSC 2 (Gießen, Germany) that was equipped with a nitrogen cooling system using nitrogen as the purge gas (30 mL/min). Samples were weighed on aluminum pans at 5–15 mg and closed with a pierced lid. The glass transition temperature and melting point for neat BFZ were determined using a heat–cool–heat cycle (25 °C to 170 °C to −50 °C to 170 °C) with a heat rate of 10 K/min. The glass transition temperatures and melting points for the polymer films and patch matrices were investigated using TOPEM mode with a heat rate of 2 K/min from −70 °C to 170 °C with a pulse height of 1 K.

2.7. X-ray Diffraction (XRD)

XRD was performed in transmission mode on X'Pert MRD Pro by PANalytical (Almelo, The Netherlands) equipped with an X'Celerator detector. Nickel-filtered CuKα1 radiation was generated at 45 kV and 40 mA. Scanning was performed in a range from 17° to 20° 2Θ containing the most prominent reflection peaks, with a step size of 0.017°.

2.8. X-ray Microtomography (µCT)

µCT scans of 400 µm BHS were performed using Bruker SKYSCAN 1272 (Kontich, Belgium) equipped with a Hamamatsu L11871-20 x-ray source and a XIMEA xiRAY16 camera with a pixel size of 7.4 µm. The membranes were first submerged in 2.5% (*w*/*v*) glutaraldehyde solution for fixation and subsequently put in 2% (*w*/*v*) OsO_4 solution to increase the contrast. The scanning parameters were set to 60-kV source voltage, the current to 166 µA, a 0.25-mm Al filter, an image rotation of 188.4° with a step size 0.4°, a 1900-ms exposure time, and about 1 h 8 min of scan time. Initial image reconstruction was conducted with NRecon software version 1.7.1.0 (Kontich, Belgium). Volume rendering

and stack analysis of the figures shown were performed using free ImageJ software version 1.53c (https://imagej.nih.gov/ij/ accessed on 11 December 2020).

2.9. Preparation of Bovine Hoof Sheets

Cattle hooves for membrane preparation were procured from a local abattoir on the day of slaughter for human consumption. As these were a byproduct in proper food production and animals were not bred, kept, or sacrificed for scientific purposes but for food production only, ethics committee approval was not required. The membranes were prepared analogous to the method described by Mertin and Lippold [13]. In brief, hooves were cut into 2 cm × 2 cm squares, submerged in distilled water for 3 d, and subsequently cut with a rotational microtome to 100-µm and 400-µm-thick membranes.

2.10. Scanning Electron Microscopy (SEM) and Focused Ion Beam Scanning Electron Microscopy (FIB-SEM)

Infected and healthy sheets were glued to aluminum stubs with silver conductive paint and sputter-coated with platinum (Q150TS Quorum Technologies, Lewes, UK).

Electron microscopy and focused ion beam milling were performed using a Helios G4 CX Dualbeam microscope (Thermo Fisher Scientific, Eindhoven, The Netherlands). Secondary electron images were taken using a 2–10 kV accelerating voltage at 4 mm working distance. Rough Fib milling was performed on stained membranes using 30-kV accelerating voltage and a 9.3-nA current. The fine polishing of the revealed cross-section was done at 30 kV and a 43-pA current.

2.11. Infection of Bovine Hoof Sheets

BHS were infected with *T. rubrum* over a period of 9 d. Infection was performed according to a slightly modified procedure by Lusiana et al. [14]. Inoculation of hoof sheets was started by 30-min maceration in a physiological saline solution. Sabouraud–Agar plates (Becton Dickinson GmbH, Heidelberg, Germany) with gentamicin and chloramphenicol were struck with a cotton swab containing *T. rubrum* in a physiological saline solution in one direction, applying a zig-zag pattern. Agar plates were dried for 10 min. Subsequently, BHS were placed on top and their surfaces moistened with the same swab. BHS were incubated for 9 days at 30 °C ± 2 °C. After colonization, the BHS were disinfected by 3 h of treatment in 70% (*v*/*v*) ethanol and subsequent UV exposure for 1 h. Membranes with similar colors, corresponding to the level of infection without visible damage such as cracks, were selected for further experiments.

2.12. Permeation across Synthetic Membranes

Release from the formulations was assessed using vertical Franz diffusion cells (FDC) with an acceptor volume of 8 mL and diffusion area of 1 cm^2. A regenerated cellulose membrane with a molecular weight cutoff of 50 kDa was mounted between the donor and acceptor compartments. To achieve sink conditions throughout the experiment, the receiver consisted of 42% (*v*/*v*) ethanol in phosphate-buffered saline, pH 7.4 [15] that was stirred at 200 rpm, and the FDC were maintained at 32 °C. A dose of 200 mg in the cases of SAL, CRE and SOL was applied to the membrane. Three hundred and fifty microliters of LAC were applied to the donor as the solution and allowed to dry overnight before filling the receiver to start the experiment. PAT were applied directly onto the the membrane before insertion into FDC. Samples of 0.5 mL were taken hourly up to 6 h and after 24 h and analyzed by HPLC-DAD. The removed volume was immediately replaced with fresh receiver solution.

2.13. Permeation across Bovine Hoof Sheets

Permeation studies in vitro were carried out over 6 days in vertical FDC with an acceptor volume of 5.5 mL and a diffusion area of 0.785 cm^2. The other conditions were kept in accordance to experiments with synthetic membranes. BHS were hydrated in the

receiver for 24 h prior to insertion into the FDC. The applied dose for each dosage form was analogous to the synthetic membrane experiments, and the donor was replaced daily for SAL, CRE and SOL with cotton swabs to account for the higher depletion of BFZ in immediate release formulations. Due to the low adherence of SAL to swabs, the residual donor was further removed by the careful use of a plastic spatula. Samples of 0.5 mL were taken daily after 24 h and analyzed by HPLC-DAD. A removed volume was immediately replaced with a fresh receiver solution.

2.14. High-Performance Liquid Chromatography (HPLC) Analysis

An analysis was conducted on an Agilent 1100 system coupled with an Agilent G1316A detector using a C18 reverse-phase column (LiChrospher® 100 RP 18 EC–5µ; 125-mm length, 4.6-mm inner diameter, and 5-µm particle size). The eluent consisted of acetonitrile and 20-mM sodium phosphate buffer, pH 7.4 (70/30, % *v*/*v*) set to a flow of 1 mL/min. The column temperature was maintained at 25 °C, and the autosampler was left at room temperature. The injection volume was 40 µL, and the detector was set to 256 nm. The limit of quantification was 100 ng/mL. Its specificity was ensured by injection of a BFZ standard from methanol and from a FDC receiver medium, aliquots of dosage forms, pure receiver medium, and receiver medium previously incubated with BHS. No peaks interfered with the BFZ peak. The following parameters were evaluated: slope = 169.0; y-intercept = −1.550; R^2 = 0.9993; linear range = 0.1–11 µg/mL; retention time = 4.5 min; repeatability = 0.4%; interday variations = 2.1%; and accuracy = 104 ± 1.4%, 94.7 ± 1.5%, and 97.5 ± 0.5% for concentrations of 0.2, 1.5, and 4 µg/mL, respectively.

2.15. Statistical Evaluation

All experiments were conducted in triplicate at least. The flux was calculated using at least three terminal linear data points. Data were presented as the mean ± standard deviation. A statistical analysis for significance was conducted using GraphPad Prism 8 software Welch's *t*-test. The results were recognized as statistically significant if $p < 0.05$ and marked with an asterisk. The results were considered very significant if $p < 0.01$ and extremely significant if $p < 0.001$ and marked with two or three asterisks, respectively.

3. Results

3.1. Image Characterization of Bovine Hoof Membranes

µCT and SEM images depicted a smooth-to-wavy surface texture with a multitude of porous structures on the membrane's surface (Figure 1A,B). Some structures on the surface appeared to be during in SEM, while some were visibly open, with a diameter of up to roughly 50 µm. Further examination by µCT revealed pores extending coherently throughout the whole membrane transversally as brighter areas against the darker keratin matrix (Figure 2B,C). Exemplary focusing of such a pore in the middle of the membrane's diameter (yellow cross) showed a hollow area visible from each axis that continued transversally as a dark crack. Further FIB milling of the matrix around these pores and the subsequent imaging of the resulting cross-section revealed that, although pores may seem to be closed or superficial, hollow structures continued beneath the surface, connecting to deeper membrane layers (Figure 1B). SEM imaging of the infected BHS showed the dense, superficial growth of fungal hyphae, completely covering the membrane's surface (Figure 3A). Imaging of a fracture cross-section revealed that fungi also grew into the membrane (Figure 3B).

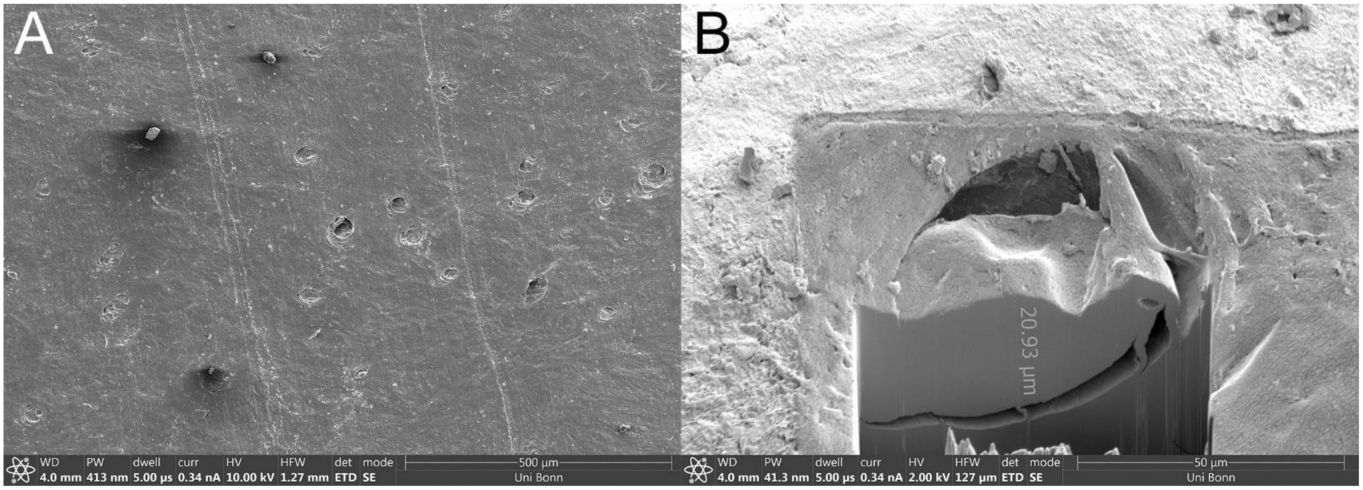

Figure 1. Scanning electron microscopy images of a bovine hoof sheet surface: (**A**) porous structures spread over the entire surface and (**B**) exemplarily focused ion beam milling of a pore reveals continuation into the membrane matrix.

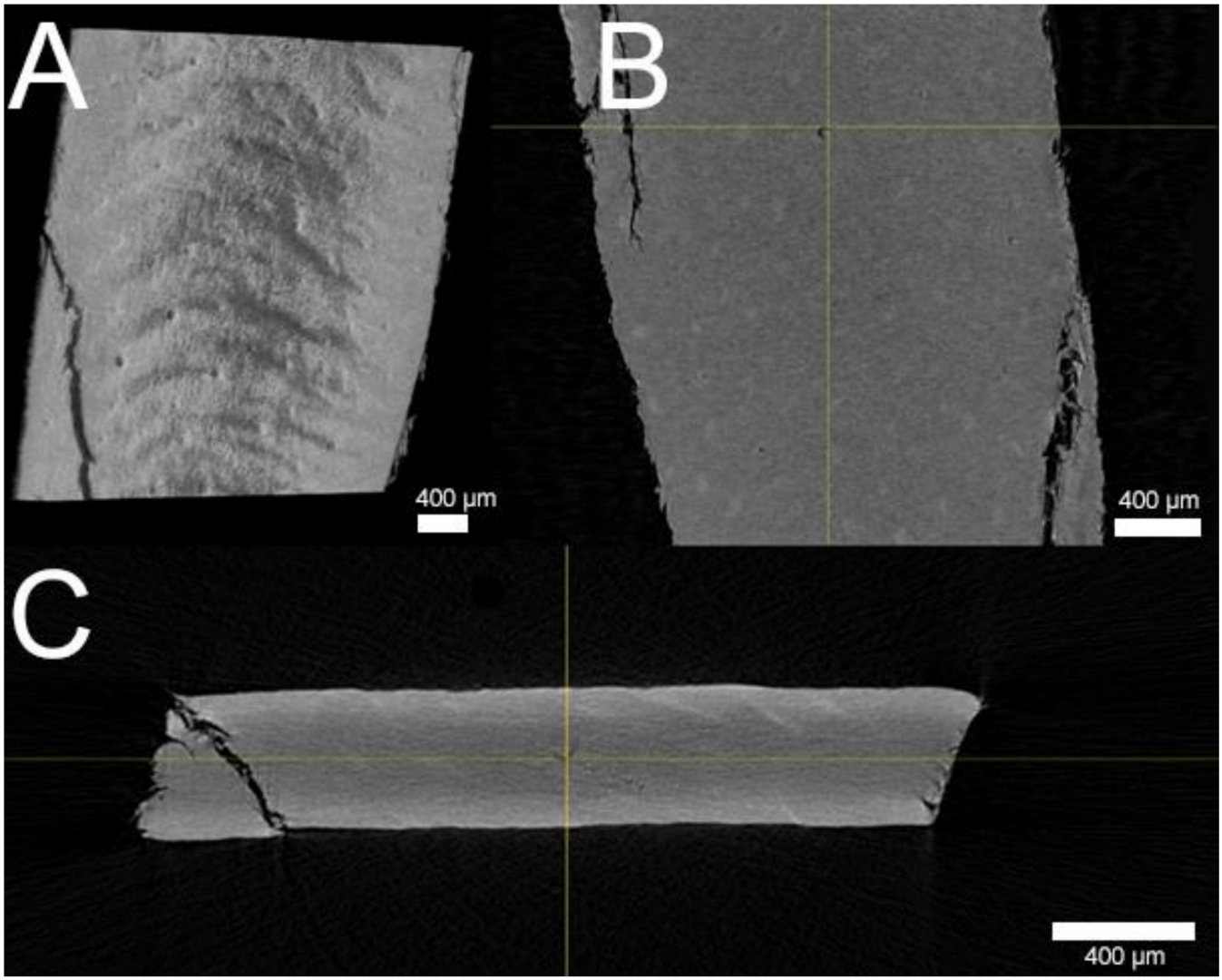

Figure 2. Volume rendering of x-ray microtomography bovine hoof sheet (BHS) images. (**A**) Surface of BHS in the Y-direction with various porous cavities visible. (**B**) Focused hollow pore (yellow cross) inside the BHS matrix in the Y-direction and (**C**) Z-direction, revealing continuation of the pore as a dark crack from the top left to bottom right; each scale bar = 400 µm.

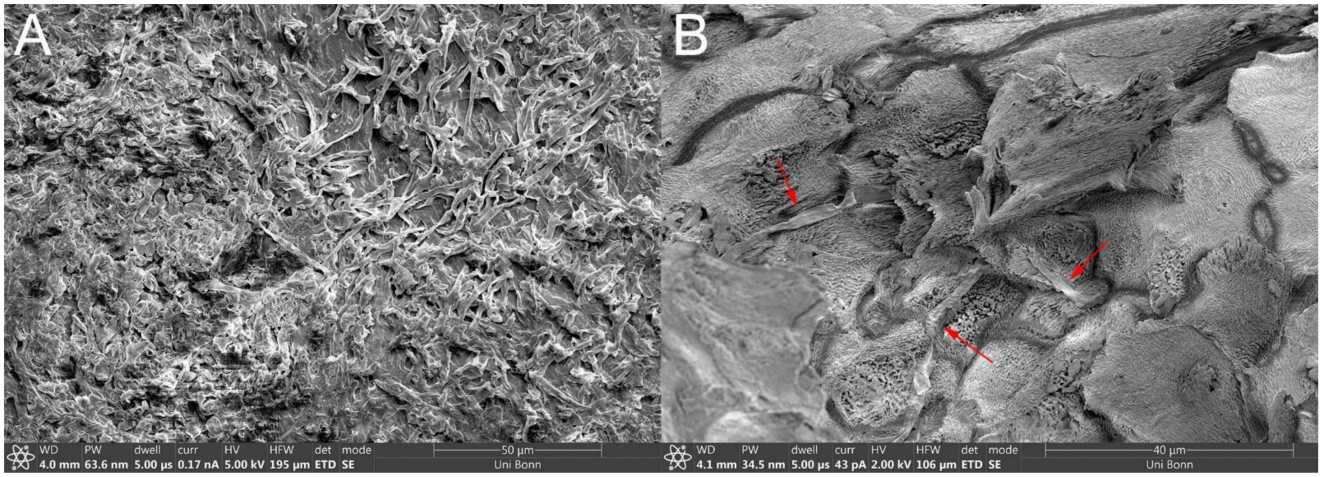

Figure 3. Scanning electron microscopy images of infected 400-µm bovine hoof sheets: (**A**) dense growth of fungi over the entirety of the membrane surface, and a (**B**) cross-section fracture reveals fungal growth inside the membrane matrix, fungal hyphae, indicated by arrows.

3.2. Solid State of PAT and LAC

A solid-state analysis of PAT and LAC showed an absence of crystallinity for 1% and 10% BFZ formulations, whereas, for the 20% drug load, crystals could be observed with the PLM and BFZ melting peaks and reflexes that occurred in the thermogram and diffractogram. For the PLM photographs, thermograms, and diffractograms, please refer to the Supplementary Materials (Figures S1–S3).

3.3. Permeation across Synthetic Membrane

Plotting the permeated amount of BFZ per diffusion area against the square root of time allowed an assessment of the flux for all the dosage forms (Figure 4). SOL's permeation, followed a sigmoidal pattern, resulted in the highest total permeation after 24 h. While the instant release dosage forms CRE and SAL showed similar releases over the first 3 h, CRE released roughly 1.7 times the amount of BFZ compared to SAL after 24 h. In comparison, the extended-release dosage forms released significantly less than BFZ. LAC released about 26% of semisolid reference CRE, whereas the amount of BFZ liberated from PAT amounted to 16% of CRE.

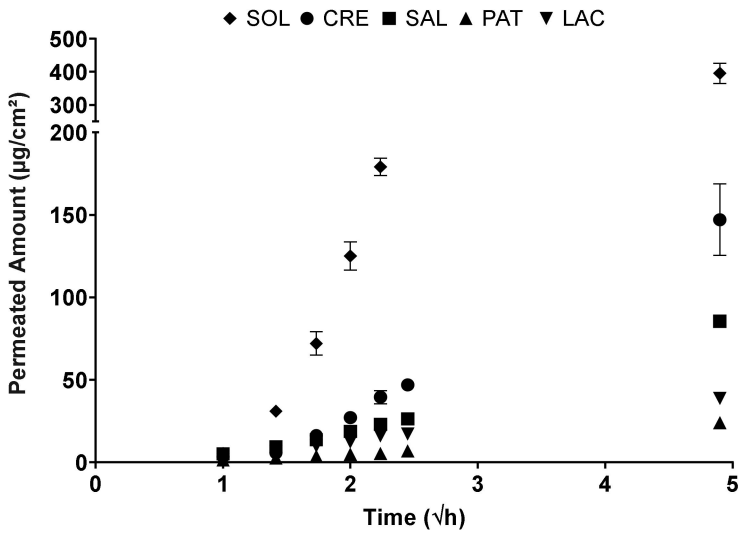

Figure 4. Permeation of bifonazole (BFZ) out of the solution (SOL), Canesten® Extra Creme (CRE), Canesten® Extra Salbe (SAL), patch (PAT), and lacquer (LAC) across a synthetic regenerated cellulose membrane (mean ± SD).

3.4. Permeation across Bovine Hoof Sheets

Linear permeation profiles for all the dosage forms over the course of 6 days were established for membranes 100 µm and 400 µm thick (Figure 5). For CRE and SAL, the permeations were linear over the course of 14 d at least (data not shown). For 100-µm-thick membranes, SOL clearly showed the highest permeation, with 256.0 ± 69.1 µg/cm^2 of permeated BFZ after 6 d. The immediate release dosage forms CRE and SAL showed similar permeation profiles with no statistically significant differences between them, resulting in 80.8 ± 15.7-µg/cm^2 and 90.0 ± 12.3-µg/cm^2 permeating. Permeated amounts from the PAT and LAC were distinctly lower than with the other formulations, with 24.6 ± 3.4 µg/cm^2 permeated out of PAT in contrast to LAC with only 9.0 ± 3.8 µg/cm^2.

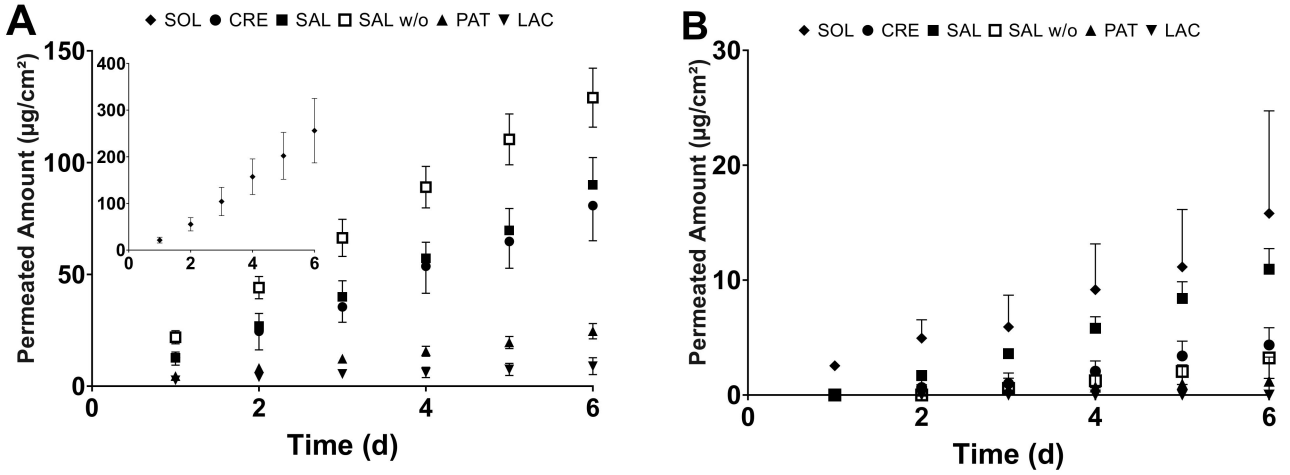

Figure 5. Permeation of bifonazole (BFZ) out of the solution (SOL), Canesten® Extra Creme (CRE), Canesten® Extra Salbe (SAL), Canesten® Extra Salbe without urea (SAL *w/o*), patch (PAT) and lacquer (LAC) across (**A**) 100-µm and (**B**) 400-µm healthy bovine hoof sheets (mean ± SD).

For 400-µm-thick BHS, SOL still showed the highest onset of permeation and resulted in 15.8 ± 8.9 µg/cm^2 permeated after 6 d. However, while showing a slower onset, the SAL was similar over the course of 6 d, releasing 11.0 ± 1.8 µg/cm^2 into the receiver medium. While no difference could be observed in the 100-µm setting, the SAL clearly delivered more BFZ than CRE, which only showed a permeation of 4.4 ± 1.5 µg/cm^2, similar to PAT with 1.2 ± 2.5 µg/cm^2. In the case of LAC, no permeation could be observed in any FDC over the course of the experiment.

Regarding the permeation of SAL *w/o* after 6 d, 129.1 ± 13.2 µg/cm^2 permeated across 100-µm BHS, whereas 3.2 ± 1.8 µg/cm^2 permeated in the case of 400 µm.

In general, increasing the membrane's thickness to 400 µm led to a disproportional decrease in the flux when compared to 100 µm for all dosage forms, as shown by normalization to a membrane thickness of 100 µm (Figure 6). The normalized flux was significantly different for every immediate release dosage form. Between 100 and 400 µm, normalized fluxes for SOL, CRE, SAL, SAL *w/o* and PAT differed by factors of 4.0, 3.0, 1.4, 5.2 and 4.0, respectively, while, for LAC, no factor could be derived due to no observable permeation across 400 µm. Furthermore, no significant difference could be observed between CRE, SAL, and SAL *w/o* in the 100-µm setting. However, increasing the membrane thickness to 400 µm resulted in a significantly different flux between the CRE and SAL, as well as an increased permeation of SAL compared to SAL *w/o*.

3.5. Permeation across Infected Bovine Hoof Sheets

Infecting 400-µm-thick BHS with *T. rubrum* for 9 d provided membranes with non-increased thicknesses to healthy BHS, which were of sufficient robustness for use in FDC experiments. The surfaces' colors changed from opaque white to a reddish brown in the infected state. The permeation profiles for CRE and SAL exhibited a similar flux to healthy

400-µm membranes that could be observed for SAL, resulting in a 13.4 ± 2.1-µg/cm^2 amount permeated (Figure 7). Then again, the flux of CRE increased in the infected model over the noninfected one and approached that of SAL, with 8.7 ± 3.9 µg/cm^2 permeated after 6 d. In addition to the permeation results, the infected BHS surface lost its discoloring when treated with SAL, undergoing careful daily formulation exchanges with a plastic spatula. Comparably, the BHS surface of CRE-treated BHS whose donor was exchanged with cotton swabs did not alter their color in a similar fashion (see Supplementary Materials Figure S4).

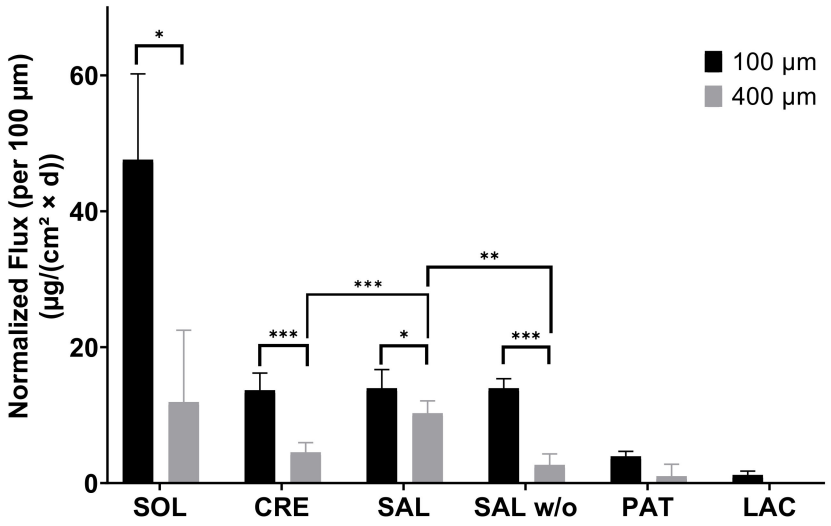

Figure 6. Respective fluxes of bifonazole through 100-µm and 400-µm healthy bovine hoof sheets (mean ± SD). Significance levels: * $p < 0.05$; ** $p < 0.01$; *** $p < 0.001$.

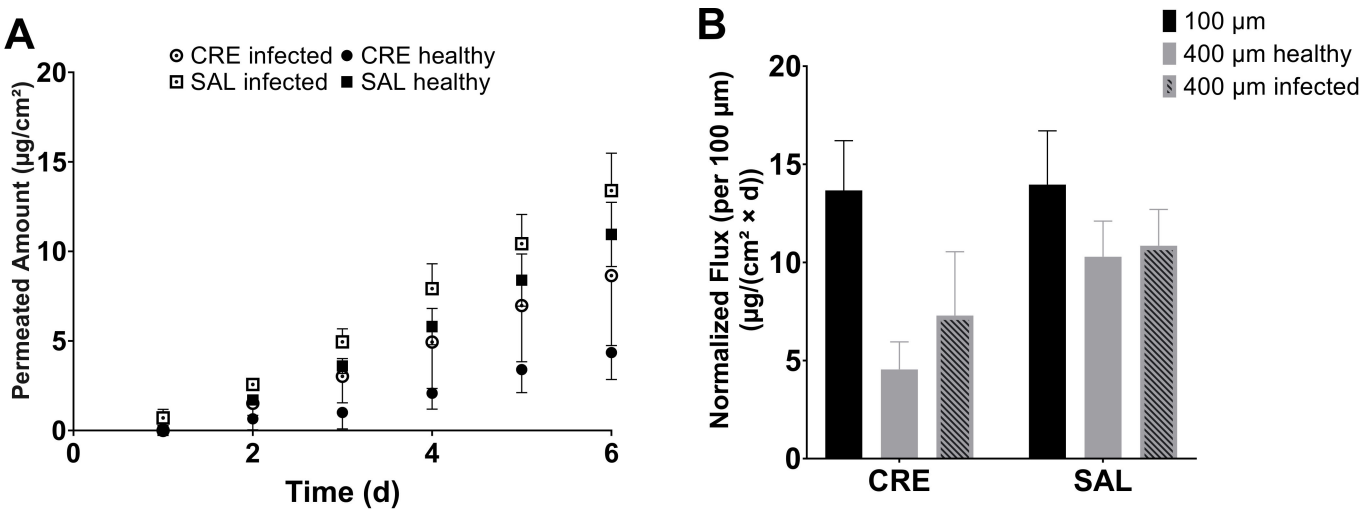

Figure 7. (**A**) Permeation of bifonazole from Canesten® Extra Creme (CRE) and Canesten® Extra Salbe (SAL) across 400-µm bovine hoof sheets and healthy and infected with *T. rubrum* (mean ± SD). (**B**) Respective fluxes of bifonazole through 100-µm and 400-µm healthy and infected membranes (mean ± SD).

4. Discussion

When implementing BHS as a surrogate model for human nails, Mertin and Lippold found BHS to be less dense, with an increased swelling capacity compared to human nails, resulting in a higher permeability [15]. However, upon verifying the integrity of their membranes via SEM imaging, they stated an absence of pores but existence of cavities [13]. In contrast to their findings, using the FIB milling technique combined with SEM imaging, these cavities were shown not to be superficial but connect to deeper membrane levels.

The additional investigation of these structures with µCT imaging further confirmed the existence of connected, transversally proceeding hollow cracks. The porosity of BHS and human nails was investigated by Nogueiras-Nieto et al. using mercury intrusion porosimetry [16]. Agreeing with our findings, their study showed that dry BHS had a pronounced porosity at the surface; yet, the internal structure of BHS had a low porosity. The hydration of both human nails and BHS increased the porosity and interconnection of the keratinous network. As revealed by our imaging, the decline of porosity in the deeper membrane levels in these studies might be due to a blockade of porous tunnels by keratinous debris. The properties of bovine claw horn were investigated by Baillie et al. [17]. Using a light microscope, they demonstrated continuous tubules running through the bovine hoof, which were shown to be hollow in SEM fracture specimens by Wang et al. [18]. Despite the hydration, freezing, and cutting steps in preparation of the BHS, these tubules were not closed, as revealed by µCT and FIB-SEM. Thus, it is very likely that channels filled with the receiver medium are present in FDC experiments. These channels presumably act as shunt routes, facilitating permeations. Therefore, an increased membrane thickness might reduce the effect of such routes through the increased chance of debris in tubules and a longer route of diffusion for APIs and subsequently lead to more appropriate datasets than with thinner BHS.

Bifonazole transport across a regenerated cellulose membrane showed a distinct order for the different dosage forms. SOL, CRE, and SAL, in that order, showed much more pronounced permeations compared to the matrix forming LAC and PAT, which could be attributed to the presumed increased diffusivity of BFZ in these liquid and semisolid dosage forms. The permeated amount out of LAC was higher than PAT, despite a presumably lower diffusivity of BFZ, which may be due to a lower hydrophobicity of RLPO compared to DT, enabling a more efficient solvent uptake and diffusion through the matrix. As the dialysis membrane does not possess the retention potential for small molecules, these findings can be interpreted as a BHS membrane with an infinite number of pores and short ways of diffusion. Similar to the synthetic membrane, the 100-µm-thick BHS allowed for differentiation between liquid, semisolid, and solid formulations with the same drug load of BFZ. However, while SOL maintained the highest permeation and the rankings of LAC and PAT reversed, possibly due to less direct contact of the dosage form with the receiver medium, the former difference between CRE and SAL became insignificant, as the barrier properties of BHS became the limiting factor of diffusion in contrast to the dialysis membrane. Naumann et al. were able to assess the permeation of a novel antifungal agent from a solution, a lacquer, a hydrogel, and a colloidal carrier system [19]. In their study, using an FTIR-ATR diffusion cell, they showed the highest permeation from the solution followed by emulsion, with the lacquer and hydrogel being significantly worse, thus confirming the revealed applicability of 60–150-µm-thick BHS for the general comparison of dosage forms. Further studies were conducted by Monti et al., who successfully compared the permeations of amorolfine and ciclopirox from the same hydrophilic vehicle using 80–120-µm BHS [20]. Their report reinforced these membranes as tools that allow quantifiable and comparable permeation results from lacquers for different APIs.

The effects of penetration enhancers have been reported for BHS of 60-µm and 200-µm thickness for lacquers [12,21]. In these studies, urea was shown to act as a potent enhancer of transungual permeation, facilitating the delivery of terbinafine hydrochloride and amorolfine hydrochloride. However, urea seemingly did not enhance the permeation from SAL compared with CRE, and the permeation from SAL w/o was even higher in the 100-µm BHS system. Regardless, the flux was not significantly different between SAL, SAL w/o, and CRE, whereas, across 400-µm-thick membranes, the BFZ permeation of SAL was significantly higher than that of CRE or SAL w/o. Therefore, although already much more limiting than the dialysis membrane, in the 100-µm BHS setup, the high amount of BFZ intrinsically released from immediate-release dosage forms overshadowed the penetration-enhancing effects when confronted with too weak of a barrier. In addition,

effects of lower viscosity might have resulted in a faster onset of permeation for less viscous SAL *w/o* in contrast to pasty SAL, explaining the resulting difference in the permeated amount across 100-µm BHS. Using 200–250-µm-thick BHS, Park et al. investigated the influence of lipophilic and hydrophilic permeation enhancers on the transungual delivery of hydroalcoholic and oily eficonazole solutions [22]. For hydrophilic enhancers, their study allowed accurate discrimination between the respective formulations. Further studies with penetration enhancers were performed by Cutrín-Gómez et al., in which they used 300–700-µm membranes and studied the enhancers' effects on the membrane surface morphology and porosity [23]. They concluded that enhancers, such as sodium laureth sulfate, or acetylcysteine had a porosity-increasing effect on the matrix. Thus, thicker membranes, which provide more keratinous material in comparison to the already existing porous structures, would yield an increased response. Since the permeations from immediate release dosage forms throughout increased disproportionally to the thickness of the respective membrane, independent of any penetration-enhancing substances, the enhancing effects of the formulations could be neglected, and the pores in the membrane were identified as a likely cause by SEM and µCT imaging. The choice of the right membrane in this particular test system is of utmost importance to obtain the most reliable results for the use of a formulation. Therefore, to simulate infection of the nail, BHS of 400-µm thickness were infected with *T. rubrum.* The commercial products CRE and SAL were chosen for further investigation in this arrangement to best mimic actual use conditions, where the application of SAL is recommended for two weeks prior to application of CRE to evaluate whether the infected model would maintain the observed differences in the healthy setup, thus supporting this recommendation. Although SAL showed similar permeations to healthy membranes, the permeations from CRE were increased in the infected model. As shown by the SEM images, the fungi grew into the membrane rather than just superficially. Hence, an increase in porosity due to digestion of the keratinous matrix by fungi is highly probable. This higher porosity of the membrane increased the flux mainly for CRE, which benefited more from the increased porosity analogous to the 100-µm BHS, correlating with higher intrinsic liberation characteristics. Although the delivery from SAL was not increased, the infected matrix was removed with a daily exchange of the donor, as the keratolytic effect of urea probably broke up the outermost layers, facilitating removal in contrast to CRE. An increase in porosity by fungal infection for human nails and resulting trends for increased flux for ciclopirox olamine and clobetasol propionate were reported by Cutrín-Gómez et al. [24]. BHS and keratin films of human hair were infected with *T. rubrum* by Lusiana et al. and Kracht et al. [14,25]. In their work, the infected membranes were inoculated on agar plates, an antifungal formulation was applied, and the fungal growth was assessed after a period of time to determine the efficacy of the formulations. While this setup allows for the rapid screening of multiple formulations, it does not allow for the assessment of permeation parameters, unlike the use of infected BHS in transungual FDC experiments. In addition, the infected FDC setup enabled the discovery of diverse formulation effects on the nail membrane, such as keratolysis, as demonstrated by removal of the superficially infected matrix by treatment with SAL, which could not be elucidated in previous studies.

In this work, BFZ was studied as a model drug, being a representative candidate in this therapeutic indication, with the main focus on establishing an ameliorated tool for comparative studies between the different dosage forms. The observations underline the importance of selecting an appropriate membrane when planning studies of permeations from ungual formulations. Thus, future studies with different APIs and dosage forms could benefit from the demonstrated applicability of different BHS thicknesses and infection statuses. Although seemingly different permeation mechanisms were involved with the respective dosage forms in the dependance of membrane thickness and infection, the observed differences could not completely be explained mechanistically yet. However, this modified model offers a foundation for a more rational experimental setup in formulation development. Nevertheless, exploring further mechanistical insights into the influence

of thickness and infection will be helpful to refine the model's applicability to other therapeutic scenarios.

5. Conclusions

Bovine hoof sheets have rightfully been established as a surrogate for human nails in in vitro test systems, as they allow for rather physiological, yet still sufficiently fast, assessments of permeation characteristics of typically employed formulations, most of all lacquers. However, for liquid or semisolid formulations, shunt routes, in the form of naturally grown pores, drastically increase the permeation upon lowering the membrane's thickness. Only with membranes thick enough to effectively limit diffusion does it become possible to reach a reasonable resolution between SAL and CRE in order to detect the potential permeation-enhancing effects, as found in this study, with urea in SAL. The infection of BHS increased the permeation similarly to lowering the membrane thickness and further allowed for an inspection of the formulations' effects on removal of the infected matrix. This model design significantly increased the nail thickness, enabling to identify and prove a therapeutic regimen essentially based on the dosage form design, such as in the urea containing semisolid formulation given here combining a rapid drug delivery into the nail matrix with simultaneous removal of the nail matrix. Accordingly, standards would be highly useful in guiding the selection of thickness and infection status of bovine hoof sheets in view of the particular dosage form and the therapeutic regimen.

Supplementary Materials: The following are available online at https://www.mdpi.com/article/10.3390/pharmaceutics13122098/s1: Figure S1: PLM images of PAT and LAC. Figure S2: X-ray diffractograms of PAT and LAC. Figure S3: Thermograms of PAT and LAC. Figure S4: Surfaces of infected 400-µm BHS treated with SAL and CRE.

Author Contributions: Conceptualization, S.K., U.B., and A.L.; methodology, S.K., U.B., and A.L.; formal analysis, S.K.; investigation, S.K., L.N., and T.F.; resources, T.Y., U.B., and A.L.; data curation, S.K.; writing—original draft preparation, S.K.; writing—review and editing, S.K., T.F., T.Y., U.B., and A.L.; supervision, U.B. and A.L.; project administration, A.L.; and funding acquisition, T.Y., U.B., and A.L. All authors have read and agreed to the published version of the manuscript.

Funding: This research project was partially funded by Bayer Vital GmbH, Leverkusen, Germany.

Institutional Review Board Statement: Not Applicable.

Informed Consent Statement: Not applicable.

Data Availability Statement: Not applicable.

Acknowledgments: We kindly thank Henkel, 3M and Evonik for providing the samples. We further thank Alexander Ziegler, Institute of Evolutionary Biology and Ecology, University of Bonn, Germany for performing the µCT scans and Kevin Kayser, Institute of Pharmacy, University of Bonn, Germany for assisting in the DSC measurements and evaluation. Constanze Krüger, a laboratory for Medical Microbiology, Mölbis, Germany performed infection studies with *T. rubrum*.

Conflicts of Interest: This research was partially sponsored by Bayer Vital GmbH. T.Y. is an employee of Bayer Vital GmbH. The company had no role in the design of the study; in the collection, analyses, or interpretation of data; in the writing of the manuscript, or in the decision to publish the results. The other authors declare no conflict of interest.

References

1. Sigurgeirsson, B.; Baran, R. The Prevalence of Onychomycosis in the Global Population – A Literature Study. *J. Eur. Acad. Dermatol. Venereol.* **2014**, *28*, 1480–1491. [CrossRef] [PubMed]
2. Summerbell, R.C.; Kane, J.; Krajden, S. Onychomycosis, Tinea Pedis and Tinea Manuum Caused by Non-Dermatophytic Filamentous Fungi Nicht-Dermatophyten-Fadenpilze Als Erreger von Onychomykosen, Tinea Pedis Und Tinea Manuum. *Mycoses* **1989**, *32*, 609–619. [CrossRef] [PubMed]
3. Stewart, C.R.; Algu, L.; Kamran, R.; Leveille, C.F.; Abid, K.; Rae, C.; Lipner, S.R. Effect of Onychomycosis and Treatment on Patient-Reported Quality-of-Life Outcomes: A Systematic Review. *J. Am. Acad. Dermatol.* **2021**, *85*, 1227–1239. [CrossRef] [PubMed]

4. Lipner, S.R.; Scher, R.K. Onychomycosis: Treatment and Prevention of Recurrence. *J. Am. Acad. Dermatol.* **2019**, *80*, 853–867. [CrossRef] [PubMed]
5. Kobayashi, Y.; Miyamoto, M.; Sugibayashi, K.; Morimoto, Y. Drug Permeation through the Three Layers of the Human Nail Plate. *J. Pharm. Pharmacol.* **1999**, *51*, 271–278. [CrossRef] [PubMed]
6. Walters, K.A.; Abdalghafor, H.M.; Lane, M.E. The Human Nail—Barrier Characterisation and Permeation Enhancement. *Int. J. Pharm.* **2012**, *435*, 10–21. [CrossRef] [PubMed]
7. Nenoff, P.; Verma, S.B.; Vasani, R.; Burmester, A.; Hipler, U.-C.; Wittig, F.; Krüger, C.; Nenoff, K.; Wiegand, C.; Saraswat, A.; et al. The Current Indian Epidemic of Superficial Dermatophytosis Due to Trichophyton Mentagrophytes—A Molecular Study. *Mycoses* **2019**, *62*, 336–356. [CrossRef] [PubMed]
8. Gupta, A.K.; Renaud, H.J.; Quinlan, E.M.; Shear, N.H.; Piguet, V. The Growing Problem of Antifungal Resistance in Onychomycosis and Other Superficial Mycoses. *Am. J. Clin. Dermatol.* **2021**, *22*, 149–157. [CrossRef]
9. Wang, B.; Yang, W.; McKittrick, J.; Meyers, M.A. Keratin: Structure, Mechanical Properties, Occurrence in Biological Organisms, and Efforts at Bioinspiration. *Prog. Mater. Sci.* **2016**, *76*, 229–318. [CrossRef]
10. Bonetti, M.; Bracchi, M.; Musitelli, G.; Perugini, P. Production and Characterization of Bovine Hoof Membranes as Standardized in Vitro Model for Nail Studies. *Int. J. Pharm.* **2021**, *600*, 120409. [CrossRef]
11. Murdan, S. Drug Delivery to the Nail Following Topical Application. *Int. J. Pharm.* **2002**, *236*, 1–26. [CrossRef]
12. Yang, F.; Yu, X.; Shao, W.; Guo, P.; Cao, S.; Wang, M.; Wang, Y.; Wu, C.; Xu, Y. Co-Delivery of Terbinafine Hydrochloride and Urea with an in Situ Film-Forming System for Nail Targeting Treatment. *Int. J. Pharm.* **2020**, *585*, 119497. [CrossRef]
13. Mertin, D.; Lippold, B.C. In-Vitro Permeability of the Human Nail and of a Keratin Membrane from Bovine Hooves: Influence of the Partition Coefficient Octanol/Water and the Water Solubility of Drugs on Their Permeability and Maximum Flux. *J. Pharm. Pharmacol.* **1997**, *49*, 30–34. [CrossRef]
14. Lusiana; Reichl, S.; Müller-Goymann, C.C. Infected Nail Plate Model Made of Human Hair Keratin for Evaluating the Efficacy of Different Topical Antifungal Formulations against Trichophyton Rubrum in Vitro. *Eur. J. Pharm. Biopharm.* **2013**, *84*, 599–605. [CrossRef]
15. Mertin, D.; Lippold, B.C. In-Vitro Permeability of the Human Nail and of a Keratin Membrane from Bovine Hooves: Prediction of the Penetration Rate of Antimycotics through the Nail Plate and Their Efficacy. *J. Pharm. Pharmacol.* **1997**, *49*, 866–872. [CrossRef]
16. Nogueiras-Nieto, L.; Gómez-Amoza, J.L.; Delgado-Charro, M.B.; Otero-Espinar, F.J. Hydration and N-Acetyl-l-Cysteine Alter the Microstructure of Human Nail and Bovine Hoof: Implications for Drug Delivery. *J. Control. Release* **2011**, *156*, 337–344. [CrossRef]
17. Baillie, C.; Southam, C.; Buxton, A.; Pavan, P. Structure and Properties of Bovine Hoof Horn. *Adv. Compos. Lett.* **2000**, *9*, 096369350000900202. [CrossRef]
18. Wang, B.; Zhou, B.; Zhang, X.; Wang, B. Microstructure and Mechanical Properties of an Alpha Keratin Bovine Hoof Wall. *J. Mech. Behav. Biomed. Mater.* **2020**, *104*, 103689. [CrossRef]
19. Naumann, S.; Meyer, J.-P.; Kiesow, A.; Mrestani, Y.; Wohlrab, J.; Neubert, R.H.H. Controlled Nail Delivery of a Novel Lipophilic Antifungal Agent Using Various Modern Drug Carrier Systems as Well as in Vitro and Ex Vivo Model Systems. *J. Control. Release* **2014**, *180*, 60–70. [CrossRef]
20. Monti, D.; Saccomani, L.; Chetoni, P.; Burgalassi, S.; Senesi, S.; Ghelardi, E.; Mailland, F. Hydrosoluble Medicated Nail Lacquers: In Vitro Drug Permeation and Corresponding Antimycotic Activity. *Br. J. Dermatol.* **2010**, *162*, 311–317. [CrossRef]
21. Šveikauskaitė, I.; Pockevičius, A.; Briedis, V. Potential of Chemical and Physical Enhancers for Transungual Delivery of Amorolfine Hydrochloride. *Materials* **2019**, *12*, 1028. [CrossRef]
22. Park, J.S.; Kim, J.S.; Ho, M.J.; Park, D.W.; Kim, E.A.; Choi, Y.S.; Jang, S.W.; Kang, M.J. Effect of Penetration Enhancers on Toenail Delivery of Efinaconazole from Hydroalcoholic Preparations. *Molecules* **2021**, *26*, 1650. [CrossRef]
23. Cutrín-Gómez, E.; Anguiano-Igea, S.; Delgado-Charro, M.B.; Gómez-Amoza, J.L.; Otero-Espinar, F.J. Effect of Penetration Enhancers on Drug Nail Permeability from Cyclodextrin/Poloxamer-Soluble Polypseudorotaxane-Based Nail Lacquers. *Pharmaceutics* **2018**, *10*, 273. [CrossRef]
24. Cutrín Gómez, E.; Anguiano Igea, S.; Delgado-Charro, M.B.; Gómez Amoza, J.L.; Otero Espinar, F.J. Microstructural Alterations in the Onychomycotic and Psoriatic Nail: Relevance in Drug Delivery. *Eur. J. Pharm. Biopharm.* **2018**, *128*, 48–56. [CrossRef]
25. Kracht, T.; Müller-Goymann, C.C. Antifungal Efficacy of Liquid Poloxamer 407-Based Emulsions Loaded with Sertaconazole Nitrate. *Int. J. Pharm.* **2020**, *585*, 119400. [CrossRef]

Supplementary Materials

Improving Transungual Permeation Study Design by Increased Bovine Hoof Membrane Thickness and Subsequent Infection

Sebastian Kappes [1], Thilo Faber [1], Lotta Nelleßen [1], Tanju Yesilkaya [2], Udo Bock [3] and Alf Lamprecht [1,4,*]

[1] Department of Pharmaceutics, Institute of Pharmacy, University of Bonn, Gerhard-Domagk-Str. 3, 53121 Bonn, Germany; kappes.sebastian@uni-bonn.de (S.K.); thilo.faber@uni-bonn.de (T.F.); s6annell@uni-bonn.de (L.N.)
[2] Bayer Vital GmbH, 51373 Leverkusen, Germany; tanju.yesilkaya@bayer.com
[3] Bock Project Management, 54456 Tawern, Germany; udo.bock@bock-pm.com
[4] PEPITE EA4267, University of Burgundy/Franche-Comté, 25000 Besançon, France
* Correspondence: alf.lamprecht@uni-bonn.de; Tel.: +49-228-735-243; Fax: +49-228-735-268

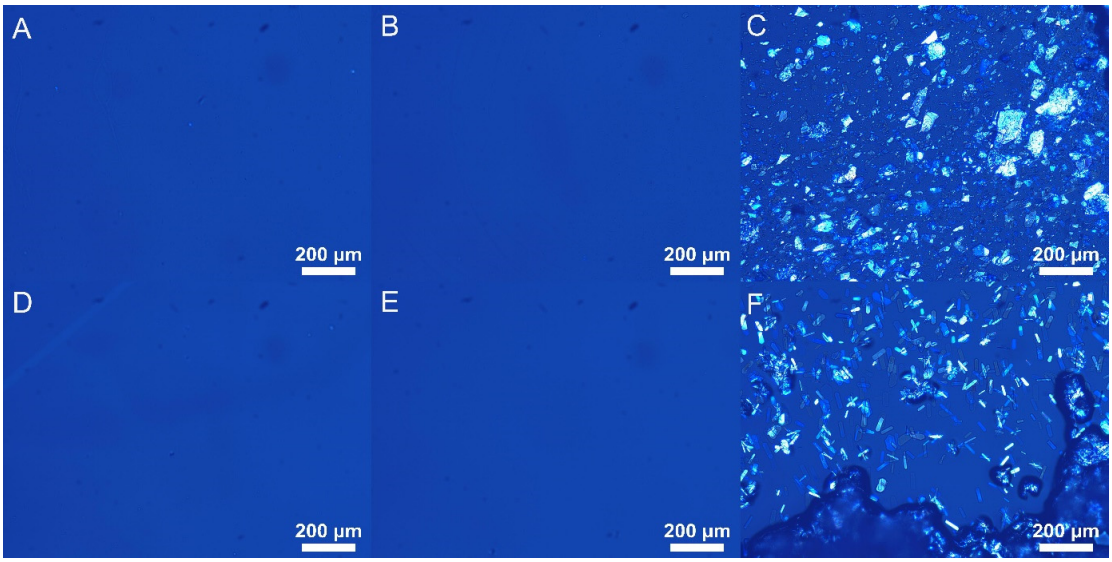

Figure S1. Polarized light microscopy images of a (**A**) patch (PAT) placebo, (**B**) 10% PAT, (**C**) 20% PAT, (**D**) lacquer (LAC) placebo, (**E**) 10% LAC and (**F**) 20% LAC.

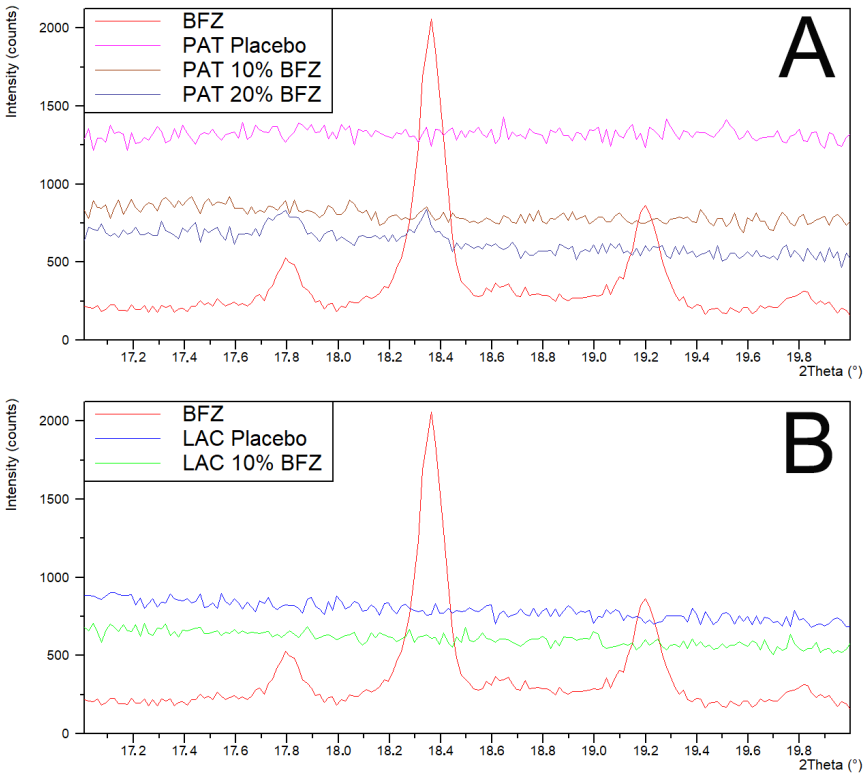

Figure S2. X-ray diffractograms of a (**A**) patch (PAT) and (**B**) lacquer (LAC) containing bifonazole (BFZ).

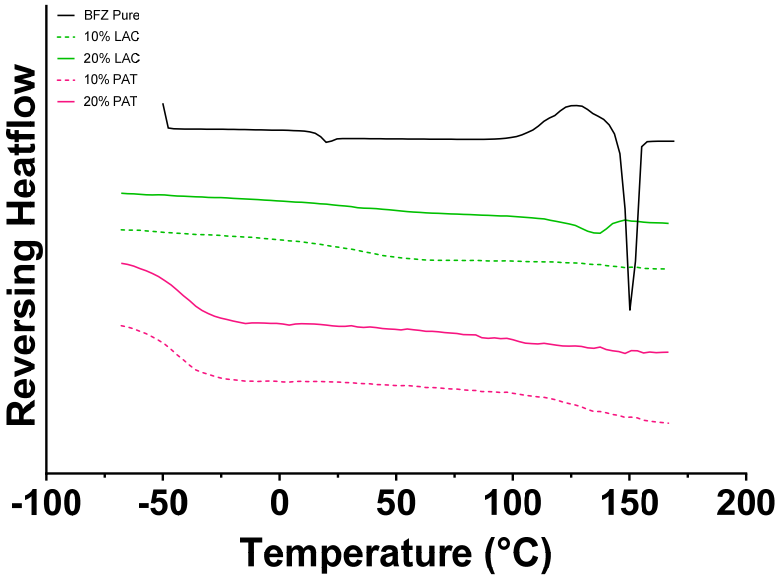

Figure S3. Thermograms of pure bifonazole (BFZ), 10 and 20% patch (PAT), and lacquer (LAC).

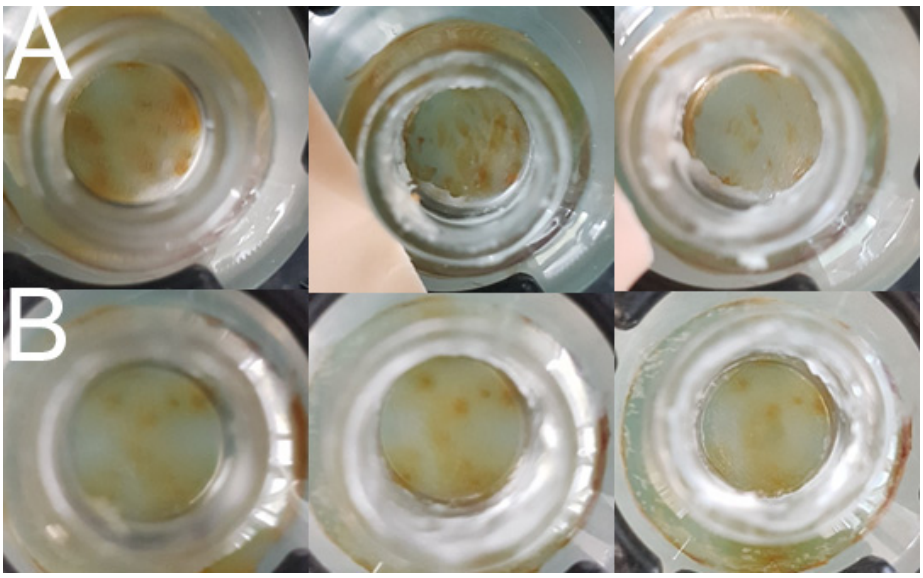

Figure S4. Surfaces of infected 400-µm bovine hoof sheets treated with (**A**) Canesten® Extra Salbe and (**B**) Canesten® Extra Creme at 0 d, 3 d and 6 d from left to right.